UNIVERSITY OF
Southampton

Faculty of Engineering and Physical Sciences
School of Physics and Astronomy

Polariton condensates in optically imprinted potential landscapes

Lucinda Michelle Pickup

A thesis submitted for the degree of
Doctor of Philosophy

December 2019

UNIVERSITY OF SOUTHAMPTON

ABSTRACT

FACULTY OF ENGINEERING AND PHYSICAL SCIENCES
SCHOOL OF PHYSICS AND ASTRONOMY

Doctor of Philosophy

POLARITON CONDENSATES IN OPTICALLY IMPRINTED POTENTIAL LANDSCAPES

by Lucinda Michelle Pickup

Microcavity-polaritons are quasi-particles formed when light and matter excitations couple strongly in cavities that have confinement lengths similar to the wavelength of light. Polariton's light effective mass, due to the photonic component, in conjunction with their composite boson nature, allows a transition into a macroscopically occupied quantum degenerate state (polariton condensate) for temperatures ranging from 4K up to room temperature. Due to the exciton reservoirs produced under non-resonant excitation and polariton's strong interparticle interactions (originating from their matter component) potential landscapes for the polaritons can be sculpted with the non-resonant laser beam(s) pumping the system. The work presented in this thesis is specifically concerned with inorganic polariton condensates in optically imprinted potential landscapes.

With annular excitation geometries it is possible to form optically trapped polariton condensates, where the condensate is spatially delocalised from the exciton reservoir. Implementing this optical trap geometry, the first all-optical polariton bistability under non-resonant excitation is demonstrated in the spinor of the condensate. Furthermore, the separation from the exciton reservoir results in significant enhancement of the coherence properties. First order coherence times exceeding 1.5ns are demonstrated for the optical trap excitation geometry; whilst excitation regimes where the condensate overlaps the reservoir demonstrate sub 100ps coherence times.

For narrow Gaussian excitation geometries, the spatial overlap of the condensate and the reservoir results in polaritons ballistically propagating away from pump with a well defined in-plane wavevector. Utilising this inherent in-plane propagation, two freely expanding polariton condensates (a polariton dyad) are shown to remain coupled, even for separation distances exceeding 100μm. Through an in-depth experimental and theoretical investigation of the polariton dyad, it is determined that it is critically important to account for the finite propagation time of polaritons from one condensate centre to the other (i.e. the coupling is time-delayed). The experimental work in this thesis is then concluded by introducing all-optical polariton band structure engineering. Utilising optically imprinted polariton condensates and their exciton reservoirs to both create and image the band structures.

In addition to the experimental results, experimental procedures and analysis techniques, that have been developed and implemented to facilitate the research, are presented.

Contents

List of Figures

Declaration of Authorship

I, Lucinda Michelle Pickup, declare that this thesis entitled 'Polariton condensates in optically imprinted potential landscapes' and the work presented in it are my own and has been generated by me as the result of my own original research.

I confirm that:

1. This work was done wholly or mainly while in candidature for a research degree at this University;
2. Where any part of this thesis has previously been submitted for a degree or any other qualification at this University or any other institution, this has been clearly stated;
3. Where I have consulted the published work of others, this is always clearly attributed;
4. Where I have quoted from the work of others, the source is always given. With the exception of such quotations, this thesis is entirely my own work;
5. I have acknowledged all main sources of help;
6. Where the thesis is based on work done by myself jointly with others, I have made clear exactly what was done by others and what I have contributed myself;
7. Parts of this work have been published in: [1] and [3].

Signed:

Date:

Acknowledgements

The path I have taken since starting my PhD candidature has been full of development, enjoyment and yes a 'little' bit of stress at times. However, even through the trials and tribulations of doing a PhD I retain the exuberance I had when seeing the lab for the first time. There are so many people I have to thank for helping me develop my skill sets, keeping me sane and just being there during the last four years.

I cannot thank Prof Pavlos Lagoudakis enough for affording me the opportunity to join the Hybrid Photonics group and dive into the fascinating world of polaritonics. For giving guidance when needed but simultaneously trusting in and allowing me the freedom to develop systems and investigate topics that particularly interest me. Also for just generally being a very encouraging and understanding supervisor.

To my friends and colleagues in the Hybrid Photonics group both current and past, including but not limited to Julian, Helgi, Tamsin, Giacomo, Anton, Stella, Giannis, Alexis, Chris, Paco and (honorary member) Nick, thank you. The group dynamic where we all want to assist one another in the drive to understand the system better is amazing. Specifically, I have had, and continue to have the pleasure of working closely alongside Julian Töpfer, Helgi Sigurðsson over the last couple of years with incredibly fruitful discussions almost every time we talk. I additionally want to thank those who have proof read this thesis.

Thank you to all of the staff in Physics and Astronomy that I have worked with and have always been there to help; especially Nicky, Gareth, Justin, Cameron, Jonathan, Tom, Gareth and Mark.

Thank you to the international scientific community I have met, you have inspired me with your work, welcomed me to discussions and been a fantastic example of how the greater world should be.

To all of my friends outside of physics all I can say is thank you. All the fun things we've done together and all of the support and encouragement you have given me has made even the most stressful times manageable. I need to especially thank Ollie, Katrín, Tory, Elena and Anna (and of course Vasya) for playing particularly significant roles (plus, withstanding all the physics talk)

To my parents, brother and collies (Jess, Meg and Milly), you have always been there supporting me and I cannot express my gratitude for everything. Finally, but most importantly I owe an immeasurable amount to my wife Tabby. From the beginning of our undergraduate studies to the present day you always encourage me, support me through whatever challenges we face in life and ultimately just make everything a better, happier and more exciting experience.

Acronyms

AOM	Acousto-optic modulator
AP	Acoustic phonons
AS	Active stabilistation
BEC	Bose-Einstein condensation
CCD	Charge coupled device
cGLE	complex Ginzburg-Landau equation
CMOS	Complementary metal-oxide-semiconductor
CW	Continuous wave
DBR	Distributed Bragg reflector
DDP	Driven damped pendulum
FFT	Fast Fourier transform
FWHM	Full width half maximum
FSR	Free spectral range
GPE	Gross-Pitaevskii equation
GPU	Graphical processing unit
GS	Gerchberg-Saxton
LC	Liquid crystal
LCOS	Liquid crystal on silicon
LCP	Left circularly polarised
LP	Lower polariton
LPB	Lower polariton branch
MBE	Molecular beam epitaxy
MC	Microcavity
MRAF	Mixed region amplitude freedom
NA	Numerical aperture
NR	Noise region
ODLRO	Off diagonal long range order
OP	Optical phonon
OT	Optically tapped/optical trap
PAN-LC	Parallel aligned nematic liquid crystal
PBS	Polarising beam splitter
PID	Proportional integral differential
PL	Photoluminescence
QW	Quantum well
RCP	Right circularly polarised
RHS	Right hand side

RR	Retroreflector
SLM	Spatial light modulator
SR	Signal region
TH	Top hat
UP	Upper polariton
UPB	Upper polariton branch
VCSEL	Vertical cavity surface emitting laser

Publications

- L. Pickup, K. Kalinin, A. Askitopoulos, Z. Hatzopoulos, P. G. Savvidis, N. G. Berloff, and P. G. Lagoudakis, *Optical Bistability under Nonresonant Excitation in Spinor Polariton Condensates*, Phys. Rev. Lett., vol. **120**, 2018.
- J. D. Töpfer, H. Sigurðsson, L. Pickup, and P. G. Lagoudakis, *Time-delay Polaritonics*, Commun Phys, vol. **3**, 2020
- A. Askitopoulos, L. Pickup, A. Zasedatelev, S. Alyatkin, K. Lagoudakis, W. Langbein, P.G. Lagoudakis *Ultra Long Polariton Condensate Coherence Time*, In preparation, 2019.
- L. Pickup, H. Sigurðsson, J. Ruostekoski and P. G. Lagoudakis, *Synthetic band-structure engineering in polariton crystals with non-Hermitian topological phases*, Submitted, 2020.
- A. Askitopoulos, A. V. Nalitov, E. S. Sedov, L. Pickup, E. D. Cherotchenko, Z. Hatzopoulos, P. G. Savvidis, A. V. Kavokin, and P. G. Lagoudakis, *All-optical quantum fluid spin beam splitter*, Phys. Rev. B, vol. **97**, June 2018.

Preface

In the early 2000s the experimental study of macroscopically occupied (quantum degenerate) states was dominated by dilute ultra cold atoms following the seminal work of Cornell [5] and Ketterle [6] demonstrating Bose-Einstein condensation (BEC) in rubidium-87 and sodium atoms respectively in 1995. Whilst cold atom systems are useful to investigate fundamental problems, the complexity of building and reading such systems as well as the extremely low-temperatures required, makes the integrability of them into real world systems diminishingly small. Exciton-polaritons (simply called polaritons herein) are solid state composite bosonic quasiparticles capable of condensation with a high degree of controllability and simple optical readout. Furthermore, the critical temperature for the transition to the condensed state ranges from standard cryogenic temperatures (4K) to room temperature depending on the specifics of the materials used [7–9].

Polaritons are part light, part matter quasiparticles formed by the strong coupling between light and matter excitations (here Coulomb bound electron-hole pairs called excitons) and they have a lifetime restricted by the reflectivity of the microcavity in which they are formed. The improvements in semiconductor growth techniques, including molecular beam epitaxy (MBE) enabled the growth of samples with high enough Q-factors and oscillator strength (coupling between photonic and excitonic modes) for the first irrefutable demonstration of polariton condensation at standard cryogenic temperatures in 2006 by Kasprzak et al [8]; it having been predicted in 1996 by Imamoglu et al. [10]. The sample used in Ref. [8] was a CdTe based microcavity (MC) and by moving to a microcavity with GaN (a higher bandgap material) as the active material, polariton condensation was demonstrated at room temperature in 2007 [11]. In 2009 polariton condensation in a GaAs based MC was demonstrated for temperatures up to $40K$ in a sample with reduced disorder [12].

Chapter 1

Introduction

1.1 Microcavity Polaritons

Microcavity polaritons are quasiparticles that are the result of normal mode splitting under the strong coupling of light and matter excitations when confined in samples that resemble miniature Fabry-Pérot cavities, with gain medium in the cavity spacer and where the confinement length of which is comparable to the wavelength of light, hence 'microcavity'. The gain medium, in the samples of interest, comes in the form of quantum wells (QWs). The QWs have a bandgap that is narrower than, and fully encapsulated by, the bandgap of the cavity spacer material thus producing a potential well that confines excitons in one dimension. The QWs are positioned around the anti-nodal positions of the photonic cavity mode to maximise coupling between the electromagnetic field and excitons. Polaritons are neither photons or excitons they exist from the oscillation of the confined energy between the photon and exciton states, the frequency of which is charaterised by a parameter called the vacuum Rabi frequency (Ω). In the following section the building blocks for microcavity polaritons are introduced and two coupling regimes of such systems (strong and weak) will be described. Finally different properties of polaritons that are of interest for work presented later will be introduced.

1.1.1 Excitons

An exciton is the quasiparticle formed when a negatively charged electron and a positively charged hole are Coulomb coupled. Excitons can be qualitatively split into those which are 'tightly' bound (Frenkel excitons) and those which extend across multiple lattice sites (Wannier-Mott excitons) [13, 14] . Frenkel excitons correspond better to ionically bound compounds in which the radius of the lowest energy exciton state is smaller than or comparable to the interatomic separation [15]. Wanier-Mott excitons on the other hand better suit inorganic semiconductor materials in which electron bands

exist [16]. Let it be noted all work in this thesis uses direct bandgap semiconductors (GaAs, InGaAs) meaning excitons can be excited/decay directly through single photon absorption/emission, as the minimum in the conduction band and maximum in the valence band dispersions occur for the same momentum.

Wannier-Mott excitons can be considered functionally similarly to the hydrogen atom [16, 17], with a comparable Hamiltonian [17]:

$$H = -\frac{\hbar^2}{2m_e^*}\nabla_e^2 - \frac{\hbar^2}{2m_h^*}\nabla_h^2 - \frac{e^2}{\epsilon|\vec{r}|} \tag{1.1}$$

where m_e^* and m_h^* are the effective masses of the electron and hole respectively, $\epsilon \neq 1$ is the dielectric constant of the material and $\vec{r} = \vec{r}_e - \vec{r}_h$ denotes the separation of electron and hole. Drawing further on the analogy with hydrogen, excitons can be characterised by a Bohr-like radius to describe the spatial extent and by an exciton Rydberg energy (R_{ex}) (the energy necessary to ionise the first bound exciton state). Excitons as a composite particle formed of an electron and hole have a resultant charge of 0 and so have a dispersion for each bound state ($n \in \mathbb{N} \geq 1$) characterised by the free motion of a quasiparticle with effective mass $M = m_h^* + m_e^*$ and wavevector $\vec{k}$ [15–17]:

$$E_{x_n}(\vec{k}) = E_g - \frac{R_{ex}}{n^2} + \frac{\hbar^2|\vec{k}|^2}{2M} \tag{1.2}$$

Comparatively to cavity photons, excitons demonstrate a significantly larger effective mass which means that for most considerations in this thesis the exciton dispersion can be considered flat (i.e. the final term of the right can be neglected).

1.1.1.1 Exciton confinement in one-dimension

Due to the notable exciton Bohr radius, for bulk GaAs $\sim$ 12.5nm [17], it is possible to construct confining potentials that are comparable in size to the bulk exciton Bohr radius, consequently confining the excitons in these directions. Discussion of confinement shall be restricted to quantum wells (QWs), which are two dimensional planar objects applying confinement in one direction only, as this is the form of confinement relevant to the systems considered.

Quantum confinement leads to the perturbation of the band structures and thus exciton energies and wavefunctions. For an infinitesimally narrow QW with infinitely high barriers the Bohr radius is half that of the corresponding bulk Bohr radius and more critically the binding energy is four times that in bulk ($E_B^{2D} = 4E_B^{3D}$) [18–20]. In more realistic scenarios with finite barriers the binding energy does not increase monotonically with decreasing QW width due to tunneling into the barriers for very narrow

QWs [20–22]. However, broadly it is the case that for confined excitons the binding energy is larger than that in bulk and thus excitons become more thermally stable in QWs. Additionally due to the increased overlap of the electron and hole wavefunctions, the oscillator strength, that characterises the probability of photon absorption/emission, is enhanced [20, 23, 24] which is beneficial when coupling light and matter.

Up to now it has not been necessary to burden the discussion on excitons with specifics on the properties of the valence bands. However, when confinement is introduced the specifics become important in the lifting of a degeneracy in the valence bands [25–27]. For semiconductors with a zincblende structure (face centred cubic with a two atom basis), such as is common in GaAs, the conduction band has s-type symmetry, with angular momentum $l = 0$ and spin $s = \pm 1/2$, whilst the valence bands have p-type symmetry with angular momentum $l = 1$ and spin $s = \pm 1/2$. Considering the valence bands only, the resultant total angular momentum states are $J = l + s = 3/2, 1/2$ leading to a six fold degeneracy on the projection J_z at the Γ point when neglecting spin-orbit interactions [20, 26, 28]. Spin-orbit coupling splits the two states with different J producing a four fold degenerate state $|J; J_z\rangle = |3/2; \pm 3/2, \pm 1/2\rangle$ and a two fold degenerate state $|J; J_z\rangle = |1/2; \pm 1/2\rangle$. The states $|J; J_z\rangle = |1/2; \pm 1/2\rangle$ are known as the split-off band and have a lower energy (so larger separation from the conduction band) and are thus neglected in the current discussion. The remaining four fold degenerate states $|J; J_z\rangle = |3/2; \pm 3/2, \pm 1/2\rangle$ are those that play a role in exciton formation. Looking at the dispersion around the Γ point for bulk GaAs one will see the states $|J; J_z\rangle = |3/2; \pm 3/2\rangle$ show a shallower curve than the $|3/2; \pm 1/2\rangle$ states. In the effective mass free propagating quasiparticle picture, the effective mass is related to the second derivative of the dispersion and so the shallower curve corresponds to a larger mass. Therefore, the states $|3/2; \pm 3/2\rangle$ receive the name 'heavy-holes' (hh) whilst the $|3/2; \pm 1/2\rangle$ states are called 'light holes' (lh) [20, 26, 28]. With the introduction of confinement, the degeneracy of the hh band and lh band at the Γ point is lifted as the quantisation energies are mass dependent [20, 29]. The hh displays a lower energy separation from the conduction band than the lh [26,30]. As such the heavy-hole exciton is energetically the lowest bound state and dominates the spectrum [27, 31].

Possible transitions between electron states in the valence bands (hh and lh) and the conduction band in Zincblende QWs are depicted in Figure 1.1. Blue arrows denote absorption/emission of a right circularly polarised (RCP) photon, and red arrows, absorption/emission of a left circularly polarised (LCP) photon[1] [32,33]. The black arrows denote transitions which cannot occur through simple one photon absorption/emission, due to the required change in J_z exceeding the maximum spin of a photon (± 1 in units of $\hbar$). With the resulting exciton states consequently referred to as dark excitons. It is the optical transition selection rules that enable the determination of the spin of an

[1]Note, linear polarisation photon transitions between the lh and conduction band states are not included in the figure.

exciton (equally polariton) directly through polarisation measurements as is discussed later in Section 1.1.4.

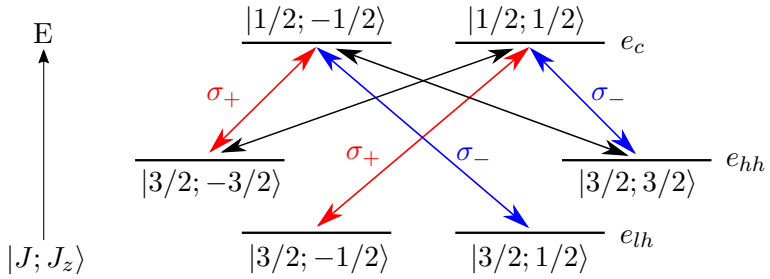

FIGURE 1.1: Transitions in a QW, e_{hh} - electron states in the heavy hole valence band, e_{lh} - electron states in the light hole valence band, e_c - electron states in the conduction band, J - total angular momentum, J_z - angular momentum projection on the z-axis, σ_- - right circular polarised light (blue) and σ_+ - left circular polarised light (red). Black arrows denote transitions which aren't optically active and the resultant excitons are referred to as 'dark excitons'.

1.1.2 Confinement of light - Microcavities

Microcavities are optical resonators where the confinement length in any direction is comparable to the wavelength of the confined light. Confinement can be in one-dimension, two-dimension or three-dimensions [21]. For brevity discussion is limited to one-dimension confinement in the form of Fabry-Pérot microcavities as these are the type used in the work presented here.

Due to the quality of confinement necessary, customisable high reflectivity mirrors known as distributed Bragg reflectors (DBRs) are used over traditional metalic mirrors. DBRs are pair periodic structures formed of alternating layers of materials with refractive index η_a and η_b where the optical thickness ($\eta_i d_i,\ i = a, b$) of each layer is $\lambda_{Bragg}/4$ (λ_{Bragg} is the central wavelength the DBR is designed for). The π phase shift experienced by a wave reflected at a boundary from low to high refractive index mediums along with the $\lambda_{Bragg}/2$ round trip through one layer means the reflections from each boundary constructively interfere, leading to a very high overall reflectivity around λ_{Bragg}. The region around λ_{Bragg} for which there is high reflectivity is referred to as the photonic stopband of the DBR. The overall reflectivity of the DBR in the stopband can be controlled by the number of pairs of layers deposited. The spectral width of the stopband is tailored by the refractive index difference of the two materials forming a pair [21, 34]. The resulting stopbands can have reflectivities close to 100% spanning up to hundreds of nm. The reflectivity spectrum of such systems can be calculated using the transfer matrix method [21, 35, 36], an example spectrum for a DBR of 28 pairs of AlAs/AlGaAs is shown in Figure 1.2 (a).

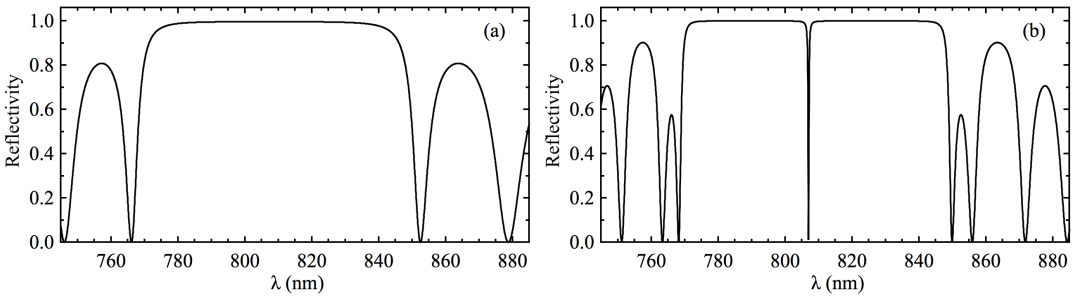

FIGURE 1.2: Transfer matrix reflectivity spectra (a) DBR consisting of 28 pairs of AlAs/AlGaAs with $\lambda_{Bragg} = 807$nm and (b) a $5\lambda/2$ AlGaAs cavity with 28 pair layer DBRs front and back. Note in the above calculations $\lambda = \lambda_{Bragg}$ and no substrate is included in the calculations.

A Fabry-Pérot microcavity is formed by separating two DBRs with a cavity spacer [2] that has an optical path length $L_c = \eta_c d_c$, where η_c is the refractive index and d_c is the geometric length of the cavity spacer. As is true for traditional Fabry-Pérot cavities, modes fulfilling the resonance condition $\lambda_m = 2L_c/m$ (equally $\omega_m = mc\pi/L_c$), where $m \in \mathbb{N} \geq 1$, see strong enhancement within the cavity if the mode is within the stopband of the DBRs[3]. As a result of the cavity, there is a strong suppression of the samples reflectivity around the resonant frequency. The free spectral range (FSR), i.e. the separation between consecutive resonant modes of a cavity, is inversely related to the length of the resonantor, $\Delta\omega = c\pi/L_c$. Thus using small cavities, i.e. $m \leq 5$, makes the FSR large enough so that only one resonant mode is within the stopband of the DBRs which, as will be discussed later, prevents mode competition in the creation of polaritons. The quality of the confinement is quantified via a parameter called the Q-factor:

$$Q = \frac{\omega_c}{\delta\omega_c} \tag{1.3}$$

where ω_c is the angular frequency of the resonant mode and $\delta\omega_c$ is the FWHM of the mode. It can be interpreted as the ratio of the energy stored in the cavity to the energy dissipated in one period. The higher the Q-factor the longer the lifetime of the cavity photons. The predicted reflectivity spectrum for a microcavity formed of two of the DBRs, whose reflectivity is shown in Figure 1.2 (a), separated by a $5\lambda/2\eta_c$ AlGaAs cavity with $\lambda = 807$nm is shown in Figure 1.2 (b).

The resonance conditions for Fabry-Pérot cavities, discussed above, quantises the wavevector only in the direction normal to the surface of the sample (also referred to as the growth direction $\hat{\boldsymbol{z}}$), k_z. There is a continuum of accessible wavevectors within the plane

[2]The cavity spacer can be viewed as a defect in an otherwise perfectly periodic one-dimensional photonic crystal.

[3]The cavity mode in DBR microcavities will be slightly shifted due to the penetration of the fields into the DBRs, an effect that is not experienced by metallic mirrors.

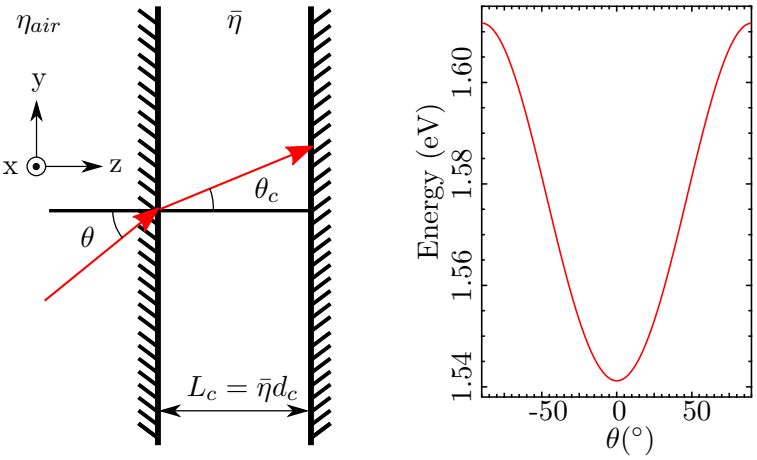

FIGURE 1.3: Left - Schematic for a planar Fabry-Pérot cavity. Right - Corresponding angular dispersion for a cavity with a resonant wavelength of $805nm$ $(1.541eV)$ for $\theta = 0$.

of the sample (the $[\hat{\boldsymbol{x}}, \hat{\boldsymbol{y}}]$ plane) $k_{||} = \sqrt{k_x^2 + k_y^2}$, this results in a parabolic shaped dispersion of the cavity mode as a function of $k_{||}$, which maps to the angle from the normal to the surface. This is best understood through the calculation of the resonant frequencies ($\omega_c = \sqrt{\omega_z^2 + \omega_{||}^2}$) as a function of polar angle (θ_c) inside the cavity from the normal (where $\theta_c < \pi/2$). Noting the restraints on ω_z i.e. $\omega_c \cos(\theta_c) = \omega_z = mc\pi/L_c$ the resonant frequencies are:

$$\omega_c(\theta_c) = \frac{mc\pi}{\cos(\theta_c) L_c}. \tag{1.4}$$

Using an average refractive index ($\bar{\eta}$) of the microcavity, the refractive index of air and Snell's law this resonance condition can be expressed in terms of a dispersion relation as a function of the angle of incidence on the samples surface (θ)[4];

$$\omega_c(\theta) = \frac{(mc\pi/d_c)}{\sqrt{\bar{\eta}^2 - \sin^2(\theta)}}. \tag{1.5}$$

An example of this dispersion is shown alongside a schematic in Figure 1.3. In the effective mass picture this parabolic dispersion implies that the cavity mode photons gain an effective mass due to the confinement in the growth direction.

Note that whilst for ideal Fabry-Pérot cavities, like those described above, the two DBRs are parallel to one another; to add another degree of control to the polariton system, the

[4]Note, the optical path length L_c is rewritten in terms of geometrical length and $\bar{\eta}$. The use of $\bar{\eta}$ is reasonable in an ideal cavity formed from thin mirrors as $\bar{\eta} \approx \eta_c$.

cavity spacer is generally wedged in one direction. The purpose of this wedge is to allow the energy difference between the cavity mode and exciton to be tuned on one sample. The angle is very shallow and thus generally the approximation of azimuthal symmetry remains valid.

1.1.3 Light matter coupling

Cavity quantum electrodynamics can be studied efficiently in a system combining the two forms of confinement described above, i.e. placing QWs within a microcavity. The cavity mode couples to the exciton dipole moment with a coupling energy proportional to the product of the amplitude of the confined electric field and the exciton dipole moment; let this light-matter coupling energy be denoted E_{LM}. This coupling can be expressed in a form that is more conducive to visualising the various regimes of coupling by considering the frequency $\Omega = E_{LM}/\hbar$ that describes the rate of transfer between the bare modes [37]. In this sense Ω can be viewed as a form of Rabi frequency with consideration to the nomenclature established in the atomic community.

When Ω exceeds all decay rates of the system, i.e. the non-radiative decay of the exciton (γ_x) and the decay rate of the cavity (γ_c), the system is said to be in the strong coupling regime [21, 37]. In the strong coupling regime energy cycles back and forth between the cavity mode and exciton mode multiple times before finally escaping the system (generally in the form of a photon tunneling through the DBRs)[5]. This Rabi oscillation results in two new eigenstates of the coupled system called the upper and lower polariton. The polariton states are bosonic quasiparticles that are part light and part matter and can be seen spectrally as two new energies distinct from the bare cavity and bare exciton modes, analogous to the normal mode splitting for coupled oscillators. Strong coupling is often demonstrated via an anti-crossing of the two polariton modes when the cavity mode crosses the exciton mode, see Figure 1.4. The energetic separation between the upper and lower polariton when the cavity and exciton modes are degenerate ($E_x = E_c$) is referred to as the Rabi splitting and is equal to $2\hbar\Omega$. Strong coupling in cavity-polariton systems was first experimentally demonstrated by C Weisbuch et al in 1992 [38].

On the other hand if $\Omega \leq \gamma_c, \gamma_x$ then the system is in the weak coupling regime whereby there is no coherent oscillation of energy between the bare exciton and cavity mode. In the weak coupling regime one reverts to a system resembling a vectial cavity surface emitting laser (VCSEL).

With the above requirements for strong coupling in mind, some key parameters that control the design process of sample production are the cavity decay rate and the placement

[5] As generally $\gamma_c > \gamma_x$, strong coupling can be described as the situation where the probability of a photon (produced from exciton annihilation) being re-absorbed to create an exciton exceeds that of the photon escaping the cavity.

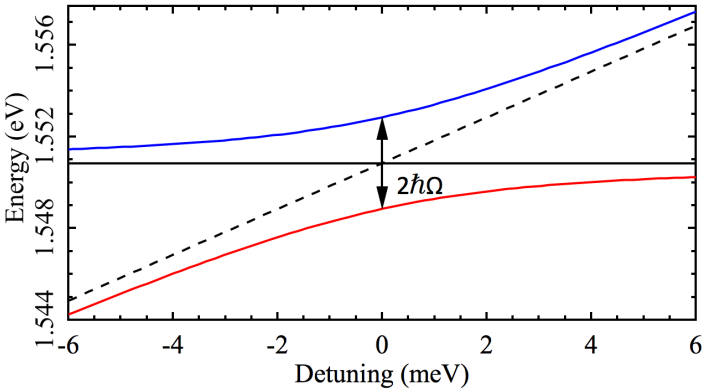

FIGURE 1.4: Anticrossing behaviour of the calculated lower and upper polariton branches (see Eqn. 1.12) at $k_{||} = 0$ as the detuning between the cavity mode and exciton mode is swept from negative to positive. Blue solid line - upper polariton, red solid line - lower polariton, black solid line - exciton and black dashed line - cavity energy.

and number of QWs. As the photon-exciton coupling is proportional to the amplitude of the electric field, QWs are placed around the anti-nodal positions of the confined electric field. However, excitons retain their composite bosonic nature only in the limit of low density [21], therefore, groups of QWs centred around each of the electric field anti-nodal positions are used. This enables a much larger number of excitons to exist around the maximum 'gain' regions without crossing the exciton saturation density (Mott transition) that would result in exciton dissociation and the loss of strong coupling. The QW-QW separation within a group is chosen, for the samples used here, so that there is negligible overlap of exciton wavefunctions from neighbouring QWs.

As discussed in Section 1.1.2 DBRs are used in place of more traditional metallic mirrors due to the tunable stopband with very high reflectivity reducing the cavity decay rate. Unfortunately unlike metallic mirrors which exhibit very low field penetration depths, for DBRs the electric field penetrates deep into the structures effectively lengthening the cavity [21,34,39]. In the limit of a large number of DBR pairs the penetration depth (L_{DBR}) can be defined as [21,34]:

$$L_{DBR} = \frac{\lambda_{Bragg}\eta_a\eta_b}{2\eta_c|(\eta_b - \eta_a)|} \tag{1.6}$$

In Ref [34] V. Savona et al. show that the coupling between the cavity mode and exciton transition is inversely proportional to the effective cavity length ($L_{eff} = L_c + 2L_{DBR}$). So the use of DBRs vastly improves the cavity decay rate, but due to the extension of the effective cavity length, the coupling strength is slightly reduced. However, as strong coupling is routinely demonstrated experimentally nowadays, this reduction in coupling strength is insignificant compared to the benefits of DBRs and thus shall not be considered further. Lastly, due to the microcavity confinement length the FSR is so

large only one mode exists in the stopband thus removing any gain/mode competition and lowering the excitation densities required for quantum degeneracy - discussed later - thus further reducing the risk of reaching the Mott transition.

1.1.3.1 Strong photon-exciton coupling

The coupled light-matter system is described via the Hamiltonian,

$$\hat{H}(k_{||}) = \sum_{k_{||}} E_c(k_{||}) a^{\dagger}_{k_{||}} a_{k_{||}} + \sum_{k_{||}} E_x(k_{||}) b^{\dagger}_{k_{||}} b_{k_{||}} + \sum_{k_{||}} \hbar\Omega (a^{\dagger}_{k_{||}} b_{k_{||}} + a_{k_{||}} b^{\dagger}_{k_{||}}) \tag{1.7}$$

where $E_c(k_{||})$ is the cavity mode dispersion and $E_x(k_{||})$ is the exciton dispersion[6] for an in-plane wavevector $k_{||}$. $a^{\dagger}_{k_{||}}$ ($b^{\dagger}_{k_{||}}$) and $a_{k_{||}}$ ($b_{k_{||}}$) are the photon (exciton) creation and annihilation operators for a given $k_{||}$ respectively [21, 40]. The creation and annihilation operators increase or decrease the number of excitations in a state by 1 respectively obeying the following conditions:

$$\begin{aligned} a|n\rangle_a &= \sqrt{n}|n-1\rangle_a \\ a^{\dagger}|n\rangle_a &= \sqrt{n+1}|n+1\rangle_a \end{aligned} \tag{1.8}$$

where $|n\rangle_a$ is a given Fock state (with occupation n) on which the creation/annihilation operators act. From these creation and annihilation operators a new operator called the number operator (N) can be defined $N = a^{\dagger}a$, which gives the occupation of the state on which the creation/annihilation operators act. The Hamiltonian can be translated into a matrix depiction that can more intuitively be diagonalised to give the new eigenenergies/states of the system. By expanding the Hamiltonian on the state $|n_x\rangle \otimes |n_c\rangle$ written for brevity as $|n_x, n_c\rangle$ in a single particle state ($n_c + n_x = 1$) the Hamiltonian becomes:

$$\hat{H} = \begin{pmatrix} \langle 1,0|\hat{H}|1,0\rangle & \langle 1,0|\hat{H}|0,1\rangle \\ \langle 0,1|\hat{H}|1,0\rangle & \langle 0,1|\hat{H}|0,1\rangle \end{pmatrix} \tag{1.9}$$

For demonstration, the expansion of the first term $\hat{H}_{00}$ is shown below, noting that dependency on $k_{||}$ has been neglected for simplicity:

[6] Due to the effective mass of excitons being orders of magnitude larger than the confined cavity mode, for the relevant values of $k_{||}$, the exciton dispersion can be considered flat.

$$\begin{aligned}\hat{H}|1,0\rangle &= (E_c a^\dagger \cdot 0) + (1 \cdot E_x|1,0\rangle) + (1 \cdot \hbar\Omega|0,1\rangle) + (\hbar\Omega\sqrt{2} \cdot 0) \\ \langle 1,0|\hat{H}|1,0\rangle &= \langle 1,0|1 \cdot E_x|1,0\rangle + \langle 1,0|1 \cdot \hbar\Omega|0,1\rangle = E_x\end{aligned} \tag{1.10}$$

where on the top line of Equation 1.10 the first and last terms on the RHS disappear because $a|0\rangle_a = 0$. Finally the second term on the RHS of the bottom row disappears due to orthonormality ($\langle i,j|k,l\rangle = \delta_{i,k}\delta_{j,l}$). Following the same procedure for the remaining elements of the Hamiltonian results in the final form:

$$\hat{H}(k_{||}) = \begin{pmatrix} E_x(k_{||}) & \hbar\Omega \\ \hbar\Omega & E_c(k_{||}) \end{pmatrix} \tag{1.11}$$

Diagonalising Equation 1.11 yields the eigenenergies:

$$E_{UP,LP}(k_{||}) = \frac{E_c(k_{||}) + E_x(k_{||})}{2} \pm \frac{1}{2}\sqrt{(E_c(k_{||}) - E_x(k_{||}))^2 + 4\hbar^2\Omega^2} \tag{1.12}$$

corresponding to the dispersion relations of the upper ($E_{UP}(k_{||})$) and lower ($E_{LP}(k_{||})$) polariton branches. These new states are superpositions of the bare exciton and bare cavity states and can be written as:

$$|LP(k_{||})\rangle = \mathcal{X}(k_{||})|X(k_{||})\rangle - \mathcal{C}(k_{||})|C(k_{||})\rangle \tag{1.13}$$

$$|UP(k_{||})\rangle = \mathcal{C}(k_{||})|X(k_{||})\rangle + \mathcal{X}(k_{||})|C(k_{||})\rangle \tag{1.14}$$

where $\mathcal{X}(k_{||})$ and $\mathcal{C}(k_{||})$ are the Hopfield coefficients. The photonic and excitonic fraction of the polariton states can thus be determined via the amplitude squared Hopfield coefficients [21]

$$|\mathcal{C}(k_{||})|^2 = \frac{E_{UP}(k_{||})E_x(k_{||}) - E_{LP}(k_{||})E_c(k_{||})}{(E_c(k_{||}) + E_x(k_{||}))\sqrt{(E_c(k_{||}) - E_x(k_{||}))^2 + 4\hbar^2\Omega^2}} \tag{1.15}$$

$$|\mathcal{X}(k_{||})|^2 = \frac{E_{UP}(k_{||})E_c(k_{||}) - E_{LP}(k_{||})E_x(k_{||})}{(E_c(k_{||}) + E_x(k_{||}))\sqrt{(E_c(k_{||}) - E_x(k_{||}))^2 + 4\hbar^2\Omega^2}}. \tag{1.16}$$

For the LP branch the photonic fraction is $|\mathcal{C}(k_{||})|^2$ and the exciton fraction is $|\mathcal{X}(k_{||})|^2$ with $|\mathcal{C}(k_{||})|^2 + |\mathcal{X}(k_{||})|^2 = 1$; note the contributions are swapped for the UP branch.

In Section 1.1.2 it was mentioned that, in general, a shallow wedge is grown into the microcavity spacer layer to allow tuning of the cavity mode with respect to the exciton

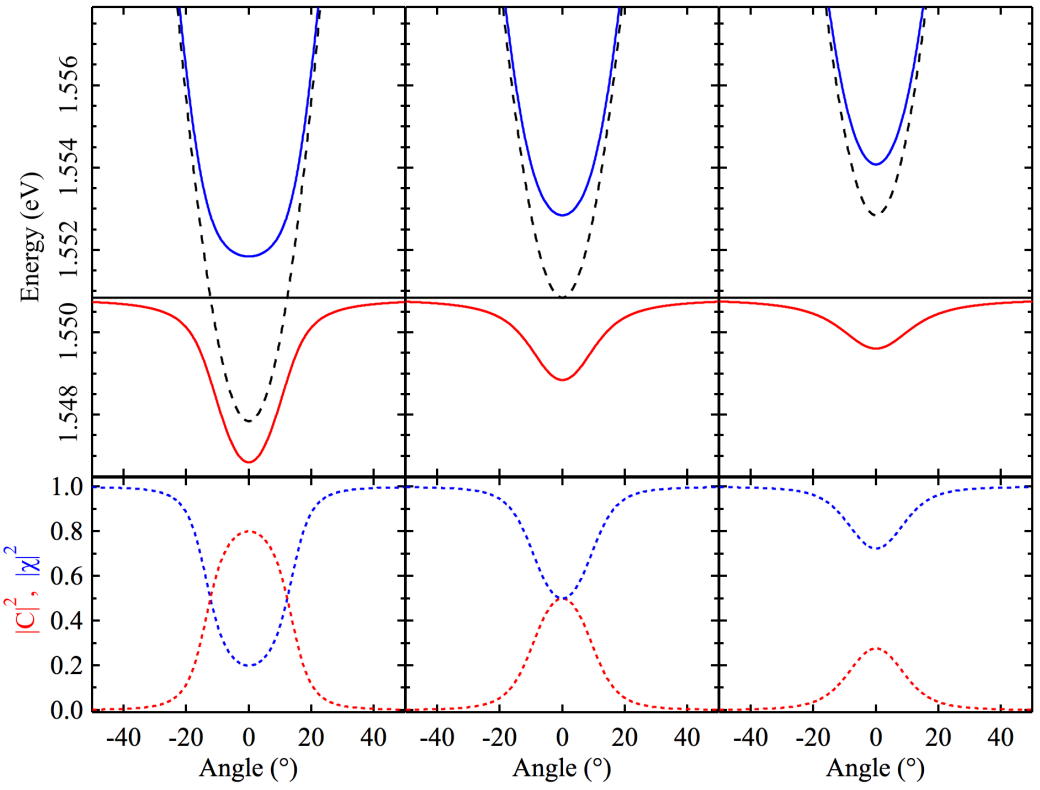

FIGURE 1.5: Top row: Polariton dispersions for (left) negative detuning, (middle) zero detuning and (right) positive detuning. Solid red lines - lower polariton branch $E_{LP}(k_{||})$, solid blue lines - upper polariton branch $E_{UP}(k_{||})$, dashed black lines - cavity dispersion $E_c(k_{||})$ and solid black lines - exciton dispersion $E_x(k_{||})$. Bottom row: red dashed line - photon fraction ($|\mathcal{C}(k_{||})|^2$) and blue dashed line - exciton fraction ($|\mathcal{X}(k_{||})|^2$) of the lower polariton branch for the dispersions in the top row.

mode. The difference in energy between the cavity mode and the exciton mode at $k_{||} = 0$ ($\delta = E_c(0) - E_x(0)$) is called the detuning. By adjusting the detuning, the properties of the resulting LP branch can be tuned as necessary (the UP branch is not relevant to the work conducted here). Figure 1.5 depicts the dispersions and corresponding LP photon and exciton fractions for a negative detuning ($\delta < 0$), zero detuning ($\delta = 0$) and a positive detuning ($\delta > 0$). More negative detunings result in a LP dispersion that is steeper around $k_{||} = 0$ which in the effective mass approximation relates to a lighter, and thus more photonic, particle[7]. Therefore, negative detunings favour themselves for condensation as condensation temperature scales inversely with mass as will be discussed in Section 1.2. The benefit of more positive detunings however is the increased exciton fraction, which gives rise to elevated interparticle interactions and non-linear behaviours.

[7]Note the effective mass approximation is only valid for small angles (equally small $k_{||}$) where the LP dispersion is approximately parabolic.

1.1.4 Polariton spin

Polaritons, being quasiparticles formed by the superposition of exciton and photon states inherit their spin from the constituent particles. Circularly polarised photons have a spin of ± 1 (in units of $\hbar$) determined by the helicity of the polarisation. Excitons also have an integer spin, determined by the band structure of the upper most valence band and the conduction band[8]. Therefore, polaritons are bosons with integer spin and furthermore, thanks to the optical transition selection rules, the spin of polaritons can be determined directly via the polarisation of the photoluminescence (PL) [21, 32, 41]. This can be seen in Figure 1.6 in terms of the transitions between the electron states of the heavy-hole valence band and the conduction band. It is cast in a slightly different light in Figure 1.7 presenting the optical transitions in terms of the creation and annihilation of excitons referring to absorption and emission respectively. A spin $+1$ exciton is optically accessible only via a left circularly polarised (LCP) photon (σ_+) and similarly a spin -1 exciton with a right circularly polarised (RCP) photon (σ_-).

A perfectly spin polarised polariton condensate (in the absence of any spin relaxation) would yield a perfectly circularly polarised PL, the helicity of which is determined by which spin state the condensate exists in. An elliptical or linear PL polarisation corresponds to a condensate that has components in both polariton spin projections.

Additionally it is possible to control the initial spin state of a condensate via the excitation laser. Even under non-resonant excitation (see Section 2.2.1) in which a plasma of uncoupled charge carriers (electrons and holes) is injected, the relaxation to the Coulomb correlated exciton states is faster than the electron spin-dephasing time. This allows for the formation of a spin polarised exciton population which results in a spin polarised polariton condensate, whereby the relative amplitudes of the two spinor components can be controlled via the polarisation of the non-resonant excitation beam [1, 42].

1.2 Quantum degeneracy - Bose Einstein Condensation

In the early 20th century A. Einstein recieved S. N. Bose's work on the statistics of photons which led to his proposal that ideal, non-interacting bosons should undergo a phase transition to a quantum degenerate state (condensate); with the threshold for condensation occurring when the associated de Broglie wavelength becomes comparable to the interparticle separation [43, 44]. The macroscopically occupied quantum degenerate state is given the nomenclature of Bose-Einstein condensation (BEC).

[8] In Section 1.1.1.1 both the heavy and light hole valence bands were considered, but the splitting in energy due to confinement is significant enough that we can neglect light hole excitons in the consideration of our polariton system as the light hole exciton is far detuned from the cavity. Therefore, where exciton dispersion is referred to this is the specifically referencing the heavy-hole exciton dispersion.

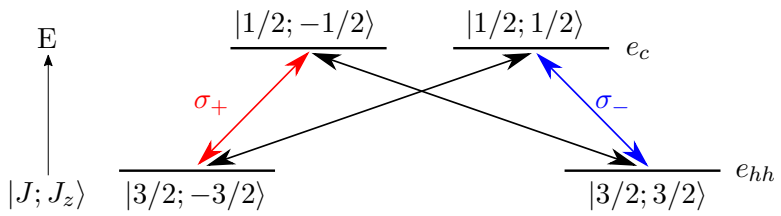

FIGURE 1.6: Exciton transitions between electron states in a QW that are relevant to microcavity polaritons. hh - heavy hole, c - conduction band, J - total angular momentum, J_z - angular momentum projection of z-axis, σ_+ - right circular polarised light (blue) and σ_- - left circular polarised light (red). Black arrows denote transitions which aren't optically active and the resultant excitons are referred to as 'dark excitons'

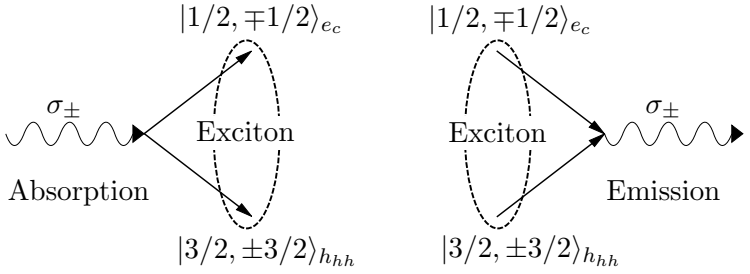

FIGURE 1.7: Recast of the optical transitions between in the heavy hole valence band states (h_{hh}) and the electron conduction band states (e_c) in a Zincblende QW in terms of exciton formation and annihilation. σ_+ - left circularly polarised photon, σ_- - right circularly polarised photon, $|J, J_z\rangle$ defines the states where J - total angular momentum and J_z is the projection of J on to the z-direction.

Work by London [45] some 13 years later indicated a possible connection between the observed superfluidity of He [46] and Bose-Einstein condensation. This marked the first indication that BEC may not be a purely theoretical concept. Nonetheless, it wasn't until 1995 that BEC of dilute atomic systems was demonstrated, when groups led by Cornell [5] and Ketterle [6] independently managed to cool rubidium-87 and sodium respectively, below a critical transition temperature.

In the following, BEC of an ideal non-interacting gas will be discussed and a more experimentally applicable interpretation of condensed bosons outside of static equilibrium will be introduced to describe polariton condensation.

1.2.1 BEC - ideal non-interacting gas in thermal equilibrium

Particles can be split via their spin due to the symmetry of the wavefunction under particle exchange, those with integer spin are referred to as bosons whilst those with half integer spin are Fermions. Fermions famously abide by the Pauli exclusion principle which is to say the highest occupation of any state is 1. Boson's on the other hand aren't subject to any such restrictions and follow the Bose-Einstein distribution:

$$n_\epsilon(\epsilon, T, \mu) = \frac{1}{e^{\beta(\epsilon-\mu)} - 1} \tag{1.17}$$

where n_i is the occupation of the state with energy ϵ_i at temperature T, where $\beta = 1/k_B T$. k_B is the Boltzmann constant and μ is the known as the chemical potential[9]. The total number of particles in the system (N) is determined via the integral:

$$N = \int_0^\infty n_\epsilon(\epsilon) g_{3d}(\epsilon) d\epsilon \tag{1.18}$$

where n_ϵ is as defined above and $g_{3d}(\epsilon)$ is the density of states of a free particle in three-dimensions with mass m in a volume V, defined as [47, 48]:

$$g_{3d}(\epsilon) = \frac{V}{4\pi^2} \left(\frac{2m}{\hbar^2}\right)^{\frac{3}{2}} \epsilon^{1/2} \tag{1.19}$$

where the energy of the ground state has been set to zero ($\epsilon_0 = 0$) to simplify the form of the following functions [10], therefore:

$$\frac{N}{V} = \frac{1}{4\pi^2} \left(\frac{2m}{\hbar^2}\right)^{\frac{3}{2}} \int_{\epsilon_0}^\infty \frac{\epsilon^{1/2}}{e^{\beta(\epsilon-\mu)} - 1} d\epsilon. \tag{1.20}$$

When describing total occupation number N it is necessary to consider the contribution from the ground state $\epsilon = \epsilon_0$ separately as the integrand of Equation 1.20 becomes equal to zero at the ground state. Therefore,

$$\frac{N}{V} = \frac{N_0}{V} + \frac{1}{4\pi^2} \left(\frac{2m}{\hbar^2}\right)^{\frac{3}{2}} \int_{\epsilon_0+\delta\epsilon}^\infty \frac{\epsilon^{1/2}}{e^{\beta(\epsilon-\mu)} - 1} d\epsilon \tag{1.21}$$

where N_0 is the occupation number of the ground state. Note $\delta\epsilon$ in the lower integration limit is infinitesimally small and in most texts the limits are simply left between ϵ_0 and ∞ as the integrand equal to zero for $\epsilon = \epsilon_0$ anyway.

Equation 1.17 and thus N grows monotonically as μ increases towards ϵ_0 therefore the thermodynamic limit ($N, V \to \infty$ while N/V remains constant) corresponds to μ asymptotically approaching 0 (see footnote 10 for the more general case in which ϵ_0 doesn't necessarily equal 0). In the thermodynamic limit a definition of the onset/existence of a condensed state can be introduced. The maximum possible density of particles in the

[9] Equation 1.17 places a restriction on the range of values for μ because $n_\epsilon \geq 0 \Rightarrow e^{\beta(\epsilon-\mu)} - 1 > 1 \Rightarrow \beta(\epsilon - \mu) > ln(1) = 0 \Rightarrow \epsilon - \mu > 0 \Rightarrow -\mu > \epsilon \Rightarrow \mu < \epsilon$. The ultimate limit on μ is determined by the lowest energy (ground) state ϵ_0 (here let $\epsilon_0 = 0$), thus $\mu < 0$.

[10] Note if $\epsilon_0 \neq 0$ then $g_{3d}(\epsilon) = \frac{V}{4\pi^2} \left(\frac{2m}{\hbar^2}\right)^{\frac{3}{2}} (\epsilon - \epsilon_0)^{1/2}$ and the numerator of the integrands in the following functions (Equation 1.20-1.21) are also replaced by $(\epsilon - \epsilon_0)^{1/2}$

excited states (N_{ex}/V) is equal to the second term on the RHS of Equation 1.21 in the limit $\mu = 0$. Should N_{ex}/V be less than the particle density of the whole system (N/V) then all particles beyond $N_{ex}(\mu = 0)$ can only exist in the ground state; and in the limit $N/V \gg N_{ex}(\mu = 0)/V$, there is a macroscopic occupation in a the ground state. With this in mind we can calculate the necessary conditions for condensation by equating $N_{ex}(\mu = 0)/V$ with N/V [47–49]:

$$\frac{N}{V} = \frac{1}{4\pi^2}\left(\frac{2m}{\hbar^2}\right)^{\frac{3}{2}}\int_{\delta\epsilon}^{\infty}\frac{\epsilon^{1/2}}{e^{\beta\epsilon}-1}d\epsilon = \frac{1}{4\pi^2}\left(\frac{2mk_BT_c}{\hbar^2}\right)^{\frac{3}{2}}\int_{\delta x}^{\infty}\frac{x^{1/2}}{e^{x}-1}dx \tag{1.22}$$

where the substitution $x = \epsilon/k_BT_c$ has been made[11]. The final integral converges and can be represented by $\zeta(\frac{3}{2})\Gamma(\frac{3}{2}) \approx 2.315$ where the first term is called the Riemann zeta function and the second is the Gamma function [47]. This is to say the density of particles supported in the excited states converges for three dimensions, consequently allowing us to determine a critical temperature (T_c) and density for condensation to occur. Introducing the thermal de Broglie wave length for a temperature T:

$$\lambda_{th} = \sqrt{\frac{2\pi\hbar^2}{mk_BT}} \tag{1.23}$$

this can be re-expressed as:

$$\frac{N}{V} = \frac{2\zeta(\frac{3}{2})\Gamma(\frac{3}{2})}{\sqrt{\pi}}\frac{1}{\lambda_{th}^3} \approx 2.612\frac{1}{\lambda_{th}^3}. \tag{1.24}$$

Upon the average interparticle spacing becoming comparable to the thermal de Broglie wavelength a transition to a condensed state will occur in a uniform ideal three dimensional system. Rearranging Equation 1.24 one can cast the condition for threshold in yet a different light:

$$T_c = \frac{2\pi\hbar^2}{mk_B}\left(\frac{\tilde{n}}{2.612}\right)^{\frac{2}{3}} \tag{1.25}$$

where $\tilde{n} = N/V$. So the threshold temperature for condensation (T_c) scales inversely with the mass of the particles, hence why polaritons exhibit condensation temperatures orders of magnitude larger than cold atom systems. Furthermore, it scales with particle density, so providing a high density of polaritons can be reached before exciton saturation occurs, the critical temperature can be increased even further.

[11] For the general case where $\epsilon_0 \neq 0$ the substitution becomes $x = (\epsilon - \epsilon_0)/k_BT_c$.

1.2.2 Reduced dimension BEC - Polariton condensation

In the previous subsection, the density of states for an infinite ideal (non-interacting) three dimension bosonic system was used. When using the density of states for ideal infinite systems of lower dimensionality, the integral in Equation 1.21 - 1.22 diverges[12]. This means the maximum number of excited state particles supported is infinite and as such a condensation threshold can never be reached for finite T_c, even though the associated de Broglie wavelength may exceed the interparticle separation [49].

Of course 'infinite' and 'ideal' are mathematical constructs that are seldom reasonable in physical systems. Therefore it is necessary for a slightly altered definition of what constitutes a BEC to describe less ideal systems that i.e.: (1) have finite interparticle interactions; (2) are finite in dimension with respect to the propagation length of the particles; (3) exist in a non uniform potential landscape. The work from Penrose and Onsager (1956) redefined the condition of BEC as the situation in which one or more of the eigenvalues of the density matrix (ρ) describing the system are comparable to unity [50]. A more experimentally demonstrable condition for BEC comes from considering the off diagonal elements of the reduced-density matrix ($\rho^{(1)}$) which corresponds to the single particle density matrix. Off diagonal elements of this reduced-density matrix correspond to coherences of the system; and when considering the projection onto real (Euclidean) space can be probed via spatial coherence measurements through well established interferometric techniques. With this definition (for an infinite system) providing $\rho^{(1)}(\vec{r}, \vec{r}', t)$ remains non-zero in the limit of the separation of points $d = |\vec{r} - \vec{r}'| \to \infty$. then the system can be considered to be in a condensed state. This requirement of the off-diagonal terms remaining non-zero is known as the existence of an off-diagonal long range order (ODLRO). For more realistic systems of finite size if the coherence between two positions in a system drops off as the separation becomes comparable to λ_{th}, then the system is in a non condensed state. On the other hand if coherence is maintained for separation distances far exceeding λ_{th}, then the system is in a condensed phase. The formation of a well defined 'global' phase over the entire condensate (i.e. ODLRO), from an incoherent reservoir, represents a spontaneous breaking of U(1) symmetry [51].

Having overcome the conceptual barrier of defining BEC in reduced dimensionality there is an additional consideration which for years led to contention on the validity of calling a polariton condensate a BEC. The lifetime of polaritons, for most samples, is generally too short for the cloud of polaritons to thermalise to the Bose-Einstein distribution. Regardless of this in 2006 Kasprzak et al. [8] demonstrated enough of the experimental conditions, the critical piece of evidence being the coherence across the cloud (demonstration of ODLRO), for the condensed state to garner the name of a polariton Bose-Einstein condensate, albeit a non-equilibrium condensate. In the time since then, sample growth

[12]The integral fails to converge when the density of states scales with the energy term having an exponent ≤ 0 i.e. when $g(\epsilon) \propto \epsilon^{\alpha}$ for $\alpha \leq 0$. For an ideal infinite 2D $g_{2D}(\epsilon) \propto \epsilon^{0}$ and for 1D $g_{1D}(\epsilon) \propto \epsilon^{-1/2}$ hence condensation is prohibited in the original definition.

techniques and lattice constant matching have allowed samples with longer and longer lifetimes to be produced which has enabled demonstration of a Bose-Einstein distribution of the polariton cloud [52]. This in conjunction with all the additional properties now routinely demonstrated for polaritons (non-linear intensity response to increasing pump power, narrowing of linewidth and particularly the long range order [8]) should finalise the debate that polariton condensation is BEC and not an effect of the non-equilibrium nature. This said, for simplicity all condensed polariton states in this work will be referred to simply as polariton condensates.

How are polariton condensates different from a conventional laser?

Given that samples used for polariton condensate research and VCSELs share many properties a common question is, what makes the polariton condensate a condensate and not a laser? Firstly, in polariton condensates there is no population inversion. Secondly the state that undergoes bosonic stimulation differs significantly between the two. In a laser, bosonic stimulation is from the inverted state directly to the coherent photonic field, whereas in a polariton condensate the bosonic stimulation occurs from a polariton reservoir state to a coherent polariton state lower in energy on the lower polariton branch. The coherent emission seen is a result of stochastic relaxation from this state due to the finite cavity lifetime. That is to say for lasers there is stimulated emission whilst in polariton condensation the stimulation is in the cooling stage [53].

1.3 Simulation of polariton systems

Modeling many body interacting particle systems is an impossible task for any moderate number of particles due to the scaling of the complexity with particle number. It is for this reason that mean field approaches are used in which individual particle interactions/characteristics are replaced via a system average (mean field) simplifying calculations dramatically. The most commonly used approaches to numerically simulate polariton systems today are based off of the Gross-Pitaevskii equation (GPE) and the complex Ginzburg-Landau equations (cGLE), which were originally developed for superfluidity and superconductivity respectively [54]. The GPE and cGLE consider only condensed particles, there is no external bath of heat or particles and thus they are incapable of modeling the phase transition from thermalised to condensed state [55]. However, both have proved time and time again to reproduce experimentally observed features of polariton condensates and arrays thereof.

As the polariton system is inherently open-dissipative, due to the finite lifetime, it requires a balance of pumping and decay to attain a 'steady state'. Correspondingly the GPE and cGLE had to be adapted include decay and pumping. In 2007 M. Wouters and I. Carusotto introduced the first generally applicable model capable of simulating a variety of polariton systems [56]. This came in the form of a generalised GPE coupled to

a simple phenomenological rate equation describing a reservoir of uncondensed particles that feeds the condensed state:

$$i\frac{\partial\psi(\vec{r},t)}{\partial t} = \left(-\frac{\hbar\nabla^2}{2m_{LP}} + \frac{i}{2}(R(n_R)-\gamma) + \alpha|\psi(\vec{r},t)|^2 + 2gn_R\right)\psi(\vec{r},t) \tag{1.26}$$

$$\frac{\partial n_R(\vec{r},t)}{\partial t} = P(\vec{r},t) - \gamma_R n_R(\vec{r},t) - R(n_R)|\psi(\vec{r},t)|^2 + D\nabla^2 n_R(\vec{r},t) \tag{1.27}$$

where ψ is the wavefunction of the condensed state, m_{LP} is the effective mass of the lower polaritons, $R(n_R)$ describes the gain due to scattering from the reservoir of uncondensed particles where n_R is the (areal) density of said reservoir; $R(n_R)$ grows monotonically with n_R. γ is a phenomenological decay rate of the condensate, α is the polariton-polariton interaction strength giving rise to the non-linearity of the condensate and g is the blueshift due to strong interactions between polaritons and the exciton reservoir. $P(\vec{r},t)$ describes the optical or electrical pump, γ_R is a non-stimulated decay rate of the reservoir and D is a diffusion rate of the reservoir though this is often neglected due to the significantly larger mass of the the reservoir particles keeping them localised to the pump region. Finally the occupation of the condensed state is defined as

$$N = \int |\psi(\vec{r},t)|^2 d^2r. \tag{1.28}$$

An additional term can be included to account for an external potential, be it due to defects, strain etc but for simplicity this has been neglected here. Comparable equations for the cGLE can also be written as is demonstrated in Chapter 3, where additionally the two components of the polariton spinor are accounted for. In some circumstances further refinements are made to the model to bring the simulation closer to experimental observations. Such as the inclusion of a second, inactive, reservoir that feeds the active reservoir but not the condensed state directly, as is used in chapter 5.

The following Chapter introduces the experimental techniques utilised throughout the work presented.

Chapter 2

Experimental techniques

2.1 Samples

To achieve strong coupling between light and exciton transitions in QWs it is necessary to confine the photonic field across the QWs sufficiently long that multiple exciton absorption and emission cycles can occur before the photon escapes the cavity. A typical high Q-factor cavity used to achieve this consists of DBRs either side of a microcavity spacer that contains a series of QWs around the anti-nodal positions of the confined field. Using multiple QWs to confine excitons allows for a higher exciton density within the cavity, increasing the coupling strength, whilst remaining below the exciton saturation density/ Mott transition [57].

The work presented in the thesis is carried out on two samples grown via molecular beam epitaxy (MBE). The first sample studied is a high-Q $5\lambda/2$ $Al_{0.3}Ga_{0.7}As$ microcavity with four sets of three 10nm GaAs QWs inside the cavity, each set centred around an anti-nodal position of the confined field. The cavity spacer is capped either side with DBR stacks consisting of $AlAs/Al_{0.15}Ga_{0.85}As$ pair layers, 32 on the top and 35 on the bottom all grown on a GaAs substrate. The resulting sample has a Q-factor of > 16000 and a Rabi splitting of 9meV [58]. It was designed by P. G. Savvids and S. Tsintzos and grown by Z. Hatzopoulos in the Microelectronics Research Group (MRG) of the Foundation of Research and Technology (FORTH) in Crete.

Whilst MBE enables high quality growth, lattice constant mismatch between the various layers leads to strain that subsequently causes various defects within a sample's anatomy. These defects can impinge on the extended propagation of polaritons or the feasibility of creating minimally perturbed lattices of coupled condensates. Lattice mismatch and the resulting strain restricts the number of pair layers of the DBRs that can be grown, while keeping deformation to a minimum, ultimately limiting the cavity lifetime. Therefore, the second sample studied includes a phosphorous doping in the AlAs layers of the DBR

stacks to compensate for the mismatch and alleviate the strain. The sample consists of a 2λ GaAs cavity with three pairs of 6nm $In_{0.08}Ga_{0.92}As$ QWs at the anti-nodal positions of the confined field with an additional QW at the first and last node of the cavity field. The DBRs are formed of 23 (26) pair layers of $GaAs/AlAs_{0.98}P_{0.02}$ on the top (bottom) of the cavity. The resulting experimental Q-factor is $\sim$ 12000 with a Rabi splitting of 8meV [9]. Again the sample is grown on a $GaAs$ substrate but due to the use of $InGaAs$ QWs the lower polariton branch is red shifted below the bandgap energy of $GaAs$, consequently the substrate is transparent to the corresponding photoluminescence, meaning the sample can additionally be probed resonantly from either the epitaxially grown side or through the substrate. This sample was designed and grown under the direction of P. G. Lagoudakis and W. Langbein.

2.2 Excitation

2.2.1 Excitation regimes

2.2.1.1 Resonant/Quasi-resonant excitation

Resonant excitation is an optical excitation technique that matches both the energy and in-plane momentum (equally excitation angle) of the final polariton state. Under resonant excitation the final state cannot be classified as a condensate, rather it is a coherent ensemble of polaritons. This is because the phase of the condensate wavefunction is inherited from the excitation laser rather than determined through spontaneous symmetry breaking during a phase transition.

Quasi-resonant excitation is similar, except one does not exactly match the energy and/or angle of the excitation beam with the final polariton state. One form of this excitation (at zero in-plane momentum) involves pumping with the laser slightly blue detuned from the bottom of the lower polariton branch. Under this regime, as the polariton population grows, the blue shift resulting from the non-linear interactions of polaritons causes the lower polariton branch to become resonant with the excitation beam. Another form of quasi-resonant excitation, which results in a condensate, is to excitate the lower polariton branch resonantly but at a high angle of incidence (in-plane momentum). Due to the phase distorting scattering processes during the transition from the injected free carriers to the final polariton state, the phase of the final polariton state is not related to the phase of the excitation laser.

2.2.1.2 Non-resonant excitation

Non-resonant excitation involves injecting a plasma of free charge carriers, which through phonon mediated channels of relaxation, form a hot exciton reservoir that feeds states on

the lower polariton branch. As the pumping density is increased a threshold condition is crossed in which the scattering into the final polariton state exceeds the losses and a coherent condensed state is formed. As described in the Section 1.2.2, the onset of coherence formation across the polariton cloud corresponds to the onset of off-diagonal long range order, which is a definitive indication of condensation. Again, through the relaxation process with a significant number of scattering events, the phase of the final condensed state is unrelated to the excitation source. The initial plasma can be injected either electrically or optically. Herein, only non-resonant optical excitation is discussed as electrical injection in not used in the work presented; though the general physics doesn't significantly differ between optical and electric injection.

To optically excite a plasma of free charge carriers, a laser energetically above the bandgap of the active material (the QWs) and also above the photonic stopband of the microcavity structure is used. The purpose of blue detuning above the cavity stopband is to maximise the coupling of the pump laser into the cavity and thus quantum wells. The excitation source used throughout is a single mode narrow linewidth tuneable Ti:Sapph laser with etalon locking to prevent mode hopping and external reference cavity locking to bring the linewidth to < 75kHz. The plasma of free charge carriers interact with optical phonons (OP) to relax into Coulomb correlated electron-hole pairs (excitons). As discussed in Section 1.1.1.1 there are optically accessible (bright) excitons with a spin of ± 1 and optically inaccessible (dark) excitons with a spin of ± 2. The bright exciton dispersion itself though can be separated into two regimes, the regime with an in-plane momentum that can be matched by photons at a given angle $< \pi/2$ with respect to the normal of the samples surface (i.e. within the light cone) and the regime which cannot couple to light because the in-plane momentum is larger than optically accessible.

Excitons outside of the light cone, with high in-plane wavevector $k_{||}$, relax towards optically active states in and around the reciprocal space trap of the lower polariton branch through acoustic phonon (AP) interactions. The AP interactions dissipate energy from the exciton cloud into the crystal lattice, thermalising the exciton cloud to some extent. However, AP interactions are inefficient, requiring multiple interactions to dissipate $\sim$ 10meV and taking $\sim$ 100ps. Fortunately, due to the initial states being outside of the light cone there is no radiative decay and so the exciton lifetime is long enough to make this relaxation process sufficient [21]. As the energy and $k_{||}$ decrease, the excitons begin to be able to hybridise with photons to form polaritons, but this also introduces radiative decay which dramatically reduces the lifetime. This leads to the build up of an energetically hot, incoherent reservoir of particles. The reservoir is often referred to simply as the hot-exciton reservoir because, for this region of $k_{||}$, the lower polariton branch asymptotically approaches an exciton contribution of 100%; see Figure 1.5. The inefficiency of acoustic phonon mediated relaxation combined with the reduced particle lifetime, due to radiative decay, necessitates that other interactions

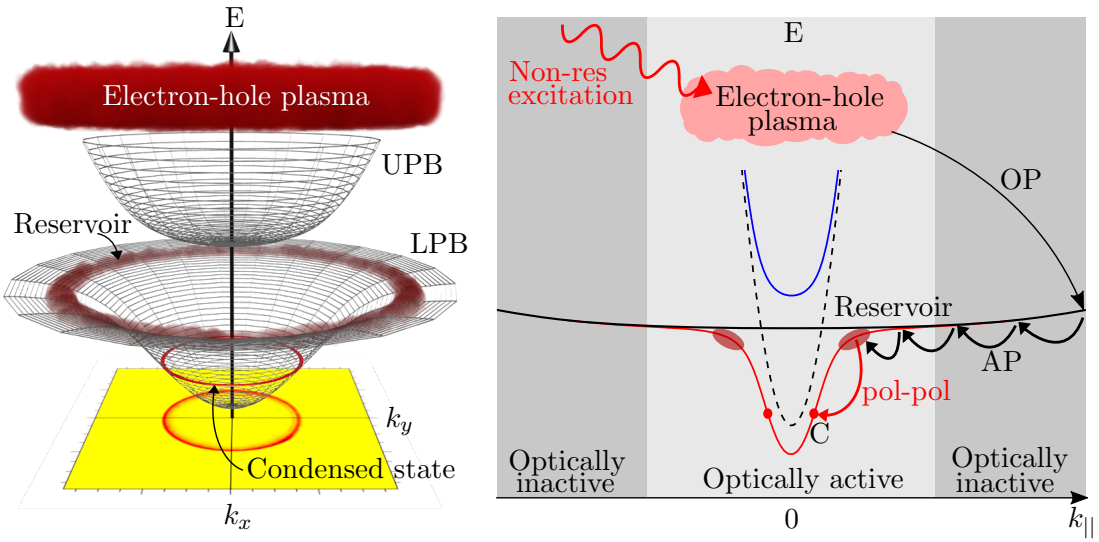

FIGURE 2.1: Left: Three dimensional schematic of the lower polariton branch (LPB), upper polariton branch (UPB) dispersions along with the free charge carrier plasma, exciton reservoir and final condensed state. The projection of the condensed state as measured experimentally in Fourier space is shown on the lower plane. Right: Schematic demonstrating the process of non-resonant excitation and relaxation processes resulting in the final condensed state (C), where OP - optical phonon mediated relaxation, AP - acoustic phonon mediated relaxation, pol-pol - polariton pair scattering. Red (blue) solid lines - LPB (UPB), black solid (dashed) line - exciton (cavity) dispersion. The light gray background denotes the region within the light cone and the dark gray background denotes the optically inaccessible region. Note the condensed states in the schematics are for freely propagating/expanding polariton condensates; see Section 2.2.2.

such as polariton-polariton scattering become the dominant source of relaxation from the exciton-reservoir to the lower energy states of the LPB.

At cryogenic temperatures the diffusion length of excitons is small, meaning the hot-exciton reservoir is localised to the spatial geometry of the excitation beam. This produces a potential landscape that favours scattering into a particular set of states on the LPB with a well defined $k_{||}$ that is not necessarily zero. Once losses from these favoured states are surpassed by the scattering into them (gain), Bose stimulated scattering to the final state produces a condensate with a spontaneously selected phase, described well by a macroscopic wavefunction. This non-resonant excitation and relaxation process is depicted in the schematics of Figure 2.1.

2.2.2 Excitation spatial geometry

The existence of a hot-exciton reservoir under non-resonant excitation affords a highly tunable method of sculpting 2D potential landscapes, thanks to strong interactions between polaritons and excitons (pol-ex). The other widely implemented technique to imprint arbitrary potential landscapes is through the micro-structuring of mesas on the planar sample [59, 60]. The downside to micro-structuring is the resulting potential is permanent, and so any variation in lattice shape, lattice constant, depth of potential etc

requires a new section of sample to be processed, at great cost and with slow return time. Optically imprinting the potential landscape allows for the configuration to be changed in live time using the same section of the planar sample. The upside of micro-structuring is the potential landscape is effective even at pump powers significantly below threshold allowing, for example, the observation of band structures in the linear regime (below condensation threshold) as well as the condensed regime [61,62]. As the work conducted during my PhD candidature is only concerned with optically imprinted geometries, these shall exclusively be considered herein. Within the optically imprinted potential landscapes there are two categories of polariton condensate that can be formed, trapped and freely expanding.

In the trapped regime a potential landscape incorporating a local minimum is imprinted. Polaritons formed in the region between this minimum in potential and the surrounding maximal potential isopleth, ballistically travel towards the minimum. Polariton-polariton scattering in this enclosed region leads to the formation of a cooled polariton condensate [63]. As one would expect, such a system can be envisaged as a particle in a finite potential box with various modes of trapped polariton condensates that can be formed depending on the exact geometry and magnitude of the 2D potential landscape imprinted. The supported modes for annular traps include modes similar in shape to the different Hermite-Gauss modes [1, 63–65] or Laguerre-Gauss modes [66]. The trapped state to condense first is that which has the largest net gain through maximising overlap with the reservoir. The final condensed state resides inside the dispersion of the propagating polaritons, in the region around $k_{||} = 0$ and not on the free particle dispersion; see Figure 2.2(a).

Conversely, in the freely expanding regime, the polariton condensate is spatially coincident with the pump (and reservoir); such regimes include Gaussian pump profiles. The potential hill landscape formed by the reservoir causes condensed polaritons to ballistically propagate outwards with a well defined $k_{||}$ that is not equal to zero. The final condensed state lies on the dispersion of (lower) free polariton branch, see Figure 2.2(b). Examples of the type of potential landscapes formed in both regimes are shown in Figure 2.3.

Each of the spatial geometries have features which are beneficial over the other in particular circumstances. For example, in the case of the trapping potential, the hot-exciton reservoir is spatially separated from the final condensed state, demonstrably reducing the decoherence inducing and spin mixing polariton-exciton interactions [63,67,68]. This has enabled the first observation of polariton bistability under non-resonant excitation in the absence of external perturbing fields, see Chapter 3 [1], as well as strongly enhanced polariton condensate coherence times, see Chapter 4. The benefit of the freely expanding regime is the ability to couple multiple spatially separated condensates in arbitrary configurations [69, 70]. As will be demonstrated, in Chapter 5, with freely expanding condensates coherent coupling across macroscopic distances far exceeding an order of

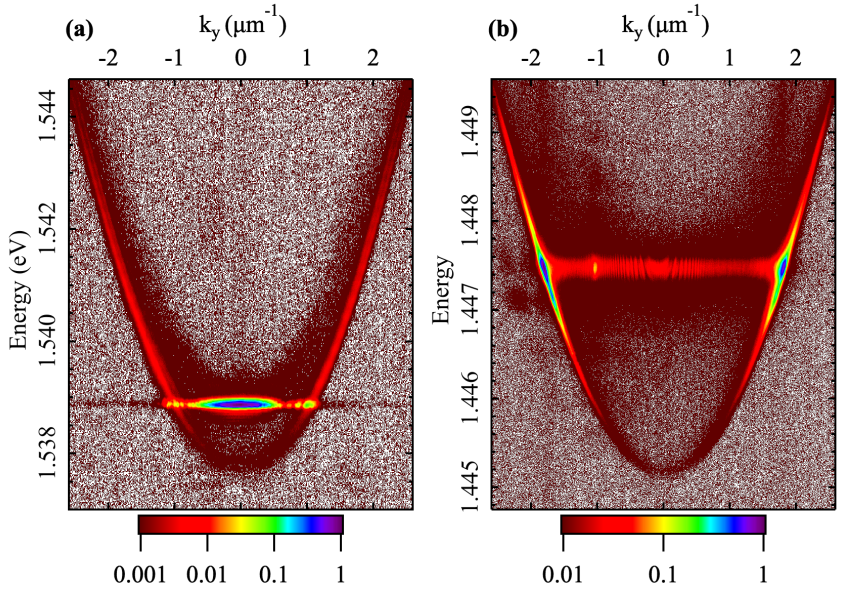

FIGURE 2.2: (a) Dispersion from a ground state trapped polariton condensate using an annular pump profile on the GaAs sample. (b) Dispersion from a freely expanding (non-trapped) polariton condensate on the InGaAs sample.

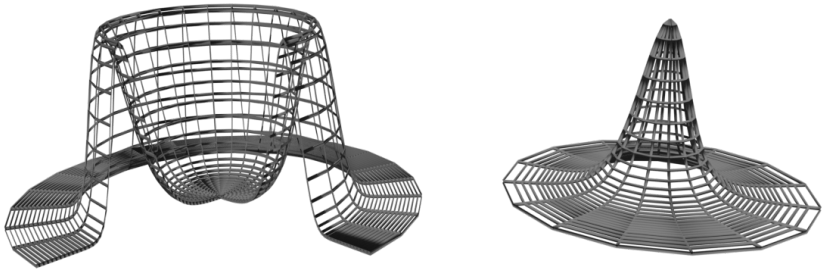

FIGURE 2.3: Potential landscape due to the exciton reservoir in the (left) trapped regime, where a section has been removed to view inside and (right) freely expanding, Gaussian excitation regime.

magnitude larger than the FWHM of the pump spots is possible; see Figure 5.1. The flux of coherent particles from one condensate centre to the other additionally has the effect of reducing the threshold pump density for each condensate.

2.3 Spatial modulation of light

To be able to produce arbitrary potential landscapes optically, one needs to be able to sculpt the intensity pattern of the excitation beam. For certain 'simple' pump geometries one can use traditional optics; lenses, axicons, masks etc. But to truly harness the power of the optically injected potential it is much more useful to use a highly adaptable computer controlled beam shaper. There are numerous forms of device that can achieve

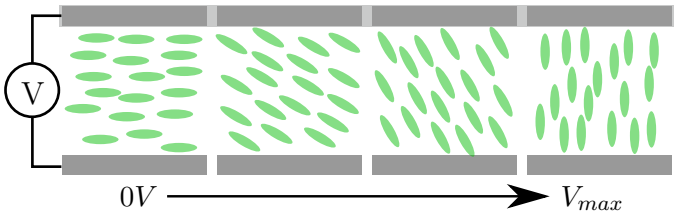

FIGURE 2.4: Electrically addressable parallel aligned calamitic liquid crystal cells with the alignment layers horizontal in the plane of the page. From left to right each cell shows the LC alignment for increasing potential differences between the contacts from 0V (left) to the state with maximum phase perturbation corresponding to V_{max} (right).

this desired controllability and they are grouped under the term spatial light modulator (SLM). There are amplitude modulation SLMs that directly change the spatial intensity pattern of the beam illuminating the SLM, for example digital micro-mirror arrays which are effectively reconfigurable masks. There are then phase modulating SLMs that instead imprint a 2D phase profile onto the illuminating beam which when Fourier transformed (equivalently focused through a lens) results in the desired intensity profile. For example where a beam F_{in} is incident on the SLM, an Amplitude modulating SLM multiplies the incident beam by a spatially varying term $A(x, y)$, whilst the term $e^{i\cdot\phi(x,y)} = 1$ (i.e. $\phi(x, y) = 0 \ \forall \ x, y$). A phase modulating SLM, on the other hand, cannot modulate amplitude directly thus $A(x, y) = 1 \ \forall \ x, y$, but imprints a non-zero phase term $\phi(x, y)$[1]:

$$F_{out}(x, y) = A(x, y) \cdot F_{in}(x, y) \cdot e^{i\cdot\phi(x,y)}. \tag{2.1}$$

Under non-resonant excitation there is complete freedom over the phase of the excitation laser, as the lasers phase is lost through multiple scattering events during the relaxation process. Therefore, it is possible to use any of the forms of SLM mentioned above. The micro-mirror array type of amplitude SLMs mostly use digital control over each pixel, which is to say each pixel is either in an 'on' or 'off' state and only has displacement in one axis. This consequently limits the maximum efficiency and resolution of the device as it is effectively applying a mask to the incident beam deflecting regions, that aren't of interest, out of the optical path. The most flexible and high fidelity spatial modulation, as used throughout the work presented, is achieved using phase-only liquid crystal on silicon (LCOS) SLMs with a resolution of 1920x1080 pixels.

LCOS phase-only SLMs have a series of electrically addressable pixels with a parallel aligned nematic liquid crystal (PAN-LC) cell between the contacts, similar to the form shown schematically in Figure 2.4. A nematic LC has a degree of rotational symmetry, defined by the azimuthal and polar angle which the long axis of each molecule (for calamitic LCs) makes to a reference axis, but demonstrates no positional symmetry.

[1]Note a phase modulating SLM could also be used in conjunction with polarisers to be implemented as a direct amplitude modulation. But in general this technique is not as flexible.

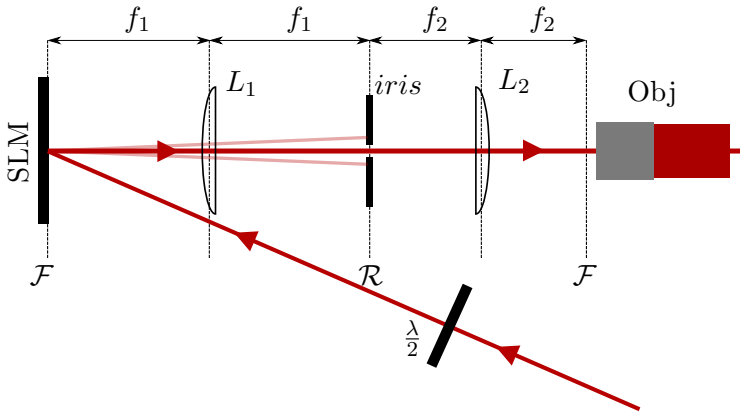

FIGURE 2.5: 4F configuration used with the SLM and microscope objective lens. Where f_1 is the focal length of the lens L_1, f_2 is the focal length of lens L_2, iris - controllable aperture for spatial filtering of diffracted modes, Obj - microscope objective lens, SLM - spatial light modulator and $\lambda/2$ - half wave plate. $\mathcal{F}$ and $\mathcal{R}$ correspond to the Fourier planes and real space planes of the system.

The molecular polarisabilities along the long and short axes of the molecules differ, consequently in the nematic phase the refractive index is different in the direction of the rotational symmetry vs the direction parallel to it [71]. A PAN-LC incorporates, for example, calamitic molecules (cylindrical volume filling) in a nematic phase sandwiched between two parallel alignment layers.

Looking at Figure 2.4 the cells, from left to right, have different optical thicknesses (and thus phase retardance) for a linear polarisation parallel to the horizontal axis (width) of the page (i.e. parallel to the alignment layers). Whereas the orthogonal linear polarisation (perpendicular to the width of the page) will see no notable difference in optical path length between the left most and right most cell. The SLMs used are produced with alignment layers to retard the phase of the linear polarisation parallel to the long axis of the (rectangular) screen. Additionally the SLMs used are 8-bit addressable and calibrated such that a 0π phase delay corresponds to a pixel value of 0 and a 2π phase delay corresponds to a pixel value of 255, with as close to a linear response of the phase delay vs pixel value as possible.

As phase-only SLMs imprint an arbitrary phase map they are placed at the Fourier plane of the optical excitation path. A 4F system is then used to project the surface of the SLM (the Fourier plane) onto the rear focal plane of an microscope objective lens that then focuses the desired real space image on the samples' surface. An iris is used at the real space plane after the first lens, following the SLM, to select the first order diffracted mode and filter out the zeroth (un-diffracted) and higher order diffracted modes, see Figure 2.5.

2.3.1 Phase map/Kinoform calculations

To produce an arbitrary spatial geometry via a phase-only SLM from, for example, a Gaussian laser beam, it is necessary to calculate the spatial phase map (kinoform) that needs to be imprinted. There exist a number of techniques used to make these phase maps from the knowledge (or approximation) of the amplitude map of the beam hitting the SLM, the desired spatial geometry and an initial guess at the required phase map. As the theory of this topic that has had some in-depth discussions previously [72, 73] I will discuss only the techniques used here and will highlight some of the experimental difficulties in implementing them along with how the problems were overcome.

Broadly, the techniques for phase calculation can be split into two categories, those which use analytically calculable solutions or a sum (modulo 2π) thereof and those which make use of iterative techniques transforming between the spatial and momentum Fourier related planes (Helmholtz propagation can also be used instead of Fourier transforms).

2.3.1.1 Analytic

A spatial geometry implemented many times during the work presented in this thesis is that of an annulus. An annulus can be formed by imprinting an analytic kinoform with a phase delay that linearly increases with the radius from the centre of the SLM screen. The gradient of the resulting ramp in phase delay defines the diameter of the annulus produced. Due to the cyclic nature of phase (i.e. $0\pi = 2\pi$) this linear radially changing phase delay results in a circularly blazed grating. The axicon kinoform can be further restricted to only allow phases of 0 and π resulting in the so called binary axicon. The binary axicon produces sharper and more symmetric profiles of the resulting annular excitation geometry and is the form used through out.

For other simple geometries a clean laser image can be produced by using the sum (modulo 2π) of the kinoforms that would create each constituent element. This technique works well for simple configurations, however when the desired intensity profile becomes more complex the technique fails to produce usable pump profiles. Figure 2.6 shows the resulting experimental laser profiles for a pentagon (a) and a 5x5 square lattice (b) utilising the sum of kinoforms technique. The 'ghost' spots for the pentagon laser profile are significantly lower in intensity than the desired pump spots and so the laser profile is usable. Conversely, for the square lattice, the resulting laser profile shows an additional layer of comparatively bright spots (i.e. it gives a 7x7 lattice rather than 5x5), whilst the intensity of the inner spots are greatly suppressed. This effect is expected to be due to the locations of multiple ghost spots (higher orders) being spatially coincident in particular locations making them comparatively bright and ultimately resulting in the intensity map being entirely unusable.

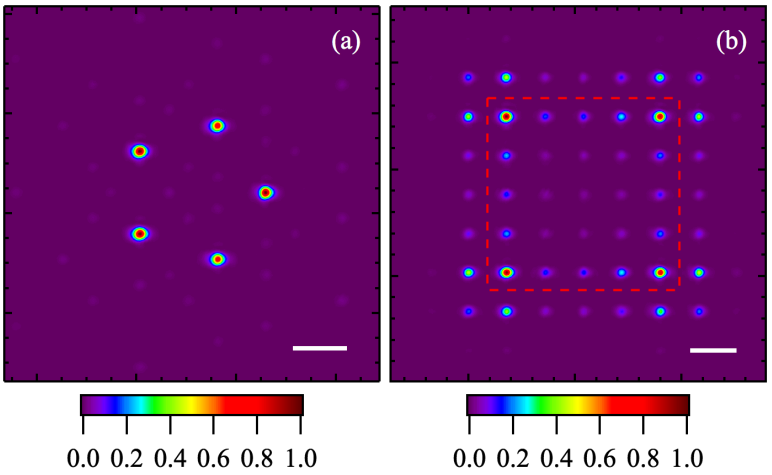

FIGURE 2.6: Experimental laser profiles using kinoforms produced by the sum of linear gratings with desired geometries of (a) pentagon and (b) 5x5 square lattice. The solid white lines in the bottom right corner of both (a) and (b) correspond to 15μm. The red dashed box in (b) surrounds the region that corresponds to the desired geometry, the points outside this box are artefacts of the kinoform production technique.

Beyond the analytic kinoforms used to create the laser pattern desired, there are a series of analytic Zernike polynomial kinoforms. The first order Zernike polynomials are just linear gratings that displace the first order diffraction pattern (which produces the desired geometry) from the un-modulated zeroth order reflected beam. Second order and higher Zernike polynomials allow for correction of small aberrations introduced by the optical elements. For example one of the second order Zernike polynomials consists of a radially quadratic phase front that acts as an effective lens. This can compensate for example, small changes in the optical path length between the SLM and microscope objective lens[2]. All kinoforms used here, analytic and iteratively calculated, incorporate at least first order Zernike polynomials via addition modulo 2π.

2.3.1.2 Iterative techniques

For more complex geometries including ones with extended shapes and lattices, simple analytic solutions are either not possible or do not result in good laser profiles. Therefore, it is necessary to implement the iterative approximation techniques which are closely related to the phase retrieval procedures developed in electron microscopy and x-ray crystallography. Of the different versions of these algorithms the two techniques used here are Gerchberg-Saxton (GS) and Mixed Region Amplitude Freedom (MRAF) [73]. The simpler of the two is an adaptation of the GS algorithm developed in 1971/1972 for

[2]Such optical path length changes could be the result of the addition of polarising optics/filters etc. and this Zernike polynomial prevents the need to reposition the lenses.

electron microscopy [74]. The procedure used can be summarised by the following list and flow-chart (Figure 2.7) (all maps depend on the spatial indices x and y, corresponding to the SLM pixels but these indices are dropped at points in the following for brevity):

1. To start one requires the knowledge of the following three fields. (1) The amplitude map of the beam incident on the SLM ($|E_{ini}|$). Generally it is not necessary to image the beam profile projected onto the SLM screen at the beginning for this step, rather the beam can be approximated by a Gaussian of suitable width[3]. (2) The amplitude map of the desired target geometry, A_0, which is just the square-root of the intensity map I_0. (3) Finally an initial guess at the phase map required to modulated the incident beam to be as close as possible to the desired target.

2. Multiplying $|E_{ini}|$ with the complex exponential of the initial phase map ($e^{i\phi_{ini}}$) gives the first input field in the algorithm $E_{in}^{(0)}$. The purpose of the initial phase guess, which generally contains something like a quadratic phase - having the effect of a lens, helps the algorithm converge on a result quickly and with maximal fidelity.

3. A fast Fourier transform of $E_{in}^{(i)}$ (where i is the iteration step) is then calculated to determine the output field (from which the predicted output intensity map can be calculated).

4. An intermediate field $G^{(i)}$, that combines the targets amplitude map with the phase from the output field $E_{out}^{(i)}$, is then calculated.

5. A new input field $E_{in}^{(i+1)}$ is created combining the incident beams amplitude and the phase map that is the argument of the inverse Fourier transform of $G^{(i)}$. It takes this form because we can only modulate the phase and not the spatial amplitude directly.

6. This marks the end of one iteration and determination of whether further iterations are carried out must be made. If further iterations are required go to step 3 with $E_{in}^{(i+1)}$. Otherwise the required kinoform is the argument of the complex field $E_{in}^{(i+1)}$.

[3]Of course this is assuming the beam is nearly Gaussian, at least around the most intense region.

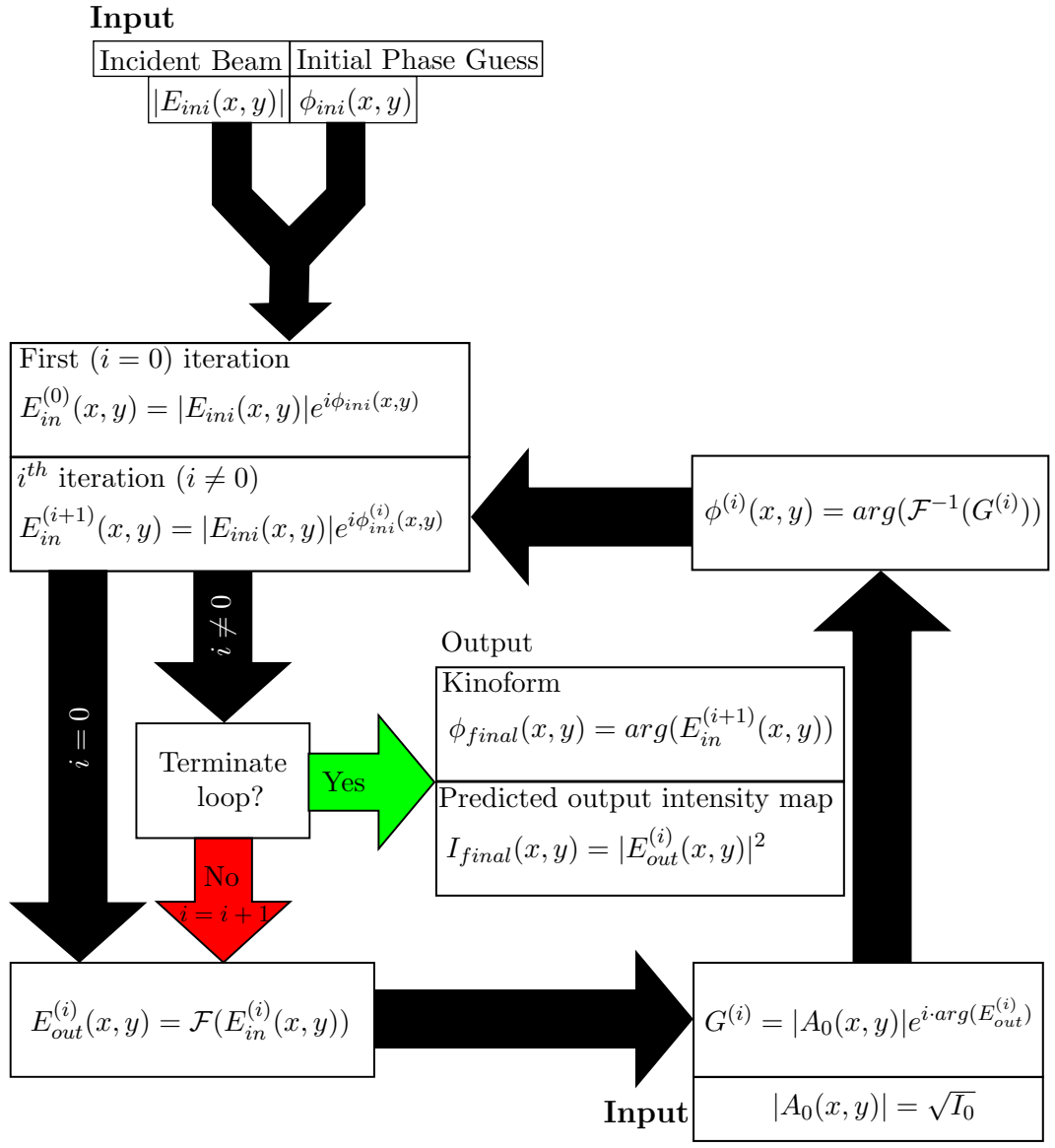

FIGURE 2.7: Flow diagram showing the Gerchberg-Saxton phase retrieval technique. $|E_{in}(x,y)|$ is the amplitude of the beam incident on the SLM, $\phi(x,y)$ is the initial guess at the phase required to modulate $|E_{in}(x,y)|$ into the desired intensity target $I_0(x,y)$ $(A_0 = \sqrt{I_0})$ at the Fourier transform of the output field $E_{out}(x,y)$.

For many applications GS is a perfectly adequate procedure, producing clean experimental laser profiles. For regimes where GS fails to produce clean laser profiles the next option is MRAF. In MRAF the target intensity map is split into two regions, the signal region (SR) and noise region (NR)[4]. In the NR the algorithm applies no constraints on either the phase or amplitude of the fields, in the SR there is only phase freedom and the output field intensity map converges closely to the target intensity map. There is a constant mixing parameter M $(0 < M \leq 1)$ introduced that relates to the split in intensity between the SR and NR. A smaller M results in a higher fidelity profile in the

[4]The regions should be chosen such that there is minimal to no intensity in the NR of the target.

SR but with reduced intensity in the SR. As M is increased the intensity in the noise region is decreased but at the cost of the fidelity of the resulting laser pattern in the SR[5], see Figure 2.8. With the addition of the mixing parameter, it is necessary to adjust the intermediate function $G^{(i)}$ for MRAF. The intermediate functions for MRAF and GS are:

$$\begin{aligned} G^{(i)}_{MRAF} &= (m\sqrt{I_0}|_{SR} + (1-m)|E^{(i)}_{out}|_{NR}) \cdot e^{i \cdot arg(E^{(i)}_{out})} \\ G^{(i)}_{GS} &= \sqrt{I_0} \cdot e^{i \cdot arg(E^{(i)}_{out})} \end{aligned} \tag{2.2}$$

where subscripts (SR and NR) denote the regions in which each term is to be calculated. There is one additional constraint that must be enforced in MRAF due to the mixing parameter, the integrated power in the SR of the target and the mixing parameter normalised integrated power across the whole output plane must remain constant in each iteration [73]:

$$\begin{aligned} \Sigma_{SR} I_0 &= constant \\ m\Sigma_{SR}|E^{(i)}_{out}|^2 + (1-m)\Sigma_{NR}|E^{(i)}_{out}|^2 &= constant. \end{aligned} \tag{2.3}$$

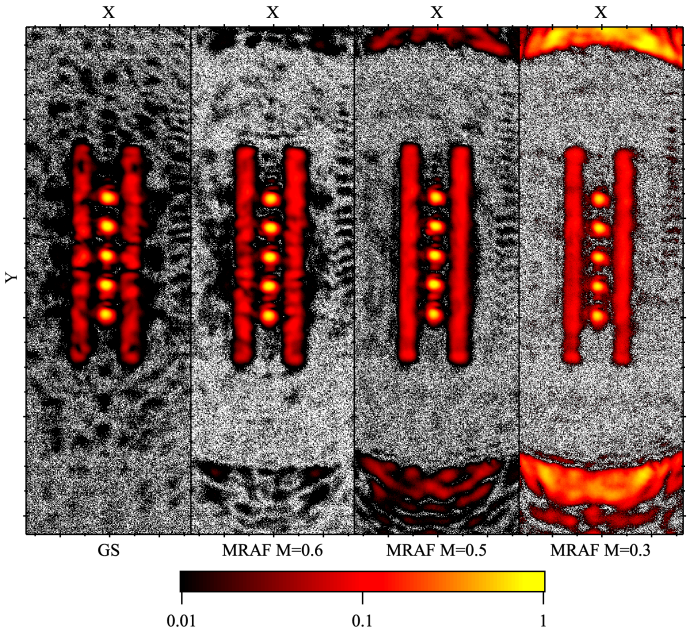

FIGURE 2.8: Experimental real space laser images of five Gaussian spots between two solid barriers with the kinoforms calculated using GS (left) and MRAF (the three on the right) with reducing mixing parameter going to the right.

[5]When $M = 1$ and the SR and NR are selected so that there is zero intensity in the NR of the target intensity map, then MRAF effectively becomes GS.

The normalisation of the SR of the target only needs to be computed once at the beginning of the calculation and the normalisation of $E_{out}^{(i)}$ is computed before calculating $G^{(i)}$ for each iteration. To minimise computational time, incorporating arrays (defined once at the beginning of the calculation) that mask out the SR and NR, negates the need of rastering the entire arrays (maps) each time $G_{MRAF}^{(i)}$ is calculated or the normalisation is conducted. This significantly reduces the time taken per iteration and for the array sizes used is not a problem for a computer with moderate RAM. Even though the differences in calculation between GS and MRAF are small, experimentally the resulting laser pattern fidelity can be vastly different; as is shown in Figure 2.8 and the following section. The heart of the improvement is from the separation of the fields into a SR, in which one requires a strong amplitude convergence to the target, and a NR in which no constraints on amplitude are made.

2.3.2 Comparison of GS and MRAF

As suggested above, iterative techniques such as GS and MRAF only need to be implemented in instances where the desired target geometry contains extended shapes and/or extended lattices which lead to strong ghost spots. However, which iterative technique should be used is an additional question that requires consideration of the required fidelity and efficiency. For lattices of Gaussian-like points, GS is perfectly adequate; particularly when coupled with the relative intensity stabilisation (see Figure 2.9(a)), as will be described in the next section.

However, should the pattern include any extended non-Gaussian like shapes, then GS will generally create a significantly speckled pattern, whereas MRAF can produce a much smoother profile; but at the cost of efficiency. An example of the experimental laser profiles for a system of five Gaussian spots between two solid barriers of controllable height, using kinoforms calculated with GS and MRAF, are shown in Figure 2.9 (b & c respectively).

2.3.3 Relative Intensity Stabilisation

Even with all of the choices of kinoform calculation, highlighted above, including the Zernike polynomial corrections, there are unavoidable aberrations that stem from e.g. sample defects or a non-ideal phase front of the beam incident on the SLM etc. To actively and automatically compensate for these, a relative intensity stabilistion technique has been designed and implemented. Note that this relative intensity stabilisation (herein called active stabilisation (AS)) works only in conjunction with the iterative Fourier transform kinoform calculation technqiues.

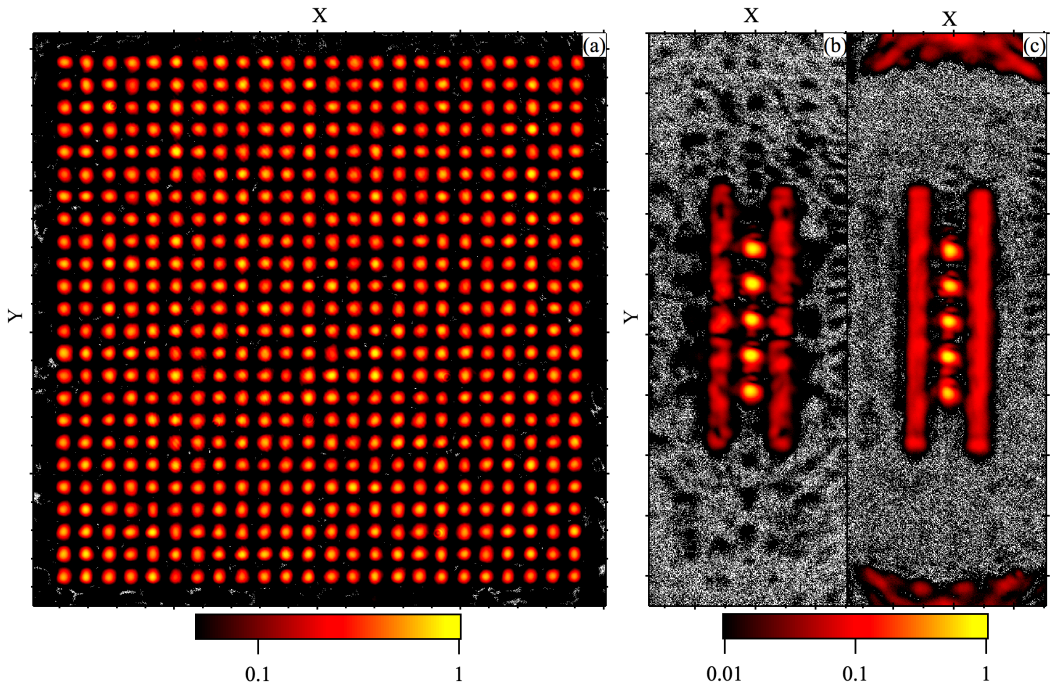

FIGURE 2.9: (a) 576 Gaussian pump spots arranged in a square lattice with the kinoform calculated using GS. (b) 5 Gaussian pump spots between 2 barriers, that in the target intensity profile are smooth, kinoform calculated using GS. (c) Same target intensity profile as in (b) but the kinoform is calculated using MRAF with a mixing parameter $M = 0.5$. Note in all of the above images relative intensity stabilisation, as described in section 2.3.3 is implemented.

The AS technique utilses a camera imaging the samples surface, where each pixel has been mapped onto the corresponding region of the target image. This allows the comparison of the experimentally realised laser geometry with the ideal target. A new target is made considering the deviations measured between the experimentally realised laser profile and the desired target, following which a new kinoform is produced and then the resulting experimental intensity map is again compared to the ideal target. This sequence repeats until the deviations fall below a preset threshold condition.

The comparison between the experimental intensity map and the ideal target can take several forms depending on the goal. If pumping with Gaussian-like spots and the goal is to make all spots equal, then the simplest form of correction is to measure the integrated or peak intensities in the regions around where each spot is meant to be located and then change the amplitude of each spot in the next target by an amount proportional to the deviation from the mean. If an unequally pumped regime is desired, then the system can compare the relative measured intensities (integrated or peak) to the relative intensities in the ideal target and apply corrections scaled to these. When the excitation is not formed from a series of Gaussian-shaped, spots it becomes necessary to interpolate the experimentally measured intensity map to match the dimensions of the ideal target, then

a pixel by pixel comparison and correction can be made. In all of the work presented here it has not been necessary to go beyond equalising the intensity of all of the spots.

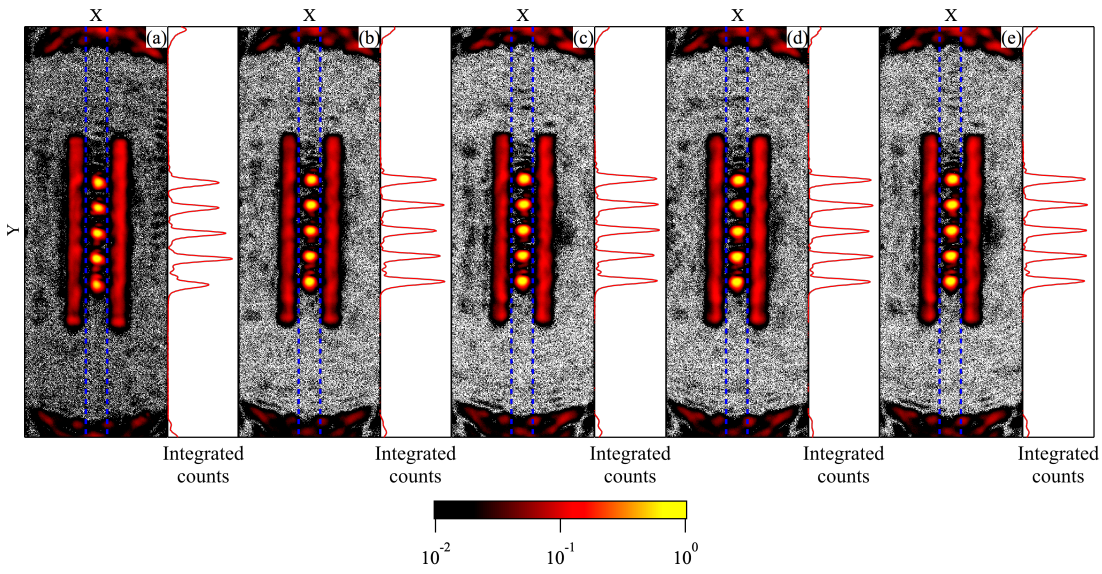

FIGURE 2.10: Real space images of the experimental laser profile for five spots with solid boundaries either side that have a peak intensity $\sim 40\%$ of the spots. Line profiles calculated between the two vertical blue dashed lines is shown on the right of each real space image. (a) Depicts the resultant laser profile after one run of MRAF with M=0.5 using 20 iterations, (b) shows the laser profile after one iteration of the active stabilisation (AS) to equalise the peak intensity of the 5 spots, (c) laser profile are two iterations of AS, (d) three iterations of AS and (e) five iterations of AS.

The AS technique is very effective at stabilising the intensity across many laser spots reducing the deviations dramatically; see Figure 2.10 & 2.11. The cost of the technique is of course the time taken for each desired pump geometry to be created with the desired intensity stabilisation. In the earliest versions of AS that I wrote, the calculations were executed by the central processing unit (CPU) and would take $\sim 30 - 60$seconds per full iteration, each of which consists of however many iterations of the MRAF or GS algorithm used. For some targets the system converges to the final kinoform in very few iterations. For example in Figure 2.10 the experimental laser intensity maps of the five Gaussian pump beams between two solid linear barriers is shown at each step across five iterations of AS resulting in very uniform intensities. However, other target geometries are not so quick to converge and a preset cut off number of AS iterations may be crossed before the measured deviations fall below a set tolerance limit (this cut off number is set due to computation time but can be manually overridden if desired). So whilst AS is effective (see Figure 2.10) it made real world probing of large numbers of large pump geometries time consuming. My colleague J. D. Toepfer has since written the iterative Fourier transforms algorithms and feedback procedures to be executed on the graphics processing unit (GPU) which reduces the calculation time by orders of magnitude allowing for hundreds/thousands of iterations to be computed quickly.

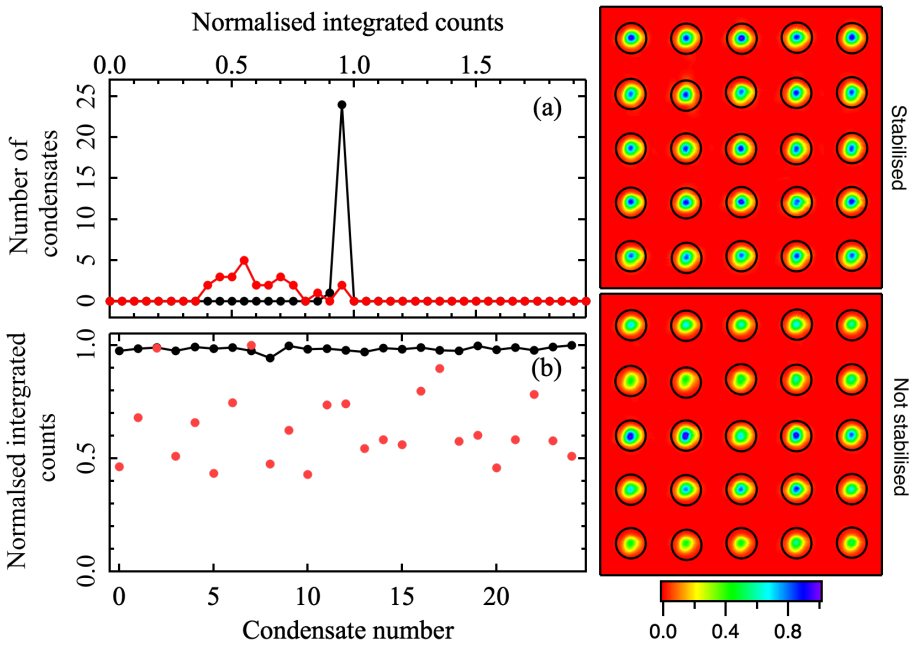

FIGURE 2.11: Demonstration of the effectiveness of the relative intensity active stabilisation techniques employed on a 5x5 square lattice. (a) histogram of the normalised integrated counts of the stabilised (black spots) and not stabilised (red spots) pump for the regions within the circles on the two real space images to the right. (b) Normalised integrated counts for each of the 25 pump spots from which the histogram in (a) is produced, black spots - stabilised and red spots - not stabilised.

Therefore, it is possible to traverse large sets of pumping geometries with this intensity stabilisation active.

2.4 Temporal modulation of excitation

To prevent sample heating from the CW excitation beam it is necessary to modulate the intensity temporally. One technique is to use a chopper wheel of a desired on-off ratio spinning at a given frequency. Generally however, it is necessary to modulate the beam faster than typical single chopper wheels can achieve (typically $\sim$ 10kHz with $1-5\%$ duty cycle is used) therefore other techniques are employed. The simplest and most powerful/flexible technique is to use either an electro-optic modulator (EOM) or an acousto-optic modulator (AOM) relying on the electro-optic or acousto-optic effect respectively. In the following, discussion is limited to AOMs as these are what were implemented here. It should be noted that although the time the laser is 'on' is short, due to it being orders of magnitude longer than the lifetime of the polaritons it can still be considered CW and is often given the term quasi-CW to reflect the temporal modulation.

An AOM consists of a transparent crystal that on one edge has a piezoelectric transducer driven by a radio frequency (RF) source, this drives longitudinal pressure waves inside the crystal perpendicular to the lasers optical axis. The acoustic wave spatially modulates the refractive index of the crystal (Acousto-Optical effect) producing a diffraction grating. The diffraction efficiency of the grating is directly controllable via the amplitude of the RF wave, which is in turn controlled by the voltage driving the AOM controller. Therefore, it is possible to not only 'chop' the excitation beam, one can temporally shape the intensity of the laser into arbitrary patterns via a function generator. It should be noted that whilst the diffraction efficiency follows the driving voltage, the response is not perfectly linear across the voltage range applicable, particularly towards the region of large driving voltages where the diffraction efficiency saturates.

As one of the key reasons for chopping the beam is to prevent sample heating, the first diffracted order is used to excite the system due to it high extinction ratio in the off state. One could equally use zeroth diffracted order to access more power in the 'on' state, but the 'off' states suffers a much lower extinction. It is possible to achieve up to $\sim 80\%$ diffraction efficiency into the first order, so generally the cost in efficiency is tolerable[6].

2.4.1 Global intensity stabilisation

As AOMs are directly and arbitrarily controllable, they can also be used in an active stabilisation of the global intensity to compensate for laser fluctuations and/or mechanical vibrations altering the excitation density on the sample. Due to the pump laser being locked to a single cavity mode (monomode operation) with a very narrow linewidth (< 75kHz), intensity fluctuations are small. One of the primary sources of fluctuations is the mechanical connection between the liquid He dewar and the banjo flow cryostat.

Whilst the system is built to minimise the existence of these vibrations, it is not experimentally feasible in our case to remove them entirely. To combat the remaining fluctuations a feedback system was built that monitors the global intensity of either the PL or laser in the collection path after the sample. It compares the voltage from the measured intensity to a reference signal and through the use of OpAmps and a PID loop gives a feedback to the voltage train driving the AOM. Due to the 'on' time of a typical experiment being $1-5\%$ duty cycle at 10kHz, and the bandwidth of the analog PID loop only being 100kHz, it is not possible for the current system to compensate fluctuations within a singular quasi-pulse, but rather it minimises fluctuations over an extended period that would be comparable to that of time integrated measurements.

[6]Note that the intensity profile of the first diffracted order is proportional to the voltage from the function generator whilst the the zeroth order is inversely proportional to the driving voltage.

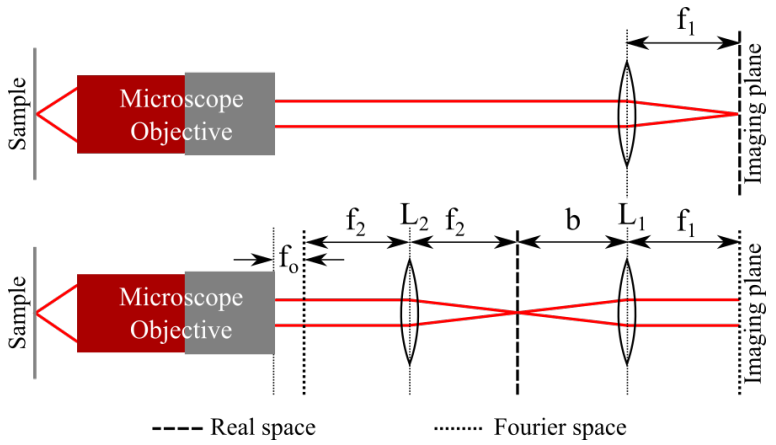

FIGURE 2.12: Top: Ray diagram demonstrating the imaging of real space using an infinity corrected objective and lens (L_1) with focal length f_1. Bottom: Depiction of Fourier space imaging with the addition of a second lens (L_2) with focal length f_2.

2.5 Types of measurements

Due to conservation laws, optical selection rules and the dissipative nature of the system, a polariton condensate can be fully characterised via well established optical techniques without needing to perturb the condensate. This section describes the various measurement techniques used during my PhD candidature.

2.5.1 Real and Fourier space imaging

To image real space (Figure 2.13(a)) an infinity corrected microscope objective lens focuses the samples' surface at infinity and a 'tube' lens L_1 refocuses the **real space** onto a detector (normally a CCD/CMOS sensor); see top schematic of Figure 2.12. Fourier space (K-space) (Figure 2.13(b)) can be imaged with the addition of a second lens L_2 it's focal length from the rear focal plane of the microscope objective lens, bottom schematic in Figure 2.12. In the bottom schematic of Figure 2.12 the length 'b' is drawn to be the same as f_1 which makes each plane (real space or Fourier space) Fourier related to the one before and after and thus the system is conjugated. However, 'b' can take other values, if $b \neq f_1$ then it is more intuitive to picture the system as L_2 imaging the Fourier plane at infinity and L_1 refocusing it at the final imaging plane.

2.5.2 Spectroscopy and tomography

Both of the above imaging techniques can be combined, with the use of a spectrometer or a tuneable Fabry-Pérot cavity, to attain spectral resolution. For the work discussed, a high resolution spectrometer (75cm) is used with 1200 groves/mm and 1800 groves/mm gratings. The polariton disperion (energy resolved k-space) is directly accessible through

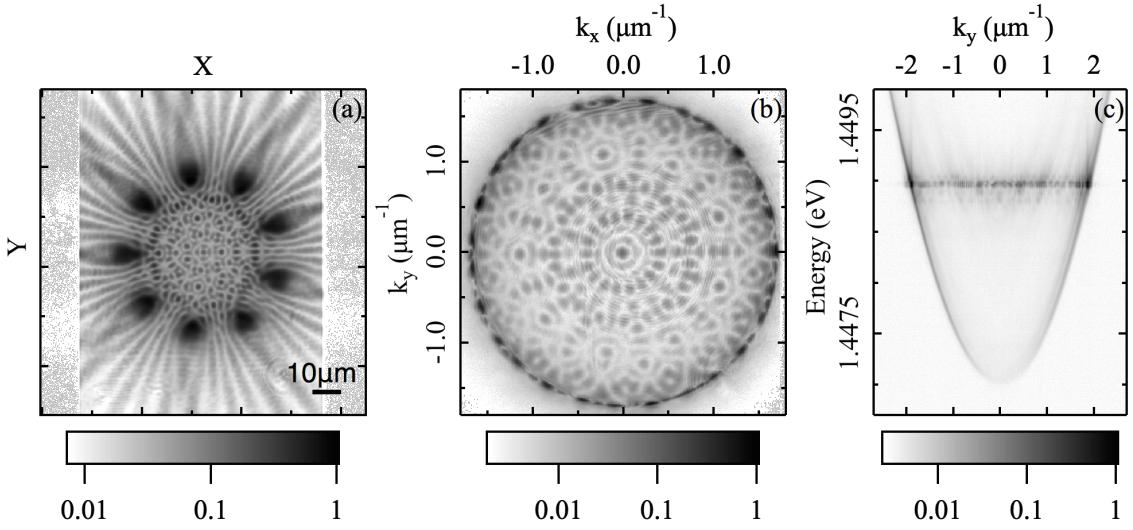

FIGURE 2.13: (a) Experimental real space image of a nonagon of coupled polariton condensates. (b) Fourier space corresponding to the real space in (a). (c) Energy resolved Fourier space (dispersion) corresponding to a narrow vetical strip of (b) centered around $k_x = 0$. All three images are in a logarithmic colour scale with the corresponding colour bars beneath each image.

angle resolved spectroscopy; where the Fourier space (k-space) is imaged onto the entrance slit of the spectrometer, see Figure 2.13(c).

Through tomographic techniques it is possible to reconstruct spectrally resolved two dimensional real space and Fourier space images. This is achieved by scanning the corresponding imaging plane (real or Fourier space) perpendicularly across the entrance slit of the spectrometer and building a stack of the spectrally resolved images from each step in the scan. Then by combining the rows of constant energy across the stack, the real or Fourier space image at that energy is reconstructed. The downside of such measurements is the real space or Fourier space resolution on one axis of the resulting images is determined by the slit width and step size used when rastering the real or Fourier plane across the slit. Therefore there is a trade off between spatial/Fourier resolution and the amount of data taken/acquisition time.

If one were to use a tunable Fabry-Pérot cavity, the spectrally resolved two dimensional real or Fourier space images can be taken directly, with the resolution determined by the optics and detector only. The specific energy imaged each time is determined by the separation of the two mirrors, which is controlled via a linear piezo actuator on one mirror.

2.5.3 Polarisation resolved measurements

Using various polarising optics (waveplates, polarising beam splitters etc) it is possible to decompose the PL into the various cross-polarisation contributions, the intensities of

which can be recorded as a function of time or they can be spatially imaged. It is using these techniques that the spin state of the polariton condensate can be determined as discussed in Section 1.1.4.

Figure 2.14 depicts the system used to temporally resolve the cross-circular polarisation contributions of the PL. The quarter-waveplate ($\lambda/4$) is set at an angle of 45°, converting the cross-circular polarisations into horizontal or vertical polarisation. The polarising beam splitter (PBS) then separates the two linear polarisations, the intensities of which are temporally measured on two balanced photodiodes. By removing the $\lambda/4$ the same setup will then resolve the contributions of the vertical and horizontal polarisations and the addition of a $\lambda/2$ waveplate at 22.5°, in place of the $\lambda/4$, yields the diagonal/anti-diagonal contributions. Through these three setups the psuedospin (equally Stokes vector) of a polariton condensate can be determined.

Rather than temporally resolving the total contribution of each polarisation it is possible to spatially resolve the polarisation components using a very similar system. To allow both cross-polarisations to be imaged on a singular CCD/CMOS detector, the PBS can be replaced with a polariser that separates the two polarisations by significantly less than 90°.

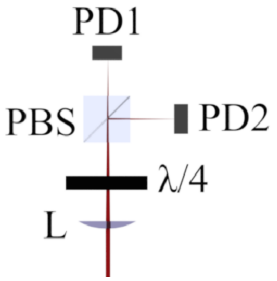

FIGURE 2.14: Cross circular polarisation analyser. L - planoconvex lens focusing the light onto the two detectors, $\lambda/4$ - quarter waveplate, PBS - polarising beam splitter, PD1(2) photodiodes.

2.5.4 First order coherence - Michelson interferometer

Michelson interferometers in the mirror retro-reflector geometry (see Figure 2.15) can be used in the determination of the relative phase between condensates and the calculation of the normalised first order correlation function:

$$g^{(1)}(\tau, |r' - r|) = \frac{\langle E^*(r,t)E(r',t+\tau)\rangle}{\sqrt{\langle |E(r,t)|^2\rangle\langle |E(r',t+\tau)|^2\rangle}} \tag{2.4}$$

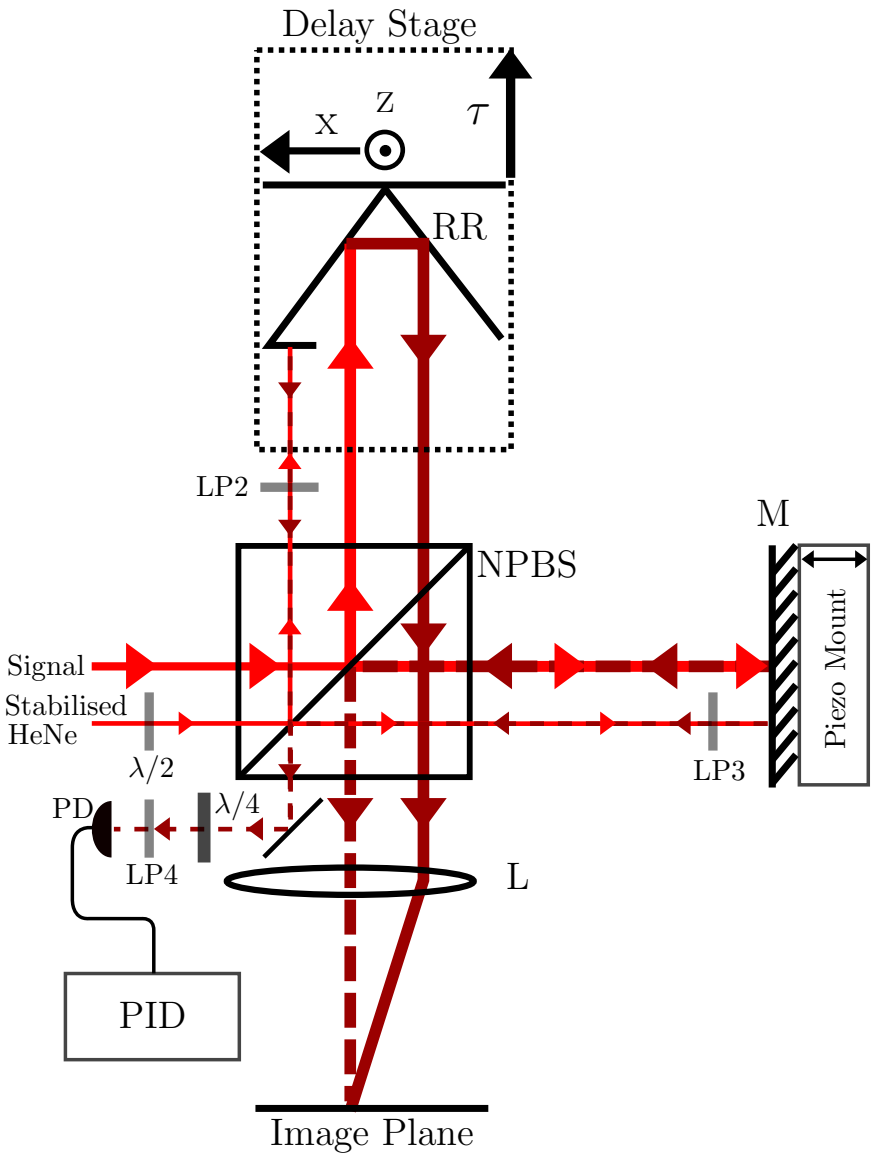

FIGURE 2.15: Actively stabilised Micheleson interferometer. RR - retro-reflector on a 15cm delay stage, M - mirror on a linear piezo actuator, NPBS - non polarising beam splitter, L - plano convex lens, PD - photodiode, LP1(2,3) - linear polarisers, $\lambda/4$ - quarter waveplate and PID - proportional integral differential loop.

where $E(r,t)$ is the electric field at position r and time t and $E^*(r,t)$ is the complex conjugate thereof. τ corresponds to the time delay between the two arms of the interferometer and $|r'-r|$ the spatial separation of the regions interfered. $g^{(1)}(\tau,|r'-r|)$ gives a direct measurement of the degree of phase coherence at τ and $|r'-r|$.

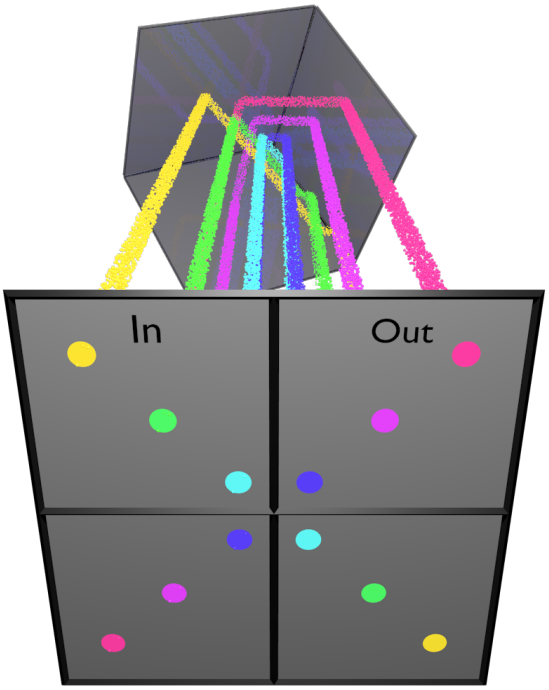

FIGURE 2.16: Demonstration of beam inversion via a standard hollow retro-reflector

A modified Michelson interferometer replacing the mirror in one arm with a retro-reflector is used because retro-reflectors flip an image in two orthogonal directions resulting in the outgoing beam being the completely inverted image of the incident beam. Additionally if the retro-reflector is positioned with the incident beam displaced by $\vec{r}_{disp}$, from the central inflection point, then the outgoing beam is displaced by $-2\vec{r}_{disp}$ from the incident beam, see Figure 2.16. Finally the outgoing beam always propagates anti-parallel to the incident beam. These features of retro-reflectors enable cross-correlations over an entire image, and thus demonstration of coherence across the condensate, to be completed in a single shot. Additionally, controlling the displacement of the outgoing beam with respect to the beam incident on the retro-reflector (via XY translation stages) gives direct control over the fringe density and angle in the resulting interferogram. This is because the retro-reflector displacement controls the relative angle of the beams from both arms when they are recombined at the imaging plane, Figure 2.15. Which is equivalent to an additional in-plane wavevector between the two. The retro-reflector is additionally mounted on a 15cm long delay stage, enabling the temporal phase decay, and so coherence time (τ_{coh}), to be accessed.

2.5.4.1 First order correlations

Consider a fully coherent source, the interferogram resulting from a retro-reflector - mirror Michelson interferometer can be written as:

$$I_{int}(\vec{r},\tau) = |E_M(\vec{r}) + E_R(\vec{r},\tau)|^2 \tag{2.5}$$

where $E_M(\vec{r}) = E_{0_M}(\vec{r})e^{i\theta_M(\vec{r})}$ and $E_R(\vec{r},\tau) = E_{0_R}(\vec{r})e^{i(\theta_R(\vec{r})+\delta(\tau))}$ are the electric fields of the mirror (M) and retro-reflector (R) arms when recombined at the imaging plane. $E_{0_{M(R)}}$ and $\theta_{M(R)}$ are the amplitude and phase of the mirror (retro-reflector) beam respectively and $\delta(\tau)$ is a phase difference due to a time delay τ from differences in arm lengths. Therefore

$$I_{int}(\vec{r}) = I_M(\vec{r}) + I_R(\vec{r}) + 2\sqrt{I_M(\vec{r})I_R(\vec{r})}cos(\Theta(\vec{r}) + \delta(\tau)) \tag{2.6}$$

where $I_{M(R)} = |E_{0_{M(R)}}|^2$ is the intensity map of the mirror (retro-reflector) arm and $\Theta(\vec{r}) = (\theta_R(\vec{r}) - \theta_M(\vec{r}))$ [7]. There is the expected sinusoidal behaviour of the intensity as a function of $\vec{r}$. For equally intense (and centrosymmetric, when using a retro-reflector) fields this sinusoidal term results in complete extinction of intensity at the minima of the cosine term as $2\sqrt{I_M(\vec{r})I_R(\vec{r})} = I_M(\vec{r}) + I_R(\vec{r})$. Note if there is a displacement of the retro-reflector beam there would be an additional term within the cosine term that can break the radial symmetry resulting in linear fringes when this additional term is dominant; this term has been neglected here to simplify the discussion.

To expand the description to include any level of coherence from completely coherent to completely incoherent fields, Equation 2.6 gains a multiplicative scalar factor to the cosine term:

$$I_{int}(\vec{r}) = I_M(\vec{r}) + I_R(\vec{r}) + 2\sqrt{I_M(\vec{r})I_R(\vec{r})}cos(\Theta(\vec{r}) + \delta(\tau)) \cdot g^{(1)}(\vec{r},\tau) \tag{2.7}$$

where $g^{(1)}$ is the first order correlation function, with $g^{(1)} = 1$ for full coherence, $1 < g^{(1)} < 0$ for partial coherence and $g^{(1)} = 0$ for full incoherence.

Experimentally, there are two methods to determine the level of coherence, one is data and computationally heavy and the other is a faster determination. The computationally lighter method is to take the interferogram and two reference images (as well as the background[8]), one of each interferometer arm, from which $g^{(1)}$ is determined via

$$g^{(1)}(\vec{r},\tau) \cdot cos(\Theta(\vec{r}) + \delta(\tau)) = \frac{I_{int}(\vec{r}) - I_M(\vec{r}) - I_R(\vec{r})}{2\sqrt{I_M(\vec{r})I_R(\vec{r})}}. \tag{2.8}$$

[7] Note that the retro-reflector beam is the mirror beam inverted and so $I_R(\vec{r}) = I_M(-\vec{r})$ and the same holds for E_{0_R} and θ_R.

[8] As determination of the degree of coherence explicitly looks at the level of extinction between bright fringes it is critical correct background removal on all images is carried out.

Taking a line profile perpendicular to the fringes yields a sinusoidal function, the amplitude of which is the degree of coherence $g^{(1)}$. Equally this can be done without the reference images of each interferometer arm via the fringe visibility

$$Vis = \frac{I_{max} - I_{min}}{I_{max} + I_{min}} \tag{2.9}$$

where I_{max} and I_{min} correspond to the envelope functions of the maxima and minima of intensity respectively for a given line profile perpendicular to the fringes. The benefit of fringe visibility is that it can be automated and used as a live check of the degree of coherence during an experiment as all it requires is the interferogram and a singular background image that can be taken once at the beginning.

The more computationally expensive technique involves scanning the relative arm lengths of the interferometer in very small step sizes, with relative phase of the arms sweeping across $\sim 6\pi$. This delay is applied via the linear piezo actuator the mirror is mounted on; see Figure 2.15. Through the interferometer stabilisation setup, described in Section 2.5.4.3, one can scan the position of the mirror in very small step sizes by rotating the linear polariser infront of the photodiode. Taking interferograms for each step of this $\sim 6\pi$ scan of relative phase, normalising each as per Equation 2.8 and stacking them, one can then determine $g^{(1)}$ for every pixel in the interferogram by determining the sinusoidal modulation amplitude of the recorded intensity as a function of the piezo actuator position. This is possible because each step of the piezo actuator relates to a different optical path length difference between the two interferometer arms, which changes the $\delta(\tau)$ term in Equation 2.8 giving rise to the sinusoidal oscillation. Due to the number of images that have to be taken in succession for this technique, the active interferometer stabilisation, described in Section 2.5.4.3, is critical.

2.5.4.2 Coherence length and time

Whilst determining the level of coherence is of interest, it is generally how the coherence changes as a function of time and/or separation distance that gives more detailed information about spatial and temporal characteristics of the system. Coherence length is impractical to measure in polariton systems as generally the coherence length far exceeds the spatial extent of a singular condensate. Whilst one could use multiple coherently coupled condensates separated by a large distance, as will be shown in Chapter 5, the existence of multiple condensates changes the coherence of the system.

Therefore, generally the coherence time of the condensates is measured using a controllable delay stage on the retro-reflector arm allowing the interference of light from time t (from the mirror arm) with light from time $t + \tau$ (from the retro-reflector arm), where τ can be positive or negative. Calculating $g^{(1)}(\tau)$ at each value of τ, a characteristic

decay as $|\tau|$ increases from zero can be fitted to determine the coherence time. The function that should be fitted to this decay is dependent on the dominant source of noise in the signal. For a signal that demonstrates a Lorentzian lineshape - corresponding to homogenous broadening - one would fit $g^{(1)}(\tau)$ with an exponential function as the Fourier transform of a Lorentzian is an exponential. Conversely if one has a dominantly Gaussian lineshape then one should fit $g^{(1)}(\tau)$ with a Gaussian. Of course in experiment the lineshape is likely to contain both Lorentzian and Gaussian components (Voigt).

2.5.4.3 Active interferometer stabilisation

Interferometric measurements are sensitive to noise/fluctuations on the scale of the wavelength of the light. Despite best efforts, it is unrealistic to be able to isolate the interferometer from such small fluctuations in a typical laboratory environment. Therefore, it is necessary to implement an active stabilisation that can lock the interferometer arms to have a given phase difference. The technique implemented in the work here is not new, sharing similarities with that designed by Wehner M. et al. in 1997 [75] and a closer relationship to that implemented by Lagoudakis K. described in [76].

As depicted in Figure 2.15, the stabilisation setup uses a linearly polarised, frequency stabilised HeNe laser. A $\lambda/2$ waveplate is used to set the polarisation to diagonal/antidiagonal and the two interferometer arms contain linear polarisers orientated vertically in one arm and horizontally in the other to create two cross-linearly polarised beams of equal intensity. On the mirror arm of the interferometer, the same mirror can be used for the stabilisation beam, whilst for the retro-reflector arm a mirror firmly mounted to the retro-reflector is used. Following recombination at the non-polarisaing beam splitter (NPBS), the two beams go through a $\lambda/4$ waveplate orientated at 45° to convert the two cross-linear polarisations into cross-circularly polarised beams. The summation of two cross-circularly polarised beams with a phase delay (here related to the relative arm lengths) results in a linearly polarised beam. The orientation of the linear polarisation is related to half the phase delay between the cross-circularly polarised beams ($2\delta_{stab}$), an effect known as optical rotation. This can be seen by writing the two cross-circularly polarised beams in terms of their components in two orthogonal linear polarisation components (Jones vector):

$$E_{\sigma_+} = \begin{pmatrix} E_x \\ E_y e^{i(\pi/2)} \end{pmatrix} e^{-i\delta_{stab}},\ E_{\sigma_-} = \begin{pmatrix} E_x \\ E_y e^{-i(\pi/2)} \end{pmatrix} e^{i\delta_{stab}} \tag{2.10}$$

noting that $E_x = E_y$ as these are circularly polarised states and $e^{\pm i(\pi/2)} = \pm i$, the sum of these is:

$$E_{sum} = \begin{pmatrix} E(e^{-i\delta_{stab}} + e^{i\delta_{stab}}) \\ Ei \cdot (e^{-i\delta_{stab}} - e^{i\delta_{stab}}) \end{pmatrix} = \begin{pmatrix} 2E\cos(\delta_{stab}) \\ 2E\sin(\delta_{stab}) \end{pmatrix} \tag{2.11}$$

i.e. a field where the components in the orthogonal directions are in phase (linearly polarised) and the relative amplitude of each is a function of the phase delay between the cross-circularly polarised beams (the orientation of polarisation depends on δ_{stab}). Therefore the intensity of light focused on the photodiode is directly related to the relative path lengths of the interferometer arms as well as the angle of the linear polariser after the $\lambda/4$. Using the intensity dependent voltage from the photodiode as the signal to a proportional-integral-differential (PID) loop, a corrective signal can be sent to the linear piezo actuator on the mirror arm to compensate for any fluctuations; thus stabilising the interferometer. This system stabilises/locks the interferometer to a desired phase delay between the arms. Furthermore, by mounting the final linear polariser before the photodiode on an automated rotation stage one can scan the relative phase delay between the interferometer arms across a number of wavelengths with great accuracy. The limiting factor on the number of wavelengths this technique can scan is simply the extent of travel on the piezo actuator.

2.5.4.4 Single shot interferometry

The active stabilisation of the interferometer and the global intensity stabilisation both work together to help reduce fluctuations which would otherwise cause the measured first order coherence to be artificially lowered. The next step to improving interferometric measurements was to implement triggered single shot interferometry. This involves triggering the camera to acquire an image during a singular quasi-pulse, using an exposure time shorter than the quasi-pulse duration. This significantly improves interferometric measurements as using exposure times that span multiple quasi-pulses result in images that are an average of many condensate realisations, which can artificially reduce the resulting $g^{(1)}$ measured.

2.5.5 Generalised experimental setup

By careful optimisation of the efficiency of the optical setup, it becomes possible to simultaneously measure multiple parameter spaces of the PL. For example, Figure 2.17 depicts the schematic of a simplified experimental setup that allows the measurement of real space (camera 1), Fourier space (camera 2) and spectrally resolved real or Fourier space (camera 3) simultaneously. By moving flipper mirrors into the beams path camera 3, in Figure 2.17, can additionally be changed to carry out interferometric measurements (interferometer not shown in the schematic).

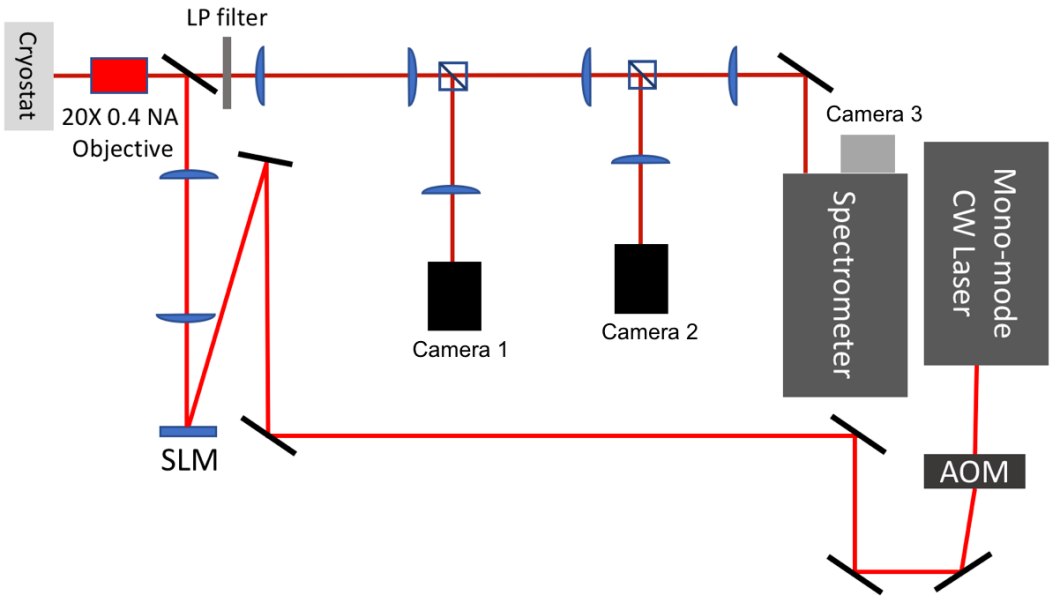

FIGURE 2.17: Simplified schematic of an experimental setup enabling the simultaneous measurement of real space (camera 1), Fourier space (camera 2) and spectra (camera 3). AOM - acousto optic modulator, SLM - spatial light modulator, NA - numerical aperture and LP filter - long pass filter.

In the following chapters, the experimental techniques outline above are implemented to investigate:

1. All-optical spin bistability in non-resonantly driven polariton condensates.
2. First order coherence properties of polariton condensates.
3. Time delayed coupling of spatially separated freely expanding polariton condensates.
4. All-optical band structure engineering using polariton condensates.

Chapter 3

Optical Bistability

3.1 Introduction

The phenomenon of bistability refers to a system supporting two stable solutions over a range of values for a given driving parameter [77,78]; with the solution reached depending on what the driving parameter was immediately before i.e. if the driving parameter is being swept forward or back. This behaviour necessitates that the system has a memory of the state it was in previously, meaning bistable effects can be used in logic/memory elements. It is usually demonstrated by means of a hysteresis loop in the plot of the measured observable vs driving parameter where the area of the hysteresis loop corresponds to the strength of the bistability. Optical bistability specifically concerns itself with bistable effects within optical systems and thus is of interest for optical transistors and optical memory, both of which are highly desirable.

Optical bistability has previously been demonstrated in systems such as cold atoms [79], lasers [80], self-electro-optic effect devices [81] and Fabry-Pérot cavities containing nonlinear materials [82,83]. In polaritonic systems bistability was limited to being observed under quasi-resonant/resonant optical excitation [84–89] or with electrical biasing [90,91] and under non-resonant electrical injection with a perturbing magnetic field [92]. For resonant excitation bistable effects have previously been described via a Kerr-like nonlinearity resulting from polariton-polariton interactions [84] and by analogy to optical parametric oscillators [85]. Bistability was observed in the luminescence intensity under electrical injection in the presence of an external magnetic field and the effect was attributed to an electrostatic screening of the injected charge carriers creating a positive feedback for the backward sweep of the driving current [92].

Due to the one-to-one correspondence between the circular polarisation of light and the polariton spin, as described in the Section 1.1.4, bistability and even multi-stability in

the spinor of a polariton condensate was demonstrated under quasi-resonant optical excitation of a cylindrical mesa by rotating the polarisation of the optical pump [86]. Spin-bistability was also shown under non-resonant optical excitation of a mesa while keeping the optical excitation constant by sweeping a biasing electrical field that introduced an energy splitting between two linear polarisation modes [90]. Under non-resonant excitation and in the abscence of external perturbing fields, the preferable operation of all-optical memory elements, both polariton bistability and spin-bistability remained elusive before the work presented in this chapter, despite theoretical predictions [93].

3.2 Path to realising all optical bistability under non-resonant excitation

The fundamental difference between resonant and non-resonant optical excitation is the presence, in the latter case, of a hot-exciton reservoir, and the concomitant exciton-polariton interactions. The observation of polariton bistability (from herein explicit distinction between bistability and spin-bistability may not always be made) is critically dependent on the noise/population fluctuations being too small to bridge the two stable solutions of the system as otherwise this would collapse the desired hysteresis loop.

Therefore to realise bistability under non-resonant excitation it is paramount to isolate the polariton condensate from the exciton reservoir as much as possible. Exciton-polariton pair scattering events are a significant source of decoherence [2, 63, 67], population fluctuations and are also a strong source of spin mixing [68] all of which are detrimental to any bistable regime in intensity or spin.

To separate the polariton condensate from the exciton reservoir an optical trap pumping regime is employed in the form of using an annular excitation beam which produces a trapping potential landscape with a minimum in the centre [42,63,64], see Figure 3.1. A spatial light modulator is used to produce the desired pumping geometry by imprinting a 2D binary axicon phase profile on the excitation beam, as described in Section 2.3. It is critical to note that the trapped state formed maximises net gain which corresponds to having the largest overlap with the reservoir, generally this is the highest order mode supported by the trapping potential. Therefore, the size of the annulus has a significant impact on the existence and/or strength of the bistability. One expects the largest hysteresis loop when the trap is the maximum size that supports only the ground state as this will relate to the system with minimum condensate-reservoir overlap.

The sample used for this work has an AlGaAs microcavity with GaAs QWs produced by the group of P. G. Savvidis [58] as described in Section 2.1. It is cooled to $\sim 6K$ using a continuous flow cold finger cryostat. The sample is excited with a linearly polarised continuous wave (CW), monomode laser, tuned to the first minimum in reflectivity, energetically above the stopband, at 754nm. The intensity of the pump laser is modulated

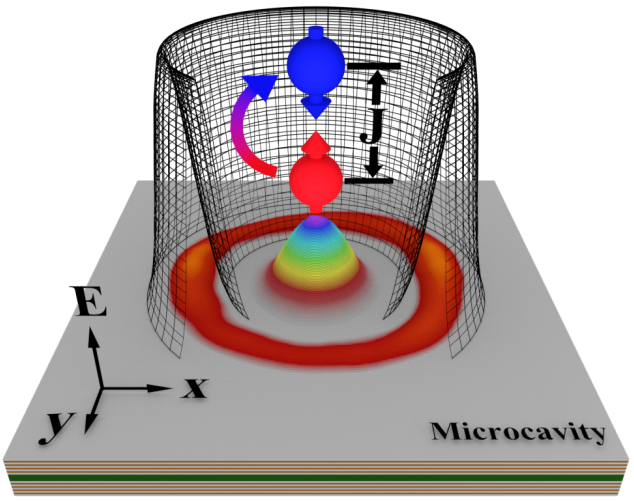

FIGURE 3.1: Schematic of the optical excitation scheme from [1]. An intensity map of the pump beam is shown by the red ring on the microcavity. The black mesh represents the confining potential barrier produced by the exciton reservoir, a section is cut out to show the rainbow-coloured centrally trapped condensate that is close to a Gaussian mode. The red and blue spheres show the spin-up and spin-down constituent states of the condensate respectively with the arrow representing the coupling between the two.

into triangular pulses with symmetric rise and fall using an AOM driven by a triangular voltage train from a function generator. Finally the pump beam is focused onto the sample surface using a 0.4 numerical aperture (NA) microscope objective lens.

The spinor of the polariton condensate is probed directly by the degree of circular polarisation (DCP) of the PL. This can be represented by the S_Z component of the Stokes polarisation vector, defined as

$$S_Z = \frac{I_{\sigma_+} - I_{\sigma_-}}{I_{\sigma_+} + I_{\sigma_-}} \tag{3.1}$$

where $I_{\sigma_+}$and I_{σ_-} correspond to the measured intensity of the right-circular and left-circular polarised light. To resolve the intensities of the cross circular polarisations of the PL a quarter waveplate ($\lambda/4$) is used to convert the cross circular polarisations into horizontal and vertical polarisations which are subsequently split via a polarising beam splitter (PBS) and recorded simultaneously using two photodiodes balanced to account for any imbalance introduced by the optics such as the PBS. Simultaneously to recording the cross circularly polarised intensities there is a photodiode recording the excitation beam which allows one to plot the DCP vs excitation power[1]. A schematic of the experimental setup is shown in Figure 3.2.

[1]To account for any non-linear response of the AOM to voltage it is critical to measure the pump intensity simultaneously to $I_{\sigma_+}$and I_{σ_-}.

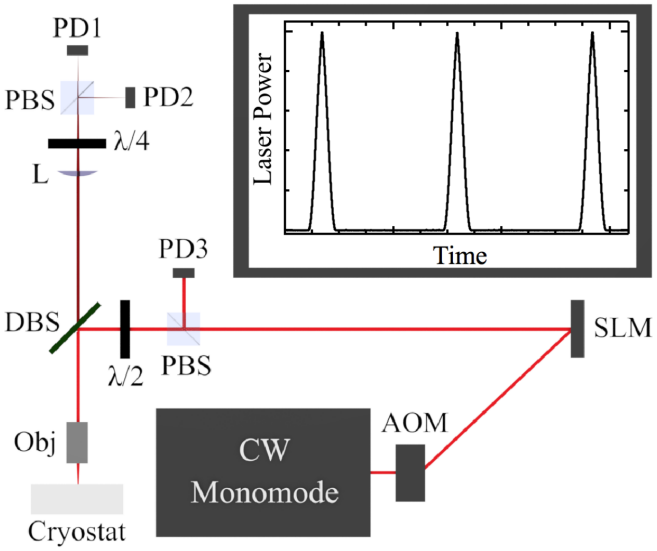

FIGURE 3.2: Schematic of the experimental setup from [1] where AOM - acousto optical modulator, SLM - spatial light modulator, PBS - polarising beam splitter, DBS - dichroic beam splitter, Obj - 0.4 numerical aperture microscope objective lens, L - plano-convex lens, $\lambda/2$ and $\lambda/4$ - half and quarter waveplates respectively and PD (1,2,3) - photodiodes measuring the spin components of the photoluminescence and the corresponding laser intensity.

3.3 Results and discussion

Figure 3.3 shows a typical experimental hysteresis loop in the DCP of the PL vs the optical excitation power, as it is swept from below threshold to several times threshold and back in the trapped spinor polariton system. The spin reversal on the forward sweep of excitation power, shown with the red dashed line in Fig. 3.3, was previously shown with time integrated measurements [42] where it was attributed to a transition from a synchronised phase evolution of the two spinor components to a desynchronised phase evolution regime. For decreasing excitation power, shown with the solid blue line in Fig. 3.3, there is backwards spin reversal but at a significantly lower pump power compared to the power of the spin reversal in the forward direction, thus opening a hysteresis loop.

The effect can qualitatively be reproduced, see Figure 3.4, using the same complex spin-dependent Ginzburg-Landau model coupled to the reservoir rate equation (cGLEs) [2]

$$\begin{aligned} i\hbar\frac{\partial\psi_{\pm}(t)}{\partial t} &= \{\alpha_0|\psi_{\pm}|^2+\alpha_1|\psi_{\mp}|^2+\hbar g_R n_{\pm}+ \\ &+ \frac{i\hbar}{2}\left(R_R n_{\pm}-\gamma_C\right)\}\psi_{\pm}+\Delta\psi_{\mp}, \end{aligned} \tag{3.2}$$

[2]The numerical simulations were carried out by K. Kalinin and N. G. Berloff

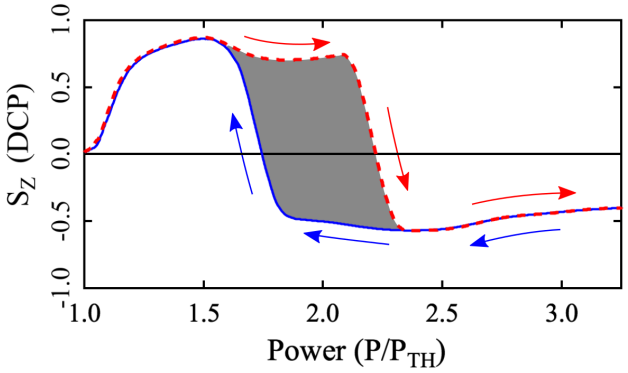

FIGURE 3.3: Measured third Stokes component, S_Z, representing the degree of circular polarization (DCP) vs pump power displaying the characteristic hysteresis loop of bistability for an annulus of $\sim 16.1\mu$m diameter and 1.67ms sweep time at a detuning of -7.6meV. Data published in [1].

$$\frac{\partial n_{\pm}(t)}{\partial t} = -\left(\gamma_R + R_R|\psi_{\pm}|^2\right) n_{\pm}(t) + P_{\pm}(t), \tag{3.3}$$

as in [42], where $\alpha_0 > 0$ is the strength of the repulsive interaction between polaritons with the same spin, $\alpha_1 < 0$ characterizes a weak attractive interaction between polaritons of opposite spin and Δ is the Josephson coupling term. γ_R and γ_C are the decay rates of the reservoir and condensate respectively, R_R is the scattering rate from the reservoir into the polariton condensate, $P_{\pm}$ is the relative pumping rate of the reservoirs for each spin state and g_R is the blueshift originating from interparticle interactions with the reservoirs.

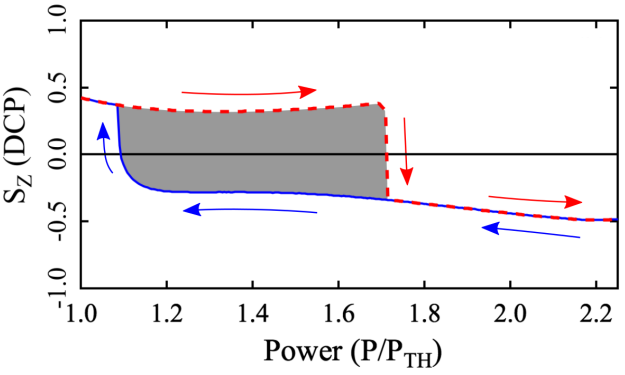

FIGURE 3.4: Numerically simulated S_Z vs excitation power qualitatively reproducing the observed hysteresis. Data published in [1].

3.3.1 Analogy to a driven damped pendulum

To develop an intuitive picture for the nature of polariton spin bistability it is best to draw analogues with the driven damped pendulum (DDP). First it is necessary to non-dimensionalize the cGLEs (Eqs.3.2 - 3.3) using $\psi_{\pm} \rightarrow \sqrt{\hbar\gamma_C/\alpha_0}\psi_{\pm}, n_{\pm} \rightarrow$

$2m\gamma_C/\hbar n_\pm, t \to t/\gamma_C$ and introducing $U_\alpha = 1 - \alpha_1/\alpha_0$, $g = 2mg_R/\hbar, R = 2mR_R/\hbar, J = \Delta/\hbar\gamma_C, \gamma = \gamma_R/\gamma_C, b = \hbar R_R/\alpha_0, p_\pm = \hbar/2m\gamma_C^2 P_\pm, \epsilon = \eta - 1, \rho = (|\psi_+|^2 + |\psi_-|^2)/2$. One can then reduce Eqs.3.2 - 3.3 to the form of a DDP;

$$\ddot{\Theta} + \beta(p)\dot{\Theta} = -I_{\text{bias}}(p) - I_{\text{cr}}(p)\sin\Theta \tag{3.4}$$

where Θ is equal to the phase difference between the two spin components in the polariton system and the angular displacement for the DDP, β is a damping coefficient (positive above threshold) that increases with pump power to a saturation value of $1/2$ in the polariton system. I_{bias} is equivalent to the driving torque and I_{cr} is the torque required to overcome any resistive torques (gravity when $\Theta < \pi$ and damping for all Θ). The functional form of the parameters in the non-dimensionalised basis are $\beta(p) = 1/2 - \gamma/2Rp(1+\epsilon)$, $I_{\text{bias}}(p) = U_\alpha\rho_{\text{st}}\epsilon/2(2+\epsilon)$, $I_{\text{cr}}(p) = J\rho_{\text{st}}(U_\alpha - gb/(1+\epsilon)R^2p)$ and $\rho_{\text{st}} = [(\epsilon+2)Rp - 2\gamma]/2b$ which is the stationary solution $d\rho/dt = 0$.

DDPs exhibit two forms of solution [94], fixed point and limit cycle. The former relates to the regime in which the driving torque is unable to overcome the resistive torques, i.e. if the ratio $I = |I_{\text{bias}}|/|I_{\text{cr}}| \leq 1$. In this regime under a constant driving torque the pendulum will reach a stable position with fixed angular displacement ($\dot{\Theta} = 0$) from the vertically down position. Conversely under constant driving torque if the maximum resistive torques are lower than the driving torque (i.e. $I > 1$) then the pendulum will continually overturn ($\dot{\Theta} \neq 0$). In the spinor-polariton system, fixed point solutions correspond to a state where the phase of the two spinor components evolve synchronously (constant phase difference) which correlates to the upper branch of the hysteresis loop. Limit cycle solutions correspond to the regime where the phases of the two components evolve desynchronously (non-constant phase difference) relating to the lower branch of the hysteresis loop. Herein the two regimes will be referred to as synchronised (S) and desynchronised (D) respectively.

In the following the formation of bistability in a DDP as the driving torque is swept forwards and backwards is described and comparisons are made to the trapped spinor polariton condensate, this is represented schematically in Figure 3.5. On the forward sweep (increasing) of the driving torque (τ_d) the DDP starts in a synchronised regime, with Θ slowly increasing only as τ_d is increased but it is always able to reach a stationary position (Figure 3.5 panel 1-2). There is a transition point when τ_d reaches a critical value (τ_{cr}) that has a corresponding stationary position of $\Theta = \pi/2$, which equates to the position of maximal resistive gravitational torque (Figure 3.5 panel 2). Should $\tau_d > \tau_{cr}$ then the system transitions into a desynchronised regime where no stationary position exists, this corresponds to the switch in the sign of S_Z on the forward branch of the spinor polariton hysteresis loop (Figure 3.5 panel 2-3). In the reverse direction (backward sweep) starting with the DDP overturning (in a desynchronised regime, Figure 3.5 panel 4) and reducing τ_d to be equal to τ_{cr} the DDP will remain in the desynchronised regime

due to inertia in the form of angular momentum. The DDP will only transition back to a synchronised regime when the damping has had sufficient time to dissipate enough energy that τ_d and the angular momentum are unable to overcome the resistive torques; this occurs for $\tau_d < \tau_{cr}$ creating a hysteresis loop (Figure 3.5 panel 6). How much lower the driving torque can be for the reverse transition is determined by sweep rate and level of damping.

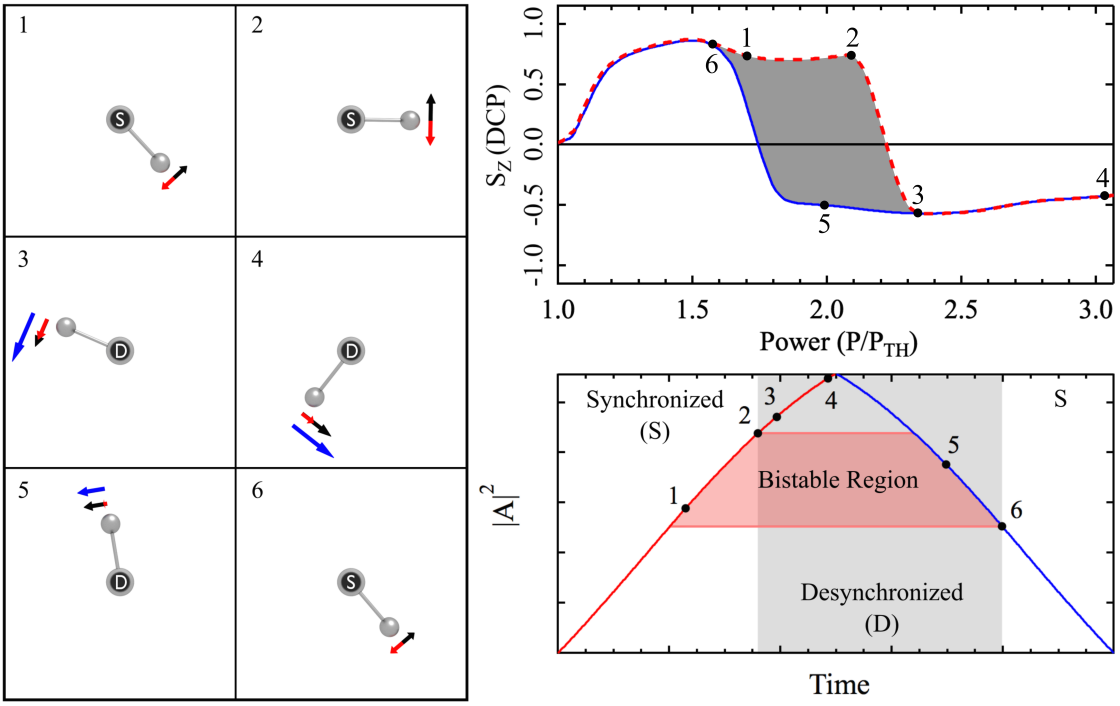

FIGURE 3.5: Panels 1-6, schematics of the state of a driven damped pendulum with arrows representing the different torques [1]; the driving torque (black), the gravitational torque (red) and the total torque (blue). The positions corresponding to panels 1-6 are highlighted on the plots of S_Z vs pump power and $|A|^2$ vs time, where $|A|^2$ is the pump intensity in the case of the spinor polariton condensate and the magnitude of the driving torque in the case of the driven damped pendulum.

3.3.2 Effect of exciton-polariton interactions

As alluded to in Section 3.2 polariton-exciton (pol-ex) interactions are highly deleterious to bistable behaviour due to the various (total and spin dependent) population fluctuations and noise they induce. At low temperatures, the exciton diffusion length is small making the reservoir co-localised with the excitation laser geometry. Therefore, the effect of pol-ex interactions can be investigated by changing the trap size and thus changing the overlap, Ω, of the condensate and the hot-exciton reservoir. Figure 3.6 shows the hysteresis area as a function of annular trap diameter; the solid black diamonds are for a detuning of -7.6 meV and the solid black circle is for a detuning of -11.2 meV. The red dotted line in Figure 3.6 shows an estimated functional form for Ω assuming a Gaussian-shaped condensate and an annular trap with Gaussian cross section,

the width of the condensate and annular profile are approximated from the measured PL under different annular pump diameters. For trap diameters in the range 11.8μm to 17.9μm the hysteresis area increases monotonically as Ω decreases/the trap diameter is increased. For trap diameters exceeding 17.9μm the trap can support the coexistence of the Gaussian-shaped ground trapped state and the first higher-order Hermite-Gauss-shaped ψ_{01} mode [64] which increases Ω sufficiently to collapse the hysteresis loop. The impact of pol-ex interactions is further exemplified by the solid black circle in Figure 3.6 depicting the hysteresis area for a trap of 13.1μm diameter at a more negative detuning. The notable increase is hysteresis area results from the reduced exciton Hopfield coefficient and thus weaker interparticle interactions.

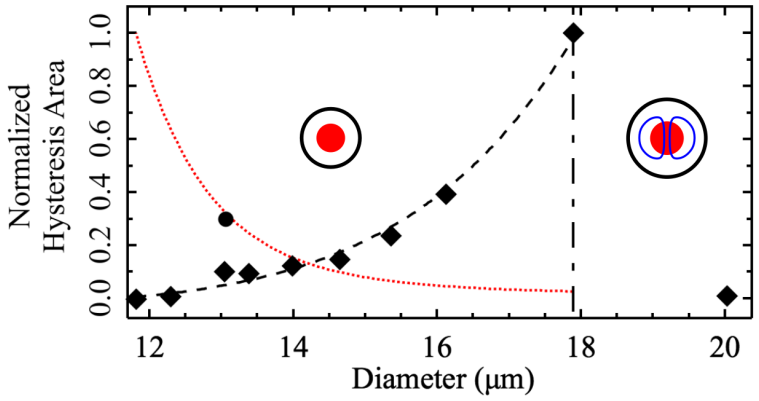

FIGURE 3.6: The dependence of the hysteresis area (symbols) on the diameter of the annular pump at $\sim 6K$ with a 1ms sweep time. The dotted red line shows the estimated overlap between the condensate and exciton reservoir, Ω, vs the annular pump diameter. The vertical dash-dotted line separates the regimes wherein only the ground state, ψ_{00}, or both ψ_{00} and first excited state, ψ_{01}, coexists. Data published in [1].

Furthermore, as the trap diameter is reduced from 17.9μm the reduction in hysteresis area is not only the result of a narrowing of the hysteresis width, the height also decreases; i.e. the strength of the spin flip is reduced for increasing overlap; see Figure 3.7. This further demonstrates that the observed behaviours are most likely a result of the overlap of the condensate with the reservoir as the reduction in spin-flip indicates that there is increased spin-mixing which pol-ex interactions are a strong source of.

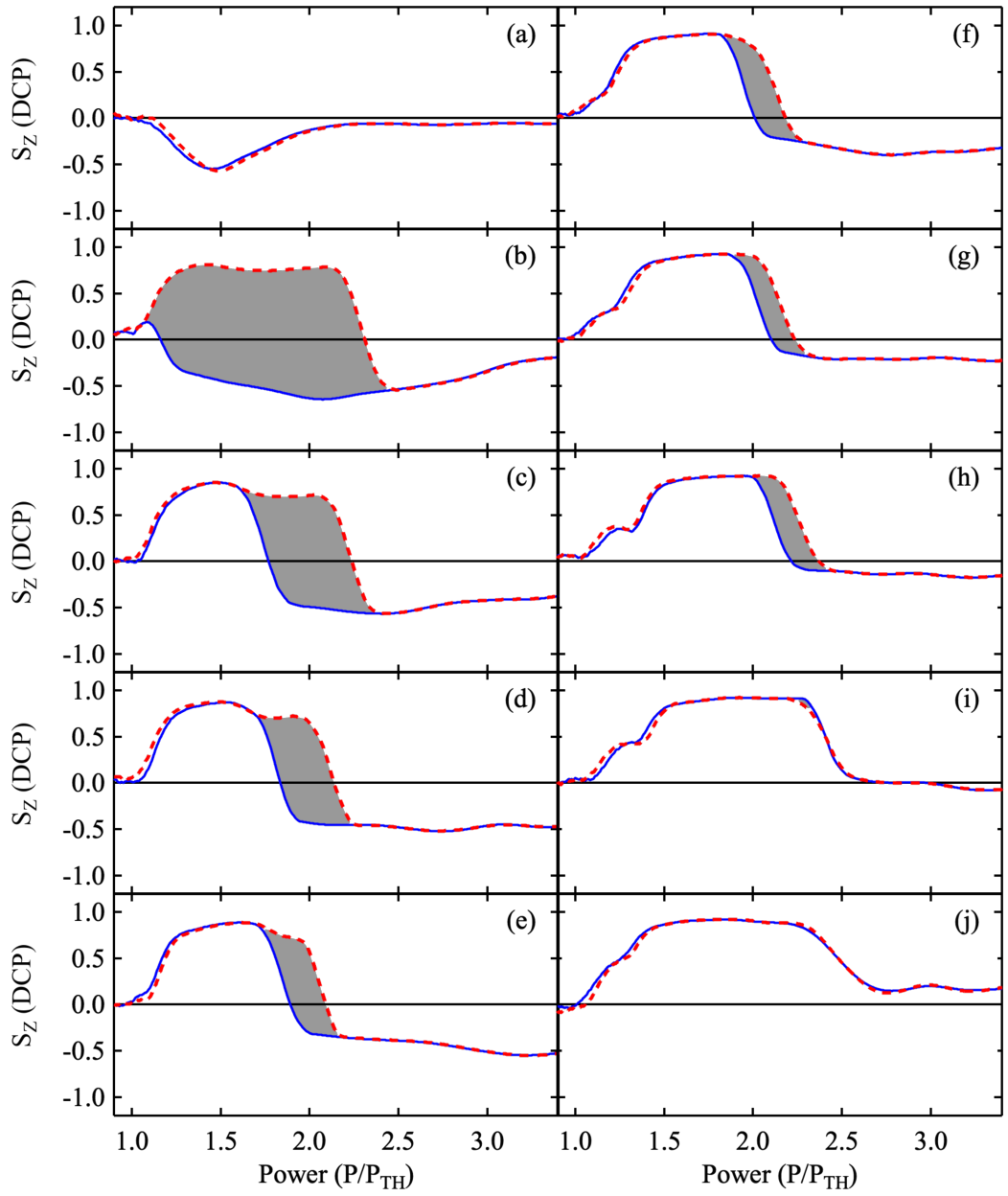

FIGURE 3.7: Measured third Stokes component, SZ, representing the degree of circular polarization (DCP) vs power demonstrating the effect of annular pump diameter (D) on the measured bistable behavior. (a) - D=20.0μm, (b) - D=17.9μm, (c) - D=16.1μm, (d) - D=15.4μm, (e) - D=14.6μm, (f) - D=14.0μm, (g) - D=13.4μm, (h) - D=13.0μm, (i) - D=12.3μm, (j) - D=11.8μm.

3.3.3 Effect of temperature

In Figure 3.8 the effect of temperature on hysteresis area is experimentally probed. The temperature range, 4 K to 40 K, was selected as the system remains in the strong coupling regime [58]. Due to temperature affecting various parameters of the system including exciton linewidth, exciton diffusion length and exciton-photon detuning, it

is not reasonable to associate the measured collapse of hystersis area onto any one parameter. Rather we can conclude that the effects combine to suppress the hystersis area.

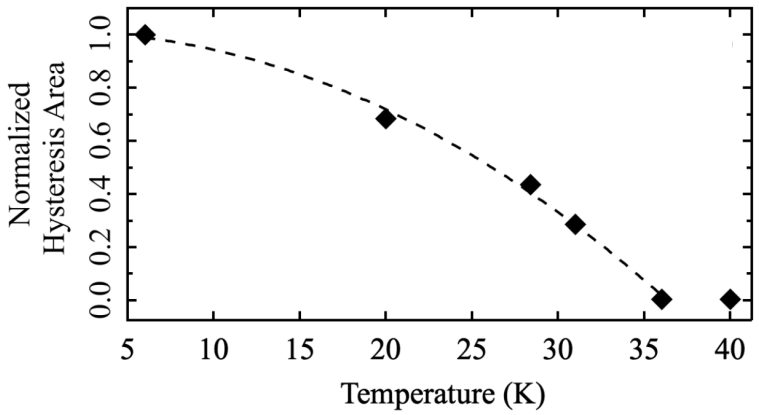

FIGURE 3.8: Temperature dependence of the hysteresis area for a $\sim 15.4\mu$m diameter annular pump with a sweep time of 1ms. Data published in [1].

3.3.4 Effect of sweep time

The suitability of the bistable spinor polariton system for potential applications in volatile memory depends on the range of times wherein the bistable behaviour is stable (non-collapsing). Hysteresis area is plotted as a function of the sweep time (T_P) in Figure 3.9, demonstrating stable (non-collapsing) bistability for sweep time spanning five orders of magnitude $T_P \in [10\mu\text{s}, 1\text{s}]$ [3].

The dependence of the hysteresis area on the sweep time exhibits a double decay behaviour indicated by the solid black and dashed red lines in Figure 3.9. A double power-law decay in hysteresis area vs sweep time has been reported to be due to quantum-fluctuations [95]. Experimentally an evolution from a double to a single power-law decay was demonstrated when increasing the average photon number and it was ascribed to a dissipative phase transition between the quantum regime and the thermodynamic limit [89]. However, the behaviour was reported to be critically dependent on the laser-cavity detuning and here spinor bistability is realised under non-resonant optical excitation. The origin of the double decay characteristic of the hystersis area vs sweep time demonstrated here is at this point an open question.

3.3.5 Effect of excitation laser

As shown in Figure 3.3 & 3.7 when the trap supports only the Gaussian-shaped ground state, when just above threshold, the system always shows a strong positive DCP. This

[3] In the experimental work carried out for Figure 3.9 the ratio of the time interval between successive sweeps (T_{sep}) and the sweep time is kept constant at $T_{sep}/T_P = 5$.

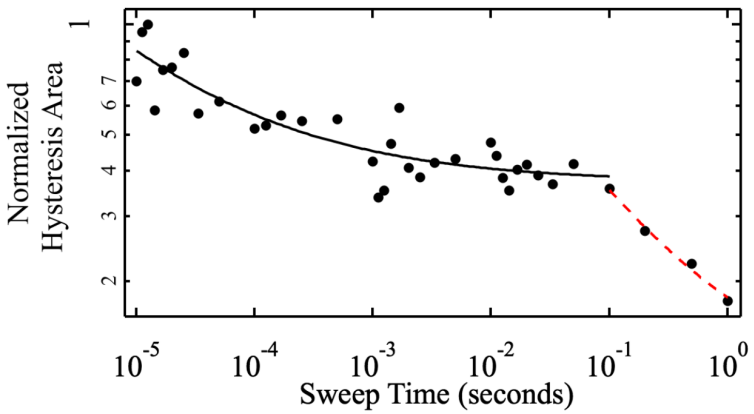

FIGURE 3.9: Hysteresis area as a function of sweep time, T_P, for $\sim 13.1\mu$m diameter annular pump recorded at $\sim$ 6K. Data published in [1].

is an effect of the angle of the linear polarisation in conjuction with the birefringence of the microcavity leading to a favourable pumping of one spin state. By placing a $\lambda/2$ waveplate after the polarising element (PBS) in the excitation path and rotating it one can switch the sign of the DCP immediately after threshold, as expected.

As a final remark it should be noted that the characterisation of the parameter space discussed above was conducted using a mono-mode CW laser, the effect disappears when switching to a multi-mode CW laser. The later introduces density fluctuations in the exciton reservoir that are mirrored in the condensate populations which collapse the hysteresis loop [96].

3.4 Concluding remarks

In this work the first experimental realisation of all-optical bistability under non-resonant excitation of a spinor polariton condensate is presented. The hysteresis loop can qualitatively be reproduced via mean-field modeling using spin-dependent Ginzburg-Landau equations with an internal Josephson coupling term between the spinor components. A mechanical analogue of the system in terms of a driven damped pendulum is provided to visualise the behaviour physically.

The detrimental nature of polariton-exciton interactions on bistable effects is probed by controlling the overlap of the trapped condensate with the pump induced exciton reservoir. By changing the excitation geometry, control over the hysteresis area is demonstrated going from a spin-discriminator (i.e. spin flip but no hysteresis) to a system with very strong bistability. We additionally obtain non-collapsing bistability hysteresis loops for a record range of sweep times in polariton systems, $[10\mu\text{s}, 1\text{s}]$, making the system promising in terms of volatile memory elements and spin switches.

3.5 Acknowledgements

The work presented in this chapter is the result of experimental work and analysis conducted by the author with numerical simulations carried out by K. Kalinin. The results are reported in the Physical Review Letters publication Ref. [1].

Chapter 4

Polariton coherence time

Due to their excitonic component, polaritons demonstrate strong interparticle interactions which are responsible for the notable blueshift in inorganic systems [53,97]. Whilst assigning a specific value to the strength of polariton-polariton interactions has previously yielded results spanning a large range of values [98–101], it is noted that the interaction strength increases with increasing exciton fraction. As such, under non-resonant excitation, the strongest interactions a condensate of polaritons will experience is with the exciton-like reservoir (denoted pol-ex interactions) which is co-localised with the non-resonant excitation beam. In the previous chapter, the deleterious effect of pol-ex interactions on the existence of bistability under non-resonant excitation was demonstrated [1]. These strong pol-ex interactions are also anticipated to be a limiting factor on the coherence properties demonstrated by polariton condensates. It is the purpose of this chapter to investigate the coherence properties of polariton condensates, specifically the effect of the reservoir present under non-resonant excitation. The work presented here is focused on the first order correlation function.

4.1 Experimental procedures

To asses the impact of the pol-ex interactions, the coherence properties of condensates spatially separated from and spatially coincident with their reservoirs are investigated. Optically trapped polariton condensates (denoted OT) serve as a platform to separate the condensate and the reservoir, they are created via annular non-resonant excitation profiles with dimensions that result in condensation in the zeroth order trapped mode. The condensates spatially coincident with the reservoir are produced by pumping with a flattened Gaussian/top hat excitation profile (denoted TH).

The work is carried out on the InGaAs QW sample [9] as described in Section 2.1. The sample is held at $\sim 6K$ using a continuous flow cold finger cryostat and is excited

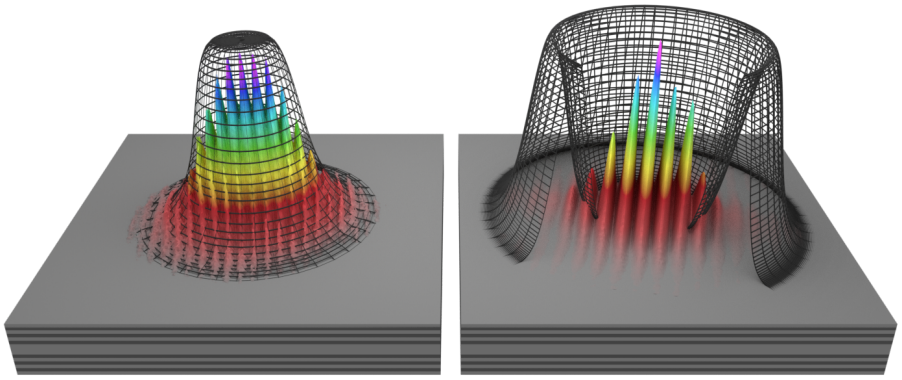

FIGURE 4.1: Schematics showing (left) the interferogram for a top hat excitation with a time delay of 57ps between the arms of the interferometer. (Right) the interferogram for an annular optical trap excitation with ground Gaussian shaped trapped state with a time delay of 840ps.

non-resonantly with a CW monomode laser, tuned to a minimum in reflectivity, energetically above the stopband at $\sim$ 800nm. Global intensity stabilisation as described in subsection 2.4.1 is implemented to minimise quasi-pulse to quasi-pulse fluctuations. The excitation beam is circularly polarised to create a maximally spin polarised condensate to minimise the additional dephasing interactions between the cross-polarised components of the spinor. The intensity of the laser is modulated in time into square pulses to prevent sample heating and it also enables single shot triggered acquisition as described in Section 2.5.4.4. As in all work in this thesis, the beam profile is shaped via imprinting a phase map on the beam with a phase-only SLM. Then when focused through a 0.4NA microscope objective lens the desired spatial profile is projected on to the samples surface.

First order coherence measurements ($g^{(1)}(\tau)$) are carried out using a Michelson interferometer in the retro-reflector - mirror configuration. The retro-reflector is mounted on a controllable delay stage capable of imposing time delays (τ), spanning 1ns, between the arms; see Section 2.5.4.1.

4.2 First order coherence

To form a baseline on which to compare the coherence properties of polariton condensates spatially separated from the exciton reservoir, the first order coherence as a function of delay time is measured for the spatially coincident condensate-reservoir regime. The points in Figure 4.2(a) correspond to the experimentally extracted visibility[1] vs delay time for TH excitation profiles of various sizes. Note the points plotted specifically correspond to the average visibility across the FWHM of the near-Gaussian intensity profile of the interferogram and the error bars are the standard deviation across the

[1]The analysis technique of visibility extraction is described in the section at the end of this chapter.

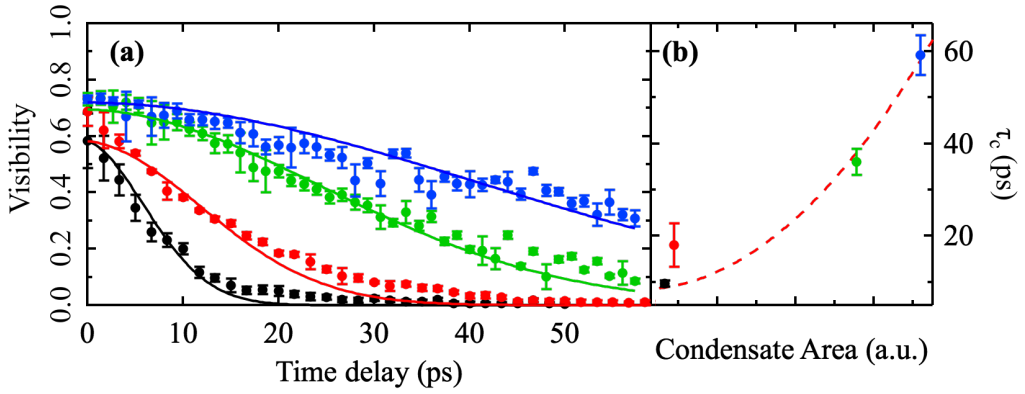

FIGURE 4.2: (a) Points - experimentally extracted visibility vs time delay (τ) where each point is the average visibility across the FWHM of the intensity profile of the interfergram (see Figure 4.3 for graphical representation), the error bars correspond to the standard deviation in visibility across the same region. Solid lines - Gaussian profiles fitted to the experimental data to extract the coherence time. The four colours correspond to different size condensates spatially coincident with the reservoir. (b) Extracted coherence time for the four condensate sizes vs the integrated area where the intensity exceeds 10% of the maximum intensity. Note the red dashed line in (b) is a quadratic function to guide the eye. Data presented in [2].

same region. The experimental points are then fitted with Gaussian functions[2] and the coherence times extracted (as described in subsubsection 2.5.4.2) and plotted in Figure 4.2(b). The marked increase in coherence time observed as the condensate size is increased, was theoretically predicted in Ref [102].

Figure 4.3(a) shows an interferogram from an optically trapped polariton condensate, the solid black line shows the intensity profile of the interferogram in the vertical direction and the two horizontal lines represent the boundaries of the corresponding FWHM. Figure 4.3(b) is a colour map of the extracted visibility for each row of the interferograms for delay times spanning the range $0 - 830$ps; note the dashed lines again represent the region that corresponds to the FWHM of the intensity profile in (a). Figure 4.3(c) shows the visibility averaged across the FWHM region for each delay time, with the standard deviation shown by the error bars. Fitting the decay with a Gaussian function centred at 0ps and with zero vertical offset (solid red line in Figure 4.3(c)) a coherence time of $\tau_{coh} = 1.54$ns is extracted; a coherence time orders of magnitude larger than the longest coherence time found under TH excitation (see Figure 4.2).

The significant enhancement of τ_{coh} exhibited by the optically trapped polariton condensate is attributed to the suppression of pol-ex interactions due to the spatial delocalisation of the condensate and the reservoir. When increasing the excitation power in the optically trapped regime, the overlap between the condensate wavefunction and the reservoir increases due to the pol-pol interactions causing the condensate to spread. This

[2]The Gaussian shape of the decay is also a feature predicted theoretically for excitation regimes around threshold [102].

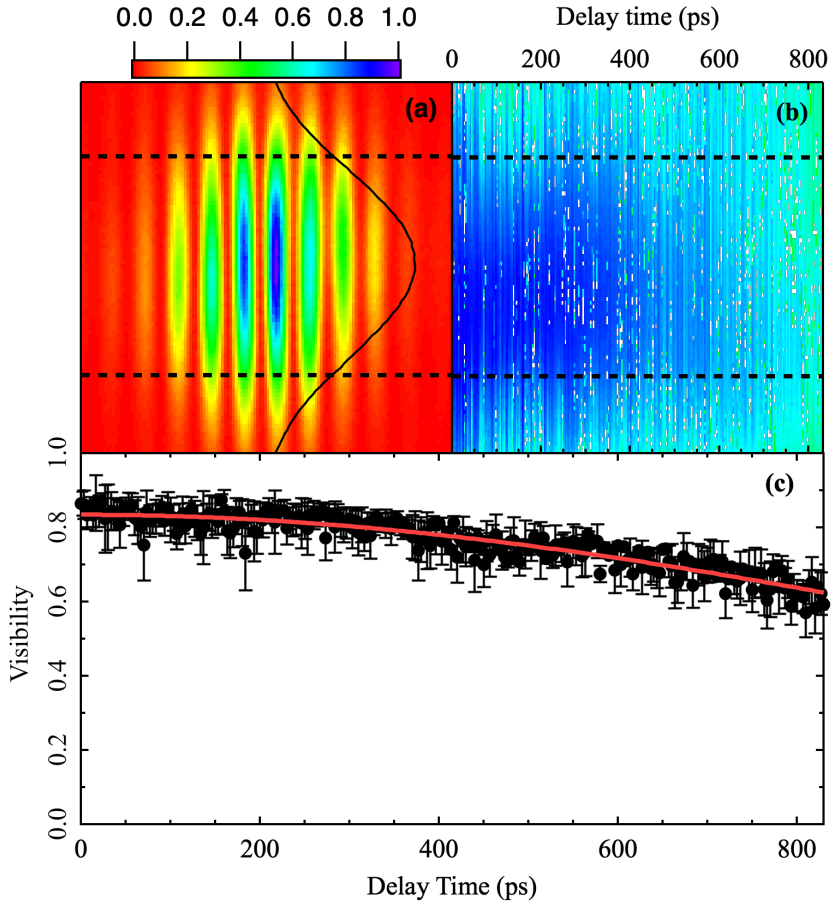

FIGURE 4.3: (a) The real space intensity distribution for the interferogram from an optically trapped polariton condensate. (b) The resultant visibility extracted for each row for delay times spanning from 0ps to 830ps. The solid black curve superimposed on (a) depicts the intensity distribution along the vertical axis and the two horizontal dashed lines in (a & b) mark the FWHM of the Gaussian intensity profile. Note the colour bar for (a & b) is shown above (a), with it representing normalised intensity for (a) and visibility for (b). (c) The visibility as a function of delay time (τ) averaged across the FWHM of the Gaussian intensity profile, error bars shown correspond to the standard deviation in visibility across this region. The solid red line in (c) shows the Gaussian fit of the visibility decay with a coherence time $\tau_c = 1.54$ns. Data presented in [2].

manifests itself in a reduction of τ_{coh} as a function of excitation density as shown in Figure 4.4. In Figure 4.4 the coherence time is plotted vs the number of counts integrated over the reference image for interferometer mirror arm at each excitation power.

4.3 Discussion

As has been demonstrated above, the first order coherence time of polariton condensates can be improved by orders of magnitude by moving from excitation regimes where the

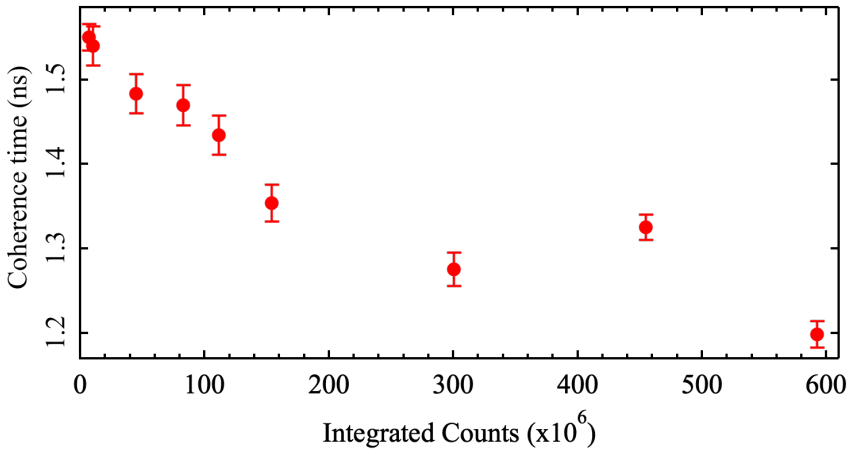

FIGURE 4.4: Coherence time vs the counts integrated in the mirror arm reference images for increasing excitation powers (left-to-right).

condensate and reservoir are spatially coincident to those where the two are separated. With the latter excitation regime, coherence times in the order of several ns are realised.

In polariton lattices even the best techniques to date allow only the tuning of nearest and perhaps next nearest neighbour interaction strengths, see chapter 5 and Ref [103]. The work here opens up the possibility to develop an external, truly arbitrary, (any-to-any) coupling platform for polariton lattices. The coherence times attainable with freely-expanding condensates are insufficient to be able to collect photoluminescence from one condensate of a lattice, arbitrarily redirect and then project back onto another condensate in the lattice, whilst maintaing coherence. However, with coherence times well within the ns scale for the OT condensates it may well be possible to achieve this.

4.4 Acknowledgments

The work presented on the first order coherence properties of polariton condensates is the result of a collaboration between the author and Alexis Askitopoulos. The work presented in this chapter is a part of [2] .

4.5 Appendix - Polariton coherence time

In this section the analytical techniques for extracting the visibility from interferograms are described.

Starting with the background corrected interferogram, the first step is to take a single pixel line profile perpendicular to the fringes, Figure 4.5. Then utilising Fourier filtering of this line profile one can determine the oscillation period of the fringe modulation

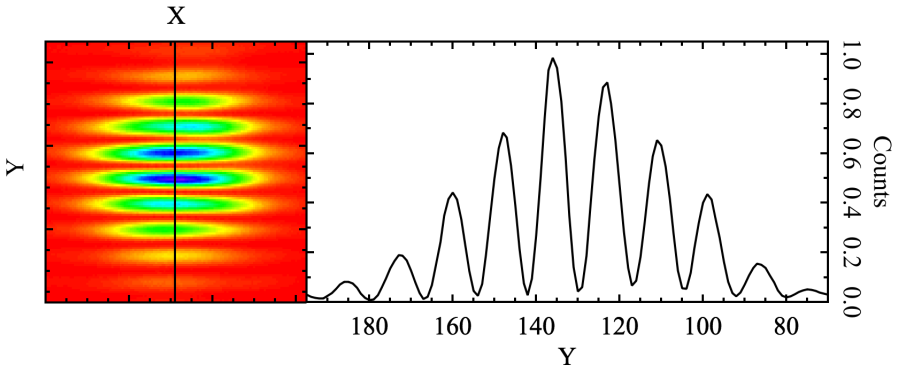

FIGURE 4.5: (a) Colourmap of a typical normalised real space interferogram of an optically trapped polariton condensate. (b) Single-line line profile along the solid vertical line in (a)

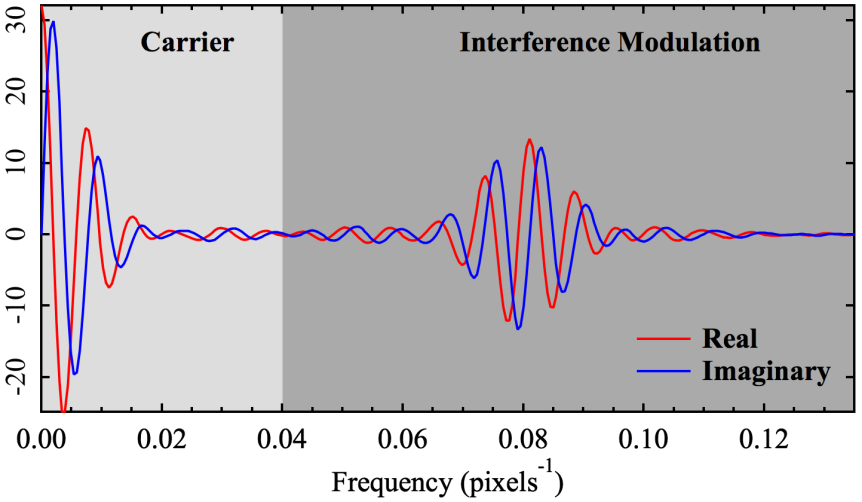

FIGURE 4.6: Region of the complex fast Fourier transform of the line profile Figure 4.5(b). The dark grey background corresponds to the regions relating to the interference fringe modulation whilst the light grey region corresponds to the carrier envelope.

due to interference and the overall intensity carrier envelope. Before computing the complex Fast Fourier Transform (FFT) it is beneficial to pad the line profile with zeros as the resolution of the FFT is proportional to the number of points in the array being transformed. Note here the line profiles are padded to 2048 points.

Broadly, the resulting FFT can be split into two regions, with the low frequency components corresponding to the carrier envelope and DC terms and the peak at higher frequencies corresponding to the interference modulation, Figure 4.6.

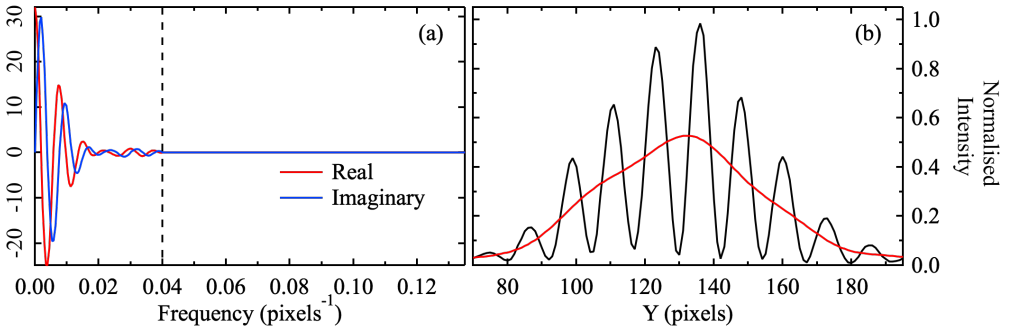

FIGURE 4.7: (a) Complex fast Fourier transform of the line profile as shown in Figure 4.6 with low pass frequency filtering (with a cutoff of 0.04 pixels^{-1}). (b) Black solid line - the line profile as shown in Figure 4.5(b), red solid line - the carrier envelope calculated by the inverse FFT of (a).

The carrier envelope (Env) can be extracted by zeroing the contribution from all frequencies above a cut-off point[3] (long-pass filtering) and computing the inverse FFT. This process is shown in Figure 4.7, with the final Env shown by the solid red line in (b). The central position of the peak, in the magnitude of the FFT, at higher frequencies corresponds to the spatial frequency of the interference fringes (ν). It is beneficial, in terms of consistently locating the correct peak, to perform short-pass filtering on the FFT of the line profile to remove the DC and carrier envelope components from the FFT.

The line profile can then be fitted with:

$$Fit(x) = Env(x)\,(1 + V cos(2\pi\nu x + \phi)) \tag{4.1}$$

using the extracted $Env(x)$ and seeding ν with the value extracted from the Fourier analysis and the visibility (V) can then be extracted. Figure 4.8 shows the line profile from Figure 4.5 as the solid black points, with the fitted Equation 4.1 shown by the red dashed curve. This technique remains robust, even for low visibilities.

Repeating this procedure for every column in Figure 4.5(a) within a region of interest (typically larger than the FWHM of the horizontal intensity profile) it is possible to construct a 1D visibility map for every interferogram. Then repeating this procedure with the interferogram for every delay time step, one creates the visiblity map as shown in Figure 4.3(b), where each column is the 1D visibility map of a singular interferogram. In the visibility vs delay time plots above, the points correspond to the average visibility over the FWHM from each 1D visiblity map and the error bars are the standard deviation.

[3]The final result of the visibility extraction process is relatively insensitive to the exact value of this cut-off frequency, but if it is set too low then the failure rate increases.

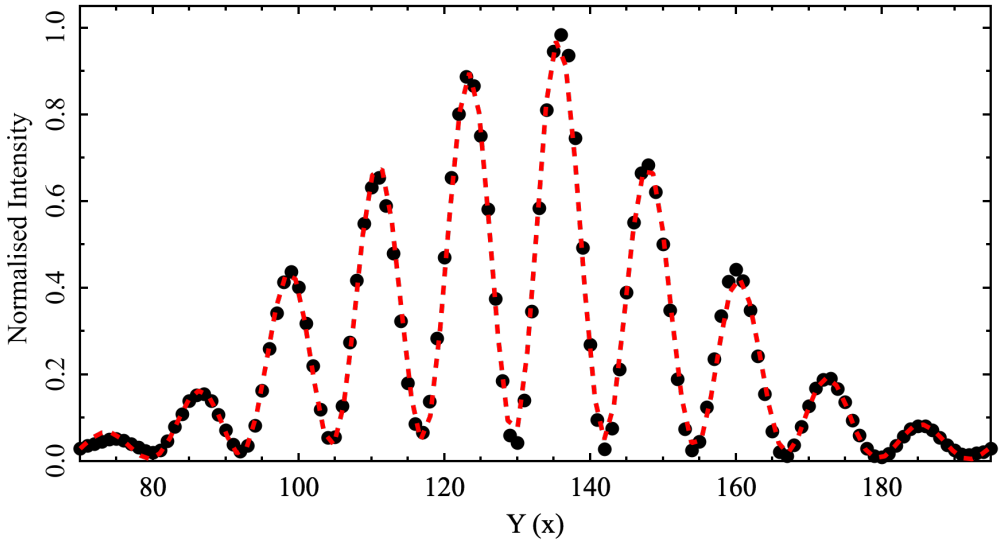

FIGURE 4.8: Black points - experimental line profile from Figure 4.5(b). Red dashed line - result of fitting Equation 4.1 to the experimental line profile, using the carrier envelope from Figure 4.7 and the interference fringe modulation frequency extracted from the FFT of the experimental line profile.

Chapter 5

Time delayed coupling of spatially separated polariton condensates

5.1 Introduction

Whilst optically trapped polariton condensates exhibit significantly enhanced first order coherence times, freely expanding polariton condensates afford an easy way to coherently couple multiple spatially separate condensates. To usefully develop extended coupled lattices of freely expanding polariton condensates, it is of utmost importance to understand the building block, namely two coupled freely expanding polariton condensates (a polariton dyad); see Figure 5.1. It transpires that the correct formalism for describing the coupling in such a system, is in terms of time delayed coupled oscillators. Where it is necessary to explicitly include the time delay within the coupling terms when the characteristic timescales (e.g. oscillator period) are shorter than the propagation time between the coupled nodes/oscillators. Time delay is common place within many fields [104–106], including biological mechanisms, perhaps most important of which are coupled neurons forming networks [107].

Previous works on coupled spatially separated polariton condensates have been based upon a phenomenological **instantaneous** coupling. Where the coupling can take the form of a conservative Josephson-like (phase) coupling [108–111], a dissipative (also referred to as radiative) coupling which corresponds to a direct particle exchange [69, 70] or a mixture of both [112, 113]. For a dyad of freely expanding polariton condensates, coupling is in the form of radiative coupling beyond the near-field and as such is conceptually different from the formalisms developed for coupled trapped condensates. Furthermore, when increasing the separation distance, the assumption of instantaneity necessarily breaks down, due to the finite speed at which polaritons propagate. As will be demonstrated here[1], it is essential that the time delay incurred from the finite polariton

[1]The work in this chapter is presented in Ref [3].

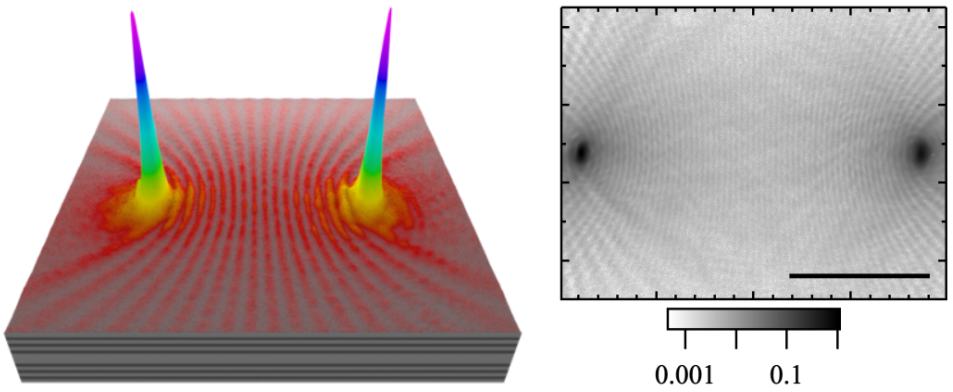

FIGURE 5.1: Left - Schematic showing two coupled spatially separated freely expanding polariton condensates with experimental interference pattern. Right - Real space photoluminescence distribution for a dyad with a separation distance exceeding 110μm, Data presented in [3]. The solid black line in the bottom right corresponds to 50μm.

propagation speed is accounted for, even for closely separated condensates. The time delayed coupling results in unique spectral phenomena and corresponding dynamics of the overall system.

In the following the experimental methodology of investigating the coupling of spatially separated, freely expanding, polariton condensates is introduced. Experimental findings are discussed in conjunction with numerical simulations via mean field theory as well as being described in terms of time delayed coupled oscillators. Finally conclusions are drawn and potential paths for future research/applications of coupled freely expanding polariton condensates are proposed.

5.2 Experimental realisation

To properly characterise the properties of a dyad of polariton condensates, a series of in depth experimental investigations are carried out. These include spatial ($\Psi(x, y)$), Fourier ($\Psi(k_x, k_y)$) and spectral dependencies on the separation distance (d) between the condensates, as well as interferometric measurements to gain ps resolution of the systems dynamics. The spatial, Fourier and spectral dependencies were taken simultaneously utilising three CCD/CMOS detectors and a high resolution 75cm spectrometer with either a 1200g/mm or 1800g/mm grating. The interferometric measurements use the Michelson interferometer in the mirror retro-reflector configuration with the retro-reflector on a 15cm double pass (total 30cm maximum) delay stage; see Section 2.5.4.

The sample used is the InGaAs QW structure described in Section 2.1, cooled to $\sim$ 6K via a cold-finger flow cryostat. A blue-detuned mono-mode CW laser at 785nm, temporally modulated at 10kHz with a duty cycle $< 5\%$ is used to excite the sample. Again the spatial profile is created via the phase-only SLM and great care is taken to

minimise intensity fluctuations, both in the relative intensities of the pump beams as well as the overall intensity of the pump profile, from one separation distance to the next.

As will be discussed in the following section, a key parameter is the relative phase of the two condensates. The relative phase can be determined via the fringe pattern created. As the dyad is a simple linear geometry, the resulting fringes are linear with the modulation parallel to the axis connecting the condensate centres. In the regime of equal pump intensities for both condensates, there are only trivial $(0, \pi)$ phase differences observed. Therefore, the relative phase can be determined by the existence of a bright fringe (intensity maxima) or dark trough (intensity minima) at $k_{||} = 0$, corresponding to the condensates being in-phase and anti-phase respectively. The relative phase can equally be described in terms of the parity of the wavefunction describing the dyad, with in-phase equating to even parity and anti-phase to odd parity.

By orientating the dyad parallel to the entrance slit of the spectrometer, the relative phase of each spectral component can independently be determined via the corresponding fringes in the momentum/in-plane wavevector axis of the energy resolved Fourier space image. These calculations are carried out in Fourier space as there is better contrast across the image due to the exponential decay of polariton population with increasing distance from the condensate centres in real space. This said, it is still possible to resolve the fringe at the centre of the dyad in real space for all but the very large values of d.

5.3 Results and discussion

5.3.1 Spectral response

The investigation into the polariton dyad was initially motivated by the observation, that under CW excitation, for most separation distances, the spectrally resolved Fourier space consists of two energies with well defined but opposite parity, see Figure 5.2(a,b and c). With only narrow regions of separation distance that result is a predominantly single energy state Figure 5.2(d,e and f). The existence of multiple energy states, for most dyad separation distances, is a feature that exists for all excitation powers including threshold.

Figure 5.3(a) shows the normalised contribution (spectral weight) of the two most dominant energy states[2] for more than 400 dyad separations in the range $5\mu\text{m} < d \leq 66\mu\text{m}$.

[2]Note that for some values of d, there are more than two energy states present. However, the spectral weight of the third energy state at threshold only contributes, at most, a few percent to the overall system and as such the discussion is focused on the two most dominant states.

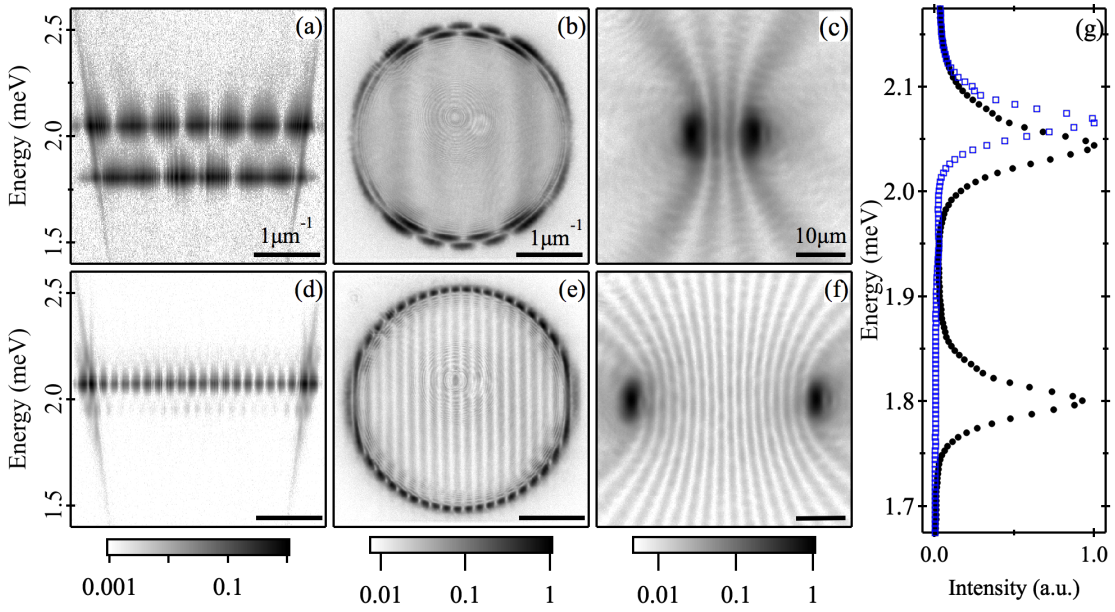

FIGURE 5.2: Experimental (a,d) energy resolved momentum space, (b,e) momentum (Fourier) space $|\Psi(k_x, k_y)|^2$ and (c,f) real space $|\Psi(x, y)|^2$ for a dyad with separation $d = 12.7\mu$m (a,b,c) and $d = 37.3\mu$m (d,e,f). The integrated and normalised spectra of (a,d) are shown in (g) with black circles and blue squares respectively. Note all images are shown in a logarithmic colour scale with the colour bars beneath the corresponding columns. Additionally the energies given are the energies above that at $k_x = 0$. Data presented in [3].

Red dots correspond to even parity states and blue squares correspond to odd parity states. There is a clear periodic, continuous transition between the system being dominated by an even-parity state and an odd-parity state, with the regions between demonstrating notable contributions from both parities. Figure 5.3(b) shows the corresponding spectral positions, demonstrating that one oscillation period in the relative spectral weight contribution of a given parity (starting from a vanishing spectral weight) corresponds to a continually red shifting branch.

Considering, for example, an odd-parity state, positions of minimal spectral weight correspond to a discontinuous jump in the energy of said state. In the direction of increasing d, this jump is from a state that is maximally red shifted from the isolated condensate (denoted by the horizontal dashed line Figure 5.3(b)) to an energy in the region of the isolated condensate energy; marking the death of one branch and the start of new one. This discontinuous jump in the odd-parity state occurs in the region of maximal contribution from the even-parity state. As d is increased further, the spectral position of the 'new' odd-parity band shows a continuously increasing redshift. A zoomed in region of separation distances from Figure 5.3 is shown in Figure 5.4 for clarity. These features (i.e. a decrease in the systems collective frequency as well as discontinuous jumps relating to phase-flip transitions) are characteristic of time-delay systems as the

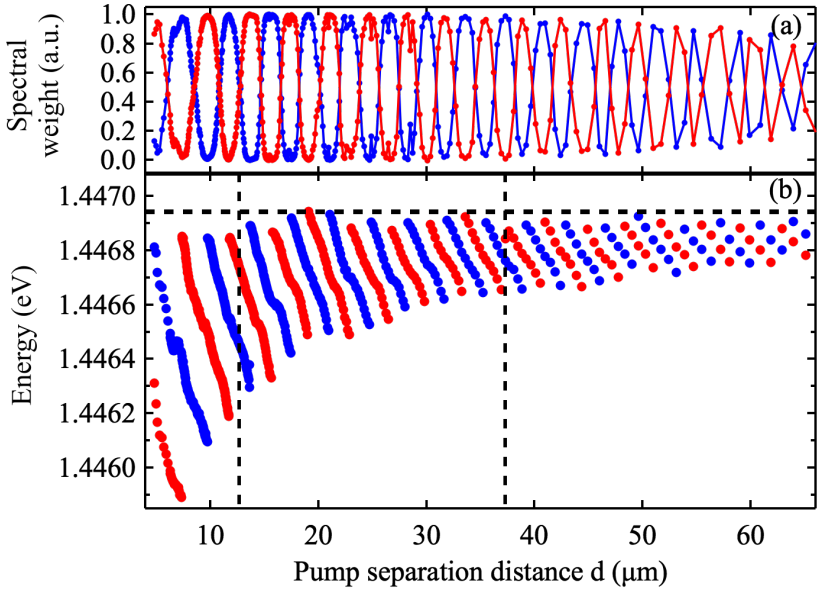

FIGURE 5.3: Experimental spectral analysis of polariton dyads as a function of separation distance. (a) Normalised spectral weight of the two most dominant energy components for each separation distance. (b) The spectral positions of the two most dominant energy components. Note red points correspond to even parity states whilst blue points correspond to odd parity states. The horizontal dashed line in (b) corresponds to the energy of a single isolated condensate in the same region of the sample with the same excitation density. The vertical dashed lines in (b) correspond to the two states shown in Figure 5.2. Data presented in [3].

time delay is increased [114]. The same characteristic behaviour is demonstrated by the even-parity states. Furthermore, the spectral width of each band (the difference between the minimally and the maximally red shifted state of a single branch), for both parities, decreases as d increases, asymptotically tending towards the unperturbed energy of isolated condensates.

5.3.2 Dynamics and coherence

In all of the distance dependence measurements, the images are taken with exposure times that far exceed the modulation period of the excitation laser. With the resultant images consequently being an average of many condensate realisations. The clarity of the features observed, as shown in Figure 5.2, demonstrates the robustness of the state the systems relaxes into. However, for the separation distances demonstrating multiple spectral components, the above techniques are insufficient to concretely determine whether the system stochastically chooses one of the spectral components observed in each realisation, or whether the components coexist in every realisation.

The use of CW excitation (albeit quasi-CW) rules out the use of Streak systems to gain sufficient time resolution to determine what, if any, the dynamics of the system

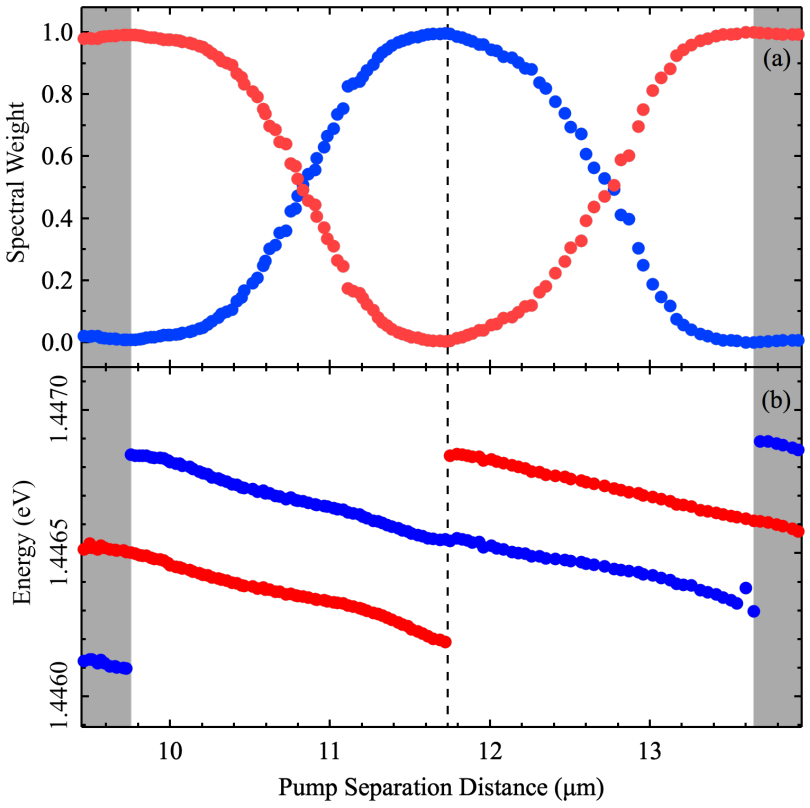

FIGURE 5.4: A zoomed in view of the data in Figure 5.3 showing just over one oscillation period of the spectral weight corresponding to the full extent of one energy branch. Data presented in [3].

are. To achieve the necessary resolution in time, auto- and cross-correlations between the condensates are recorded, utilising the Michelson inteferometer (as described in Section 2.5.4) with a controllable time delay τ between the arms. For two equally populated (with sufficiently long time averaging) condensates $\Psi_{1,2}$, each of which being formed of two coexisting and equally weighted opposite parity energy states, the complex amplitudes of the condensates can be expressed as:

$$\Psi_1(t) = \psi_0(e^{-i\omega_e t} + e^{-i(\omega_o t)}) \tag{5.1a}$$

$$\Psi_2(t) = \psi_0(e^{-i\omega_e t} - e^{-i(\omega_o t)}) \tag{5.1b}$$

where ψ_0 is a time independent real amplitude and $\omega_e = E_e/\hbar$ and $\omega_o = E_o/\hbar$ are the angular frequencies corresponding to the even and odd parity states respectively. The resulting auto-correlation, i.e. the interference of one condensate at time t with itself, delayed in time by τ, is denoted by $I_{auto}(\tau) = \langle|\Psi_1(t) + \Psi_1(t+\tau)|^2\rangle_t$. Where the angled brackets, with subscript t, corresponds to time averaging so as to be compatible

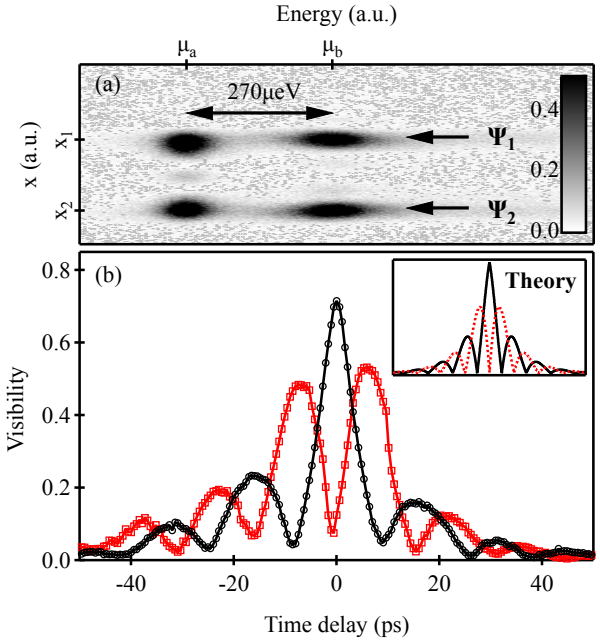

FIGURE 5.5: (a) Energy resolved real space of the PL from a dyad with $d = 10.3\mu$m pumped at 1.5 times the threshold density of a single condensate, demonstrating two opposite parity energy components of nearly equal spectral weight. (b) The auto-correlation (black) and cross-correlation (red) fringe visibility as a function of delay time τ, between the two arms of the interferometer showing clear decay and revival of fringe visibility. Data presented in [3].

with experimental observation due to the accessible exposure times. Similarly the cross-correlation, i.e. the interference of condensate 1 at time t with condensate 2, delayed in time by τ, is written $I_{cross}(\tau) = \langle|\Psi_1(t) + \Psi_2(t+\tau)|^2\rangle_t$, with the resulting functional forms:

$$I_{auto}(\tau) = 4|\psi_0|^2\left(1 + \cos\left(\frac{\Delta\tau}{2}\right)\cos\left(\tilde{\omega}\tau\right)\right) \tag{5.2a}$$

$$I_{cross}(\tau) = 4|\psi_0|^2\left(1 - \sin\left(\frac{\Delta\tau}{2}\right)\sin\left(\tilde{\omega}\tau\right)\right) \tag{5.2b}$$

where $\tilde{\omega} = (\omega_e + \omega_o)/2$ is the average (fast) frequency and $\Delta = \omega_e - \omega_o$ corresponds to the beat frequency that manifests as a modulation in intensity as a function of τ. The intensity modulation as a function of τ, due to the coexistence of two energy states, results in a periodic decay and revival of the fringe visibility (following the modulus of a sinusoidal function) in the interferograms as a function of τ. This behaviour is clearly visible in Figure 5.5 which shows the experimental fringe visibility of the auto- and cross-correlations as a function of τ for a dyad with separation $d = 10.3\mu$m, where the system exhibits two spectral components of nearly equal spectral weight. Whilst both cross- and auto-correlations show the beating behaviour, the coexistence of the odd and even

parity states leads to a π phase shift between the modulation of the two correlations; see Equation 5.2 and Figure 5.5. Experimentally, the periodic decay and revival of the fringe visibility exhibits an additional decay with τ, due to the finite coherence time of the condensates (individually and as a dyad).

From the experimentally measured energy difference between the two opposite parity states (270μeV), the predicted fringe visibility modulation period is ~ 15.3ps, in good agreement with the experimental findings. These features strongly support the assertion that the two opposite parity states coexist and the system does not stochastically chose one in every realisation. Physically this modulation in fringe visibility is the manifestation of a persistent coherent oscillation of polariton population between each of the condensate centres. The coherent particle oscillation between the condensates is a feature reproduced when numerically simulating the system, in a state with two well populated energy states, via a generalised Gross-Pitaevskii equation model[3], see Figure 5.6.

As discussed above, the dyad demonstrates regimes in which the two coexisting spectral components result in a coherent oscillation of population between the two condensate centres. There are also regimes in which this effect is suppressed due to the system populating primarily one energy state. This is confirmed experimentally in Figure 5.7 by the blue data, for $d = 20\mu$m corresponding to one dominant energy state, showing minimal fringe visibility modulation compared to the red data, for $d = 20.5\mu$m corresponding to two notably occupied energies, which shows strong decay and revival.

An additional, initially unexpected, feature is that the existence of a second coupled condensate centre significantly increases the first order coherence time of the system when compared to the isolated condensate at the same excitation density. This feature persists as the excitation density is increased, as shown in Figure 5.7(b), demonstrating an increase in coherence time exceeding 100% for all excitation densities tested.

5.3.3 Time delayed oscillators model

As mentioned in the introduction to this chapter, previous models of coupled polariton condensates use an instantaneous coupling (be it conservative, dissipative or both). However, it turns out such models are incapable of reproducing the rich phenomena observed experimentally here with freely expanding polariton condensates. Additionally it is intuitively difficult to combine the construct of instantaneous coupling with two condensate centres macroscopically separated. For the coupling of freely expanding polariton condensates, polaritons from each condensate centre must travel, inducing

[3]The GPE model used here incorporates an active and an inactive reservoir, whereby the active reservoir observes stimulated relaxation into the condensate, whilst the inactive reservoir sustains the active reservoir, but does not directly contribute to the condensate due to conservation constraints [108, 115].

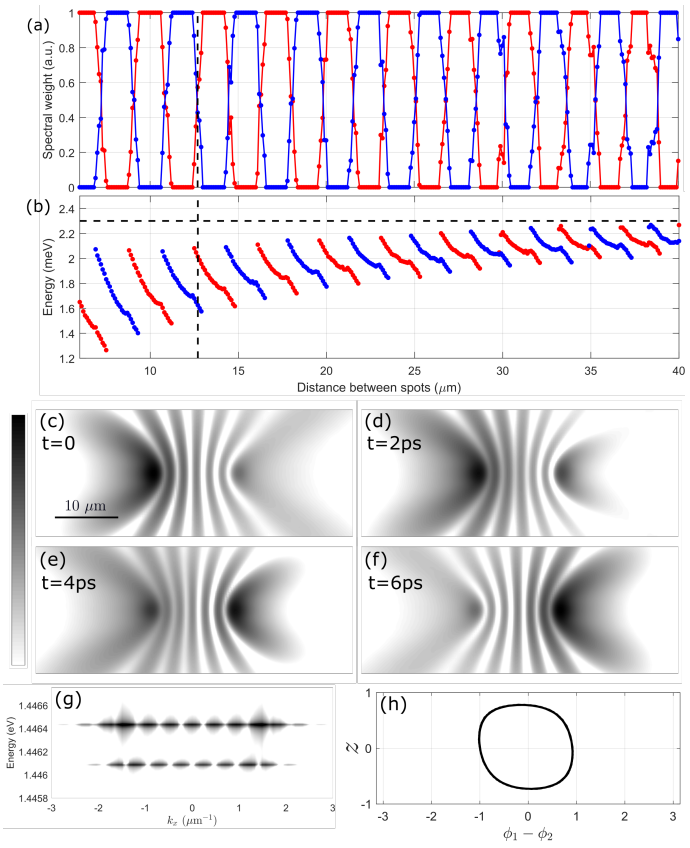

FIGURE 5.6: Results from the full 2D GPE numerical simulation of polariton dyads. (a) The spectral weight and (b) the spectral position as a function of the dyad separation distance, note the vertical dashed line corresponds to the left vertical dashed line in Figure 5.3(b) and the horizontal dashed line is the energy of an isolated condensate with the same excitation pump density. (c-f) Spatial density distributions as a function of time for a dyad operating in a two energy state, the corresponding energy resolved momentum space is shown in (g). The trajectory of the imbalance between the two condensate centres density (z) and relative phase $\phi_1 - \phi_2$ for a single oscillation period for the state corresponding to (c-g). Data presented in [3].

a phase (equally time) delay. Additionally as mentioned the observed behaviour of transitions between the two parity states (phase-flips) with discontinuous changes in frequency are universal characteristics of time-delayed coupling in non-linear systems [114, 116–119].

The problem is reduced to 1D to simplify calculations, as even in this reduced dimensionality, the key physical features are captured. Considering a system of two finite complex (the imaginary component giving the system gain) delta like potentials ($V(x)$) separated by a distance d, the time-independent non-hermitian single particle problem is formulated as:

$$E\Psi(x) = \left(-\frac{\hbar^2 \partial_x^2}{2m} + V(x) - i\frac{\hbar\gamma_c}{2} \right) \Psi(x) \tag{5.3}$$

where:

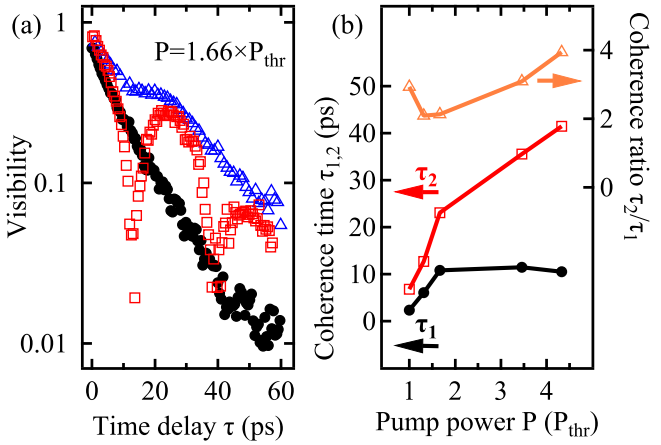

FIGURE 5.7: (a) Extracted visibility from the self interference as a function of delay time for: (black points) an isolated freely expanding polariton condensate, (blue points) a polariton dyad ($d = 20\mu$m) condensed in an approximately single energy state and (red points) a polariton dyad ($d = 20.5\mu$m) condensed in a two energy state. The overall visibility decay as a function of τ, exhibited by the isolated condensate and polariton dyad yields the corresponding coherence times (τ_1 & τ_2 respectively). These coherence times extracted and shown as a function of pump power (normalised to threshold of an isolated condensate) on the left axis of (b). The ratio of the dyad coherence time (τ_2) and the isolated condensate are shown on the right axis of (b). Data presented in [3].

$$V(x) = V_0 \left(\delta(x + d/2) + \delta(x - d/2)\right), \tag{5.4}$$

and $V_0 \in \mathbb{C}$ and m is the effective mass of the polaritons in the lower dispersion branch. Specifically V_0 is in the first quadrant of the complex plane, i.e. $\Re(V_0) \geq 0$ and $\Im(V_0) \geq 0$, denoted as $\mathbb{C}^+$. Additionally restricting solutions to waves propagating away from their corresponding condensate centre, i.e. $k \in \mathbb{C}^+$, the eigenfunctions to Equation 5.3 are:

$$\Psi(x) = \begin{cases} Ae^{-ikx}, & x \leq -d/2 \\ Be^{ikx} + Ce^{-ikx}, & |x| < d/2 \\ De^{ikx}, & x \geq d/2 \end{cases} \tag{5.5}$$

The resonance condition for a system with such a potential landscape takes the form:

$$\left[\frac{V_0}{\frac{i\hbar^2 k}{m} - V_0}\right]^2 = 1, \tag{5.6}$$

with the corresponding resonant states:

$$k_{n,\pm} = -i\tilde{V} + \frac{i}{d} W_n(\mp d\tilde{V} e^{d\tilde{V}}), \quad n \in \mathbb{Z}, \tag{5.7}$$

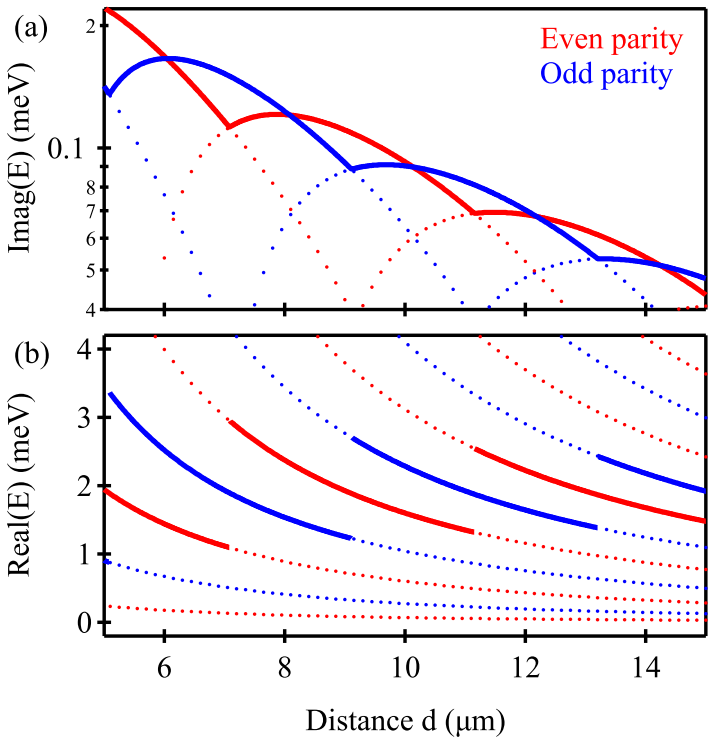

FIGURE 5.8: (a) Imaginary component of the eigenenergies from Equation 5.8 and (b) the corresponding real component. The two-delta peak potential has $\Re(V_0) = 1\text{meV}\ \mu\text{m}$ and $\Im(V_0) = 2\text{meV}\ \mu\text{m}$. The two largest positive imaginary components for every value of d are shown as solid lines whilst the rest are shown as points. Data presented in [3].

where $\tilde{V} = mV_0/\hbar^2$ and W_n are branches of the Lambert W function. Equation 5.7 describes infinitely many solutions of even (+) and odd (-) parity states with corresponding complex valued eigenvalues:

$$E_{n,\pm} = \frac{\hbar^2 k_{n,\pm}^2}{2m} - \frac{i\hbar\gamma_c}{2}. \tag{5.8}$$

Figure 5.8 shows the imaginary (a) and real (b) components of the eigenvalues for the odd (blue) and even (red) parity states; showing a qualitative agreement between the toy model energy bands and those experimentally measured (Figure 5.3). There is a periodic switching between an odd or even parity state having the largest positive imaginary component (gain), in agreement with the oscillatory (phase-flip) behaviour of the experimental spectral weights shown in Figure 5.3(a). There are regions between these, where neighbouring odd and even parity branches have equally large positive imaginary components, resulting in equal population of both states. There are also regimes in which two consecutive branches of the same parity have equal imaginary components/populations, these correlate to the discontinuous jump in frequency (death of one branch and the start of a new branch). This stepwise jump occurs at the point of maximal occupation of the opposite parity branch, as seen experimentally. Note, the

coexistence of two opposite parity energy states, for some separations, at threshold is due to similar values of gain, but above threshold even more states could reasonably have sufficient gain to additionally condense.

Whilst the time-independent 1D toy model is capable of reproducing some of the spectral phenomena experimentally observed, the results turn out to be proportional to the Lambert W function that naturally arises in time delayed differential equations [120]. This indicates the dynamics of the system are of significant interest, therefore the description is extended further, to the time-dependent regime where nonlinear interparticle interactions can additionally be accounted for. The overall system ($\Psi(x,t)$) can be written as a super position of two expanding waves ($\psi_{1,2}(x,t) = c_{1,2}(t)\phi_{1,2}(x)$) emanating from the two condensate centres, displaced from one another by a distance d:

$$\Psi(x,t) = c_1(t)\phi_1(x) + c_2(t)\phi_2(x). \tag{5.9}$$

Where the ansatz,

$$\phi_{1,2}(x) = \sqrt{\kappa}e^{ik|x\pm d/2|}, \tag{5.10}$$

is used, where $k = k_c + i\kappa$ where $k \in \mathbb{C}^+$. Restricting k to the first quadrant of the complex plane ensures that the resulting waves flow away from the condensate centres ($k_c \geq 0$) and are normalisable ($\kappa \geq 0$). Plugging Equation 5.9 into the full time-dependent version of Equation 5.3 and integrating over spatial parameters yields:

$$i\hbar\left(\dot{c}_i + \mathcal{N}_{12}\dot{c}_j\right) = F(c_i, c_j) \tag{5.11}$$

where $i = 1, 2$, $j = 3 - i$ and $\mathcal{N}_{12} = \int_{-\infty}^{\infty} \phi_2^*(x)\phi_1(x)\, dx$ is the overlap integral of the two contributing wavefunctions. Explicitly:

$$\mathcal{N}_{12} = \left(cos(k_c d) + \frac{\kappa}{k_c} sin(k_c d)\right) e^{-\kappa d} \simeq cos(k_c d)e^{-\kappa d} \tag{5.12}$$

where the simplification on the RHS can be made as $\kappa/k_c \ll 1$, due to the condensate energy ($\propto k_c$) being far greater than the linewidth ($\propto \kappa$). Additionally the term $F(c_i, c_j)$ on the RHS of Equation 5.11 has the form:

$$\begin{aligned} F(c_i, c_j) = \left(\frac{\hbar^2 k^2}{2m} - \frac{i\hbar\gamma_c}{2}\right)(c_i + \mathcal{N}_{12}c_j) + \left(\left[V_0 - \frac{i\hbar^2 k}{m}\right] c_i + V_0 e^{ikd} c_j\right)\kappa \\ + \left(\left[V_0 - \frac{i\hbar^2 k}{m}\right] c_j + V_0 e^{ikd} c_i\right)\kappa e^{-ik^* d}. \end{aligned} \tag{5.13}$$

As can be seen in Equation 5.11, the temporal dynamics of both wavefunctions are combined. To separate the temporal dependencies for each wavefunction, note that Equation 5.11 for both condensate centres can be written in vector/matrix form as:

$$i\hbar \begin{pmatrix} 1 & \mathcal{N}_{12} \\ \mathcal{N}_{12} & 1 \end{pmatrix} \begin{pmatrix} \dot{c}_1 \\ \dot{c}_1 \end{pmatrix} = \begin{pmatrix} F(c_1, c_2) \\ F(c_2, c_1) \end{pmatrix} \tag{5.14}$$

where the matrix $M = \begin{pmatrix} 1 & \mathcal{N}_{12} \\ \mathcal{N}_{12} & 1 \end{pmatrix}$ on the LHS is invertible for all conditions of relevance as $\mathcal{N}_{12} < 1$ while $d > 0$. To simplify the expansion, let us consider the case of weak coupling, which can be parameterised as the regime where the spatial overlap of the wavefunctions ($\mathcal{N}_{12}$) is small, i.e. the term $\xi = e^{-\kappa d}$ is small. In this case all terms $\mathcal{O}(\xi^2)$ and higher can be omitted. Additionally assuming that the resonance condition from the time independent toy model (Equation 5.6) is satisfied

$$i\hbar\dot{c}_i = \left[\frac{\hbar^2 k^2}{2m} - i\frac{\hbar\gamma_c}{2} + \kappa\left(V_0 - \frac{i\hbar^2 k}{m}\right)\right] c_i + V_0\kappa e^{ikd} c_j. \tag{5.15}$$

Note that when $c_i = \pm c_j$ and solving for stationary states, Equation 5.15 yields results consistent with the time independent model above (Equation 5.7). Equation 5.15 shows that interaction between the condensates is in the form of a coherent influx of particles originating from the centre of condensate j propagating onto condensate i (and vice versa), with a phase delay of $e^{ik_c d}$. When c_i and c_j are oscillating at a fixed frequency ω, the phase delay term can be recast into an effective time delay:

$$e^{ikd} c_j(t) = e^{-\kappa d} c_j(t - \tau_d), \tag{5.16}$$

where the exponential on the RHS originates from the one dimensional spatial decay of the wavefunction due to the finite lifetime of the polaritons. The time delay τ_d in the interaction originates from the finite time it takes a polariton, of given wavevector k, to propagate between the two condensate centres. Specifically it is defined as:

$$\tau_d = \frac{k_c d}{\omega}. \tag{5.17}$$

For weak coupling, in which case the change in frequency ω from that of the isolated condensate ω_0 is small, the time delay τ_d is proportional to:

$$\tau_d \approx \frac{k_{c,0} d}{\omega_0} \tag{5.18}$$

where again d denotes the separation distance between condensate centres and $k_{c,0}$ is the real component of the complex wavevector for the isolated condensate.

Expanding the system further, to include local nonlinear interactions, reservoir gain and blueshift, the full non-linear equations of motion for the coupled system of two polariton condensates becomes:

$$i\dot{c}_i = \left(\Omega + \frac{2g + iR}{2} n_{A,i} + \alpha|c_i|^2\right) c_i + Je^{i\beta} c_j(t - d/v), \tag{5.19a}$$

$$\dot{n}_{A,i} = -(\Gamma_A + R|c_i|^2) n_{A,i} + P. \tag{5.19b}$$

Where g is the polariton-reservoir interaction strength, α is the condensate polariton-polariton interaction strength, $n_{A,i}$ denotes the active reservoir of condensate i and R is the stimulated scattering rate from the active reservoir to the condensate. Γ_A is the non-stimulated decay rate of the active reservoir and P is the pump. It has been assumed that the dynamics of the inactive reservoir are slow compared to that of the condensate and active reservoir, thus the inactive reservoir is approximated as being static. The effect of the inactive reservoir is absorbed into the term $\Omega = \Omega_0 - i\Gamma$, describing the self energy of the condensate, where Γ is the effective linewidth of the propagating polaritons. The inter-condensate coupling is denoted as $Je^{i\beta} = V_0\kappa e^{-\kappa d}$. Equation 5.19 is thus a discretised Gross-Pitaevskii equation in which the inter-condensate interaction is time delayed; this markedly increases the dimensionality of the phase-space as well as the complexity of the coupled system. Furthermore, the system now shares strong similarities with the Lang-Kobayashi equation [121], where each condensate acts as an antenna radiating radially symmetric expanding waves. These sources interact, maximising gain by adjusting their shared oscillation frequency and the phase difference between the sources. The interaction is necessarily time delayed due to $k_{c,0}d \gg 1$, this is similar to coupled semiconductor laser systems that also arrive at time-delayed dynamics [122].

As the coupling is in the form of a coherent influx of particles, it's amplitude will decay spatially in the same manner as the particle density. For 2D in the linear regime, the spatial decay is well modeled by a 0-order Hankel function of the first kind ($H_0^{(1)}$) [123]. This behaviour is experimentally corroborated by looking at the spatial decay of an isolated condensate, pumped with the same excitation power as each of the condensates in the dyad and in the same region of the sample. Therefore the distance dependence of the coupling amplitude ($J(d)$) takes the form:

$$J(d) = J_0 \left| H_0^{(1)}(k_0 d) \right| \tag{5.20}$$

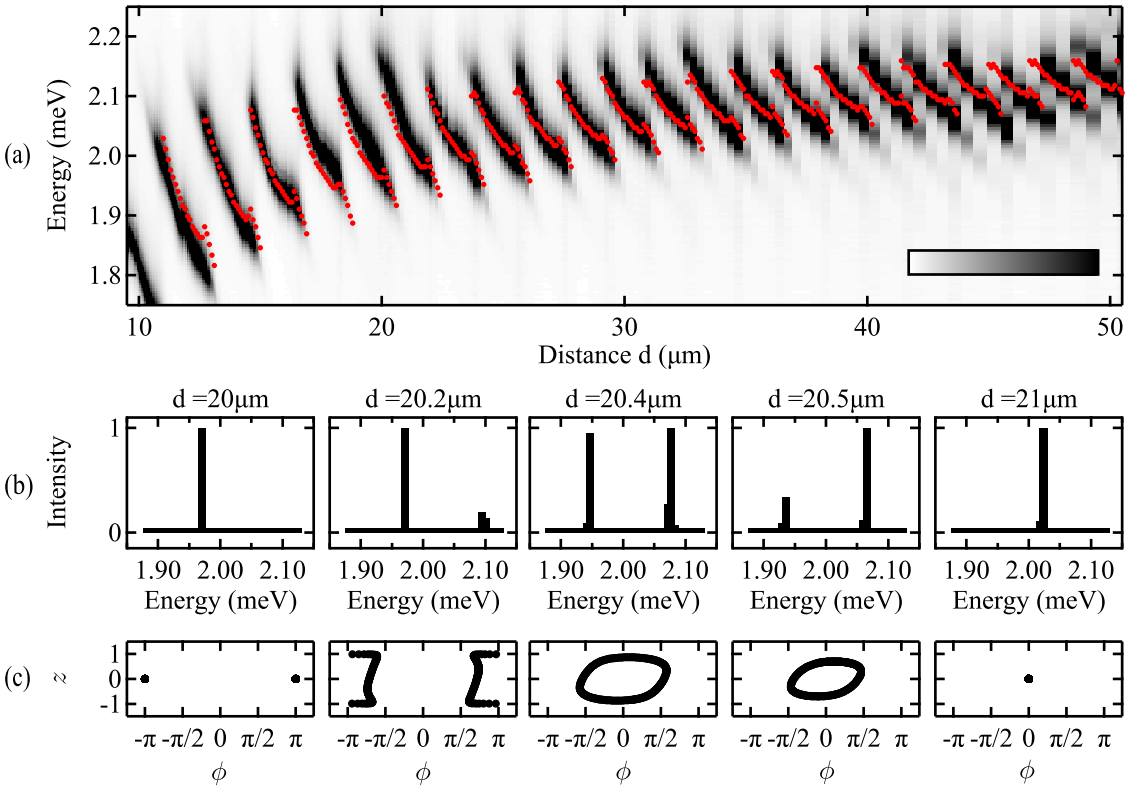

FIGURE 5.9: (a) Comparison between the experimental dyad spectra (grey-scale colourmap), in terms of blueshift from the $k_{||} = 0\mu\text{m}^{-1}$ state, with the spectral peak (or two most dominant spectral peaks when in a multimode state) resulting from numerical integration of Equation 5.19 (red points). (b) and (c) demonstrate how the spectral composition and imbalance vs phase trajectories change when going from a single mode anti-phase ($d = 20\mu$m) to a single mode in-phase ($d = 21\mu$m) state. Parameter values used: $\hbar\Omega = (1.22 - i0.5)$meV, $\hbar\alpha = 0.1\mu$eV, $\hbar R = 0.5\mu$eV, $\hbar g = 0.5\mu$eV, $v = \omega_0/k_{c,0} = 1.9\mu$m ps^{-1}, $P = 100$ps^{-1}, $\Gamma_A = 0.05$ps^{-1}, $\hbar J_0 = 1.1$meV,$k_0 = (1.7 + i0.014)\mu\text{m}^{-1}$ and $\beta = -1$. Data presented in [3].

where J_0 is, in principle, the coupling strength for vanishingly small separation distance. Numerical integration of Equation 5.19 from a initial conditions of white noise is carried out and shows excellent agreement with experimental findings; see Figure 5.9. The red dots in Figure 5.9 show the resulting spectral peak from numerical integration of Equation 5.19 when in a regime of single mode operation, or the two most dominant spectral peaks when multiple spectral components exist. They are plotted on top of a grey-scale colourmap of experimentally measured, normalised spectra of a polariton dyad vs the dyad separation distance; from which the points in Figure 5.3 are extracted. Figure 5.9(b and c) show the transition in spectral composition and phase space characteristics, when increasing d from 20μm to 21μm. The phase space diagrams show fixed points (single mode regimes) or a limit cycles (multi-mode regimes) in the phase difference $\phi = arg(c_1 * c_2)$ vs normalised population imbalance phase maps. The system starts in a fixed point, anti-phase, single mode operation state (left) then goes through a series of dynamic limit cycle solutions demonstrating multi-mode operation (middle two) and finishing in a fixed point, in-phase, single mode operation (right).

5.4 Conclusions

An in depth experimental and theoretical investigation into the polariton dyad, the building block of all coupled freely expanding polariton lattices, has been conducted. It transpires that for coupled freely expanding polariton condensates, in the coupling term it is necessary to explicitly take into account the time it takes for polaritons to propagate between the condensate centres. Through implementation of a time delayed dissipative/radiative coupling between the condensate centres (pump regions) it has been possible to semi-quantitatively reproduce spectral and dynamical features, found experimentally, via a set of dynamical equations resembling the Lang-Kobayashi equation. The necessity of time delayed coupling means the system exists in a non-bounded phase space of solutions. This complexity then favours the system for possible future applications in reservoir computing, whereby the internal dynamics of the system are used to solve problems in a manner similar to the comunication between neurons, hence the name neuromorphic computation.

Note that, numerically, the system remains well represented via the 2D Gross-Pitaevskii equation with the addition of a second, non-active, reservoir that replenishes the active reservoir.

5.5 Acknowledgements

The experimental investigations were carried out by the author and J. D. Töpfer and simulations were conducted by H. Sigurðsson and J. D. Töpfer.

Chapter 6

All optical band structure engineering

6.1 Introduction

Particles subject to potential landscapes with discrete translational symmetry exhibit bands of allowed energies in the dispersion, where the specific features correspond to the Bloch states of the potential landscape [124, 125]. Band theory is able to describe the optical properties of materials well, via consideration of the atomic arrangement within a crystal. Reverse engineering this, i.e. creating an artificial crystal by periodically patterning a material to achieve desired optical properties, is the field of band structure engineering. When producing artificial crystals it is possible to break the translational symmetry locally or introduce specific boundaries which can result in interesting phenomena, including defects and surface states which demonstrate reduced dissipation of energy into the bulk of the crystal [126].

In polariton systems, to date, band structure engineering was conducted via either patterned metallic deposition on top of the sample [127, 128] or microstructuring the samples themselves into arrays of micropillars [59,61,62,129,130] to create periodic potential landscapes in the plane of the sample. Features such as Dirac cones and flatbands have been experimentally demonstrated with polaritons utilising etched lattices in Lieb [62] and honeycomb [59, 61] geometries. In addition, theoretical proposals have been made for Bloch oscillations [131] and spontaneous formation of currents [132]. The limitation with the previous state-of-the-art is that the potential landscapes formed are permanent. Thus should one want to investigate a new geometry or lattice constant, for example, it requires an entirely new sample to be made or at least a new section to be patterned. This comes at the cost of resources and time and there is still no guarantee that the parameters of the new sample will be correct. It is thus paramount that a live tunable technique, preferably all optical, for band structure engineering is created.

This chapter introduces, and demonstrates, the ability to use non-resonantly injected polariton condensates for all-optical band structure engineering. Polaritons interact strongly with excitons and thus by shaping the spatial geometry of the exciton reservoirs, which mirrors the shape of the non-resonant excitation laser, it is possible to create arbitrary and tunable potential landscapes using the same section of planar (non-patterned) sample [1, 3, 69, 70, 133]. The geometry of the potential landscape can then be changed at the refresh rate of the LCOS SLM screen (60Hz).

6.2 Experimental techniques

This work is carried out on the planar distributed Bragg reflector (DBR) microcavity with a 2λ GaAs cavity containing eight 6nm InGaAs QWs, organised in pairs at the three anti-nodal positions of the confined field, with an additional QW at the final node either side of the cavity [9]. The sample is cooled to $\sim 6K$ using a cold finger flow cryostat and is excited with a monomode continuous wave laser, blue detuned energetically above the stopband to maximise coupling in efficiency. The laser is modulated in time into square wave packets with a frequency of 10kHz and a duty cycle $< 5\%$ to prevent sample heating. The spatial profile of the excitation beam is sculpted using a phase-only spatial light modulator to imprint a phase map so that, when the beam is focused via a 0.4 NA microscope objective lens, the desired real space is projected onto the samples surface. The same objective lens is used to collect the photoluminescence which is then directed into the detection setup. Note the relative intensity stabilisation technique, described in chapter 2 is implemented.

6.3 One-dimensional polariton artificial crystal

6.3.1 Band structure

To demonstrate the fundamental applicability of this technique for band structure engineering, the first geometry investigated is a chain of polariton condensates formed by narrow (FWHM $\sim 2\mu$m) Gaussian, non-resonant pump spots. This constitutes the simplest periodic potential possible, and even for a modest number of condensates demonstrates condensation into single particle Bloch states as the excitation density crosses condensation threshold; see Figure 6.1.

The colourmaps in Figure 6.1 show the experimental photoluminescence intensity distributions in real space (a & d) and Fourier space (b & e) along with the corresponding dispersions (c & f) for chains of eight equally separated condensates, with inter-condensate separation distances of $\sim 13\mu$m (a, b & c) and $\sim 8.6\mu$m (d, e & f) respectively. The

condensed system is characterised in real space by high intensity regions in the immediate vicinity of the pump spots, with interference fringes between them. The dispersions show energy bands with periodicity (as a function of inplane momentum) corresponding to all repetitions of the reduced Brillouin zone, of the polariton artificial crystal, that exist within the free particle dispersion. In comparison, the dispersions for a singular polariton condensate and a dyad, show energetically narrow component(s) and in the case of the dyad simple interference fringes between the condensate nodes on the free particle dispersion; see chapter 5 [3]. The occupation of energy bands for the chain indicates that polaritons created at the pump centres sense the periodicity of the potential landscape which results in the macroscopic occupation of coherent Bloch states; even for a modest number of condensates. Furthermore, comparison of the top and bottom row of Figure 6.1 clearly demonstrates that the energy band(s) in which the condensates exist is directly controllable by changing the excitation profile (specifically in Figure 6.1, the inter-condensate separation distance). The dominant occupation of a 'sub-region' of energies within the energy bands is a result of the system being in the Bose condensed regime, an effect also observed in etched polariton systems above condensation threshold [62].

In addition to the formation of energy bands, there is a Talbot interference pattern [134] in the regions either side of the chain, see Figure 6.1(a & d). Similar features have also been observed in polariton condensation using a chain of etched mesa traps [135]. Further demonstrating the ability to harness optically imprinted condensates and the concomitant potentials to achieve effects observed in etched/patterned systems with the addition of tunability.

6.3.2 Band splitting

Alternating the inter-condensate separation distances along the 1D polariton crystal ($A{-}B{-}A{-}\cdots{-}A$), as shown schematically in Fig. 6.2, causes the energy bands observed above to split. The size of the energy gap that opens is dependent on the difference between the distances A and B. Figure 6.3 shows the experimental PL dispersion (top image in each panel a-f) and the real space intensity distribution (bottom image) for chains of eight polariton condensates, where the separation distance A is held constant at $\sim 10.1\mu$m, as B is reduced from $\sim 10.1\mu$m (a) to $\sim 7.8\mu$m (j). As the difference between A and B crosses a threshold (from Figure 6.3 (c) to (d)) the energy splitting becomes larger than the respective linewidths and the energy gap becomes discernible. As the difference between A and B is increased further, the energy gap opened continues to increase (Figure 6.3(d) to (g)) and eventually the top of band N mixes with the bottom of band $N+1$ (where $N \in \mathbb{N}$) as can be seen in Figure 6.3(g) to (j).

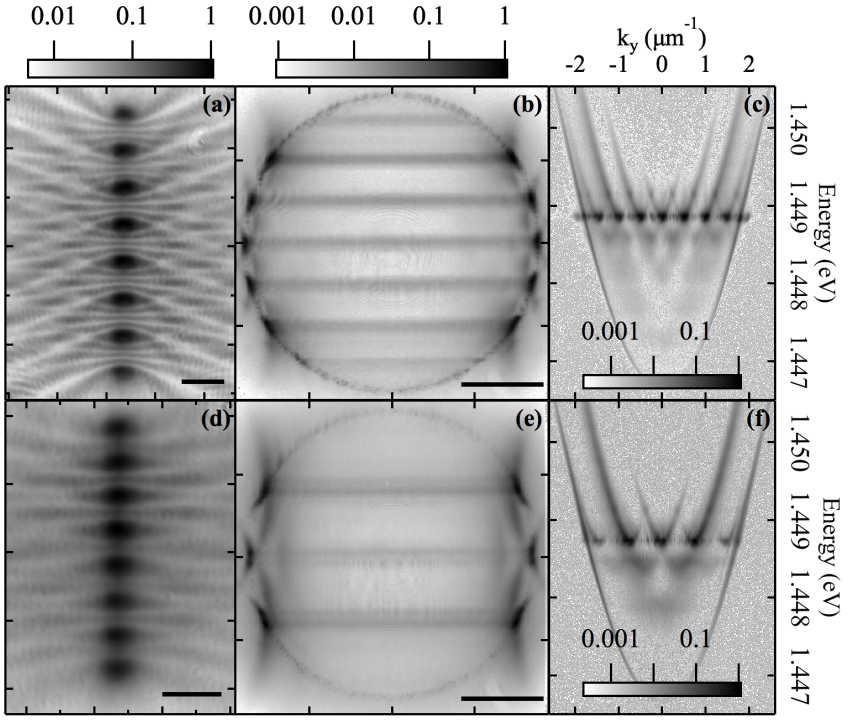

FIGURE 6.1: Photoluminescence from chains of eight equally separated polariton condensates, where the separation distance is $\sim 13\mu$m for (a,b & c) and $\sim 8.6\mu$m for (d,e & f). The left most column (a & d) shows the real space intensity distribution of the PL, the middle column (b & e) shows the Fourier space (k-space) intensity distribution and the right hand column (c & f) shows the dispersions. The corresponding colourbars for the left two columns appear above the columns and scale bars depicting 15μm (in a & d) and $1\mu\text{m}^{-1}$ (in b & e) are in the botttom right hand corner of each respective frame. Data presented in [4].

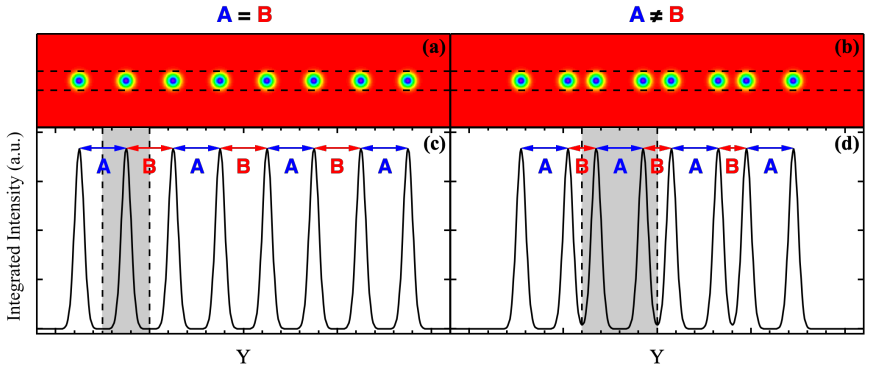

FIGURE 6.2: Schematic showing how the potential landscape is dimerised through alternating the inter-condensate separation distances in a 1D polariton crystal. (a & b) show simulated non-resonant pump laser intensity distributions for (a) a uniform chain (i.e. $A = B$) and (b) a chain with alternating inter-condensate separations (i.e. $A \neq B$). (c & d) show the horizontal line profile of the integrated intensity in (a & b) bounded by the horizontal dashed lines. As the potential landscape mirrors the excitation profile (c & d) equally represent the potential landscape in the direction along the 1D polariton crystal, where a unit cell is indicated by the grey shaded regions.

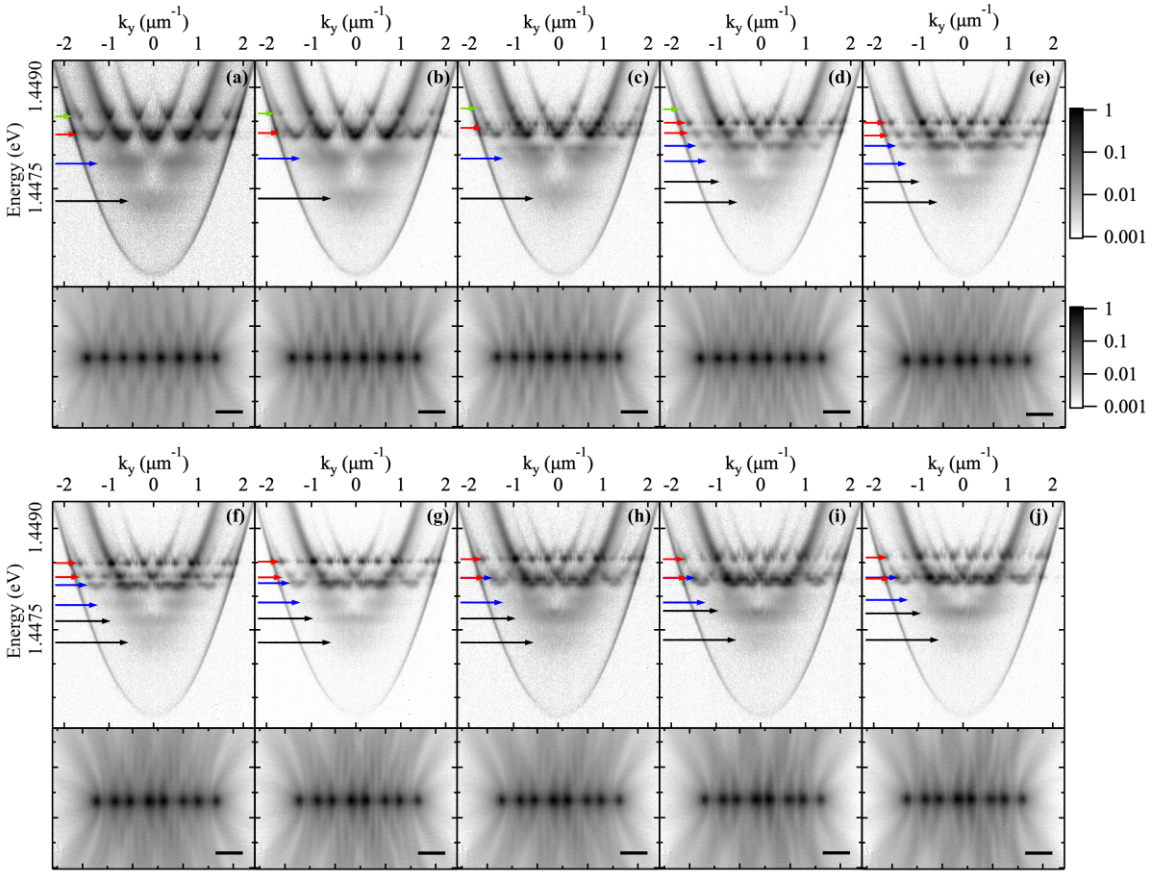

FIGURE 6.3: Each panel (a-j) shows the dispersion (top) and real space density distribution (bottom) of the PL from chains of eight polariton condensates where separation distance $A \approx 10.1\mu$m is kept fixed and $B \approx$ (a) 10.1μm, (b) 9.5μm, (c) 8.9μm, (d) 8.8μm, (e) 8.7μm, (f) 8.5μm, (g) 8.3μm, (h) 8.1μm, (i) 8.0μm and (j) 7.8μm. The coloured arrows indicate the spectral region of each energy band. Where the splitting of an energy band is visible there are two arrows of the same colour marking the upper and lower sub-band. Note that these arrows are only indicators to guide the eye. All dispersions use the same logarithmic colourscale, as do all the real space distributions with the corresponding colourbars shown to the right of (e). The solid bars in the bottom right corner of each real space distribution correspond to 15μm. Data presented in [4].

6.3.3 Broken symmetry - Defect state

Another pathway in band structure engineering is the introduction of local defects to the periodicity of the potential landscape. In the optically imprinted polariton crystal introduced here there are numerous way to imprint a defect, including changing the intensity and/or size of a given pump spot in the excitation geometry or by changing one separation distance in a 1D chain of otherwise uniform separation distances. Figure 6.4 shows the real space intensity distribution (a), dispersion (b) and an energy resolved strip of real space (c) of the PL from two chains of six polariton condensates with inter-condensate separation distance $\sim 10.2\mu$m, where the ends of the chains are separated

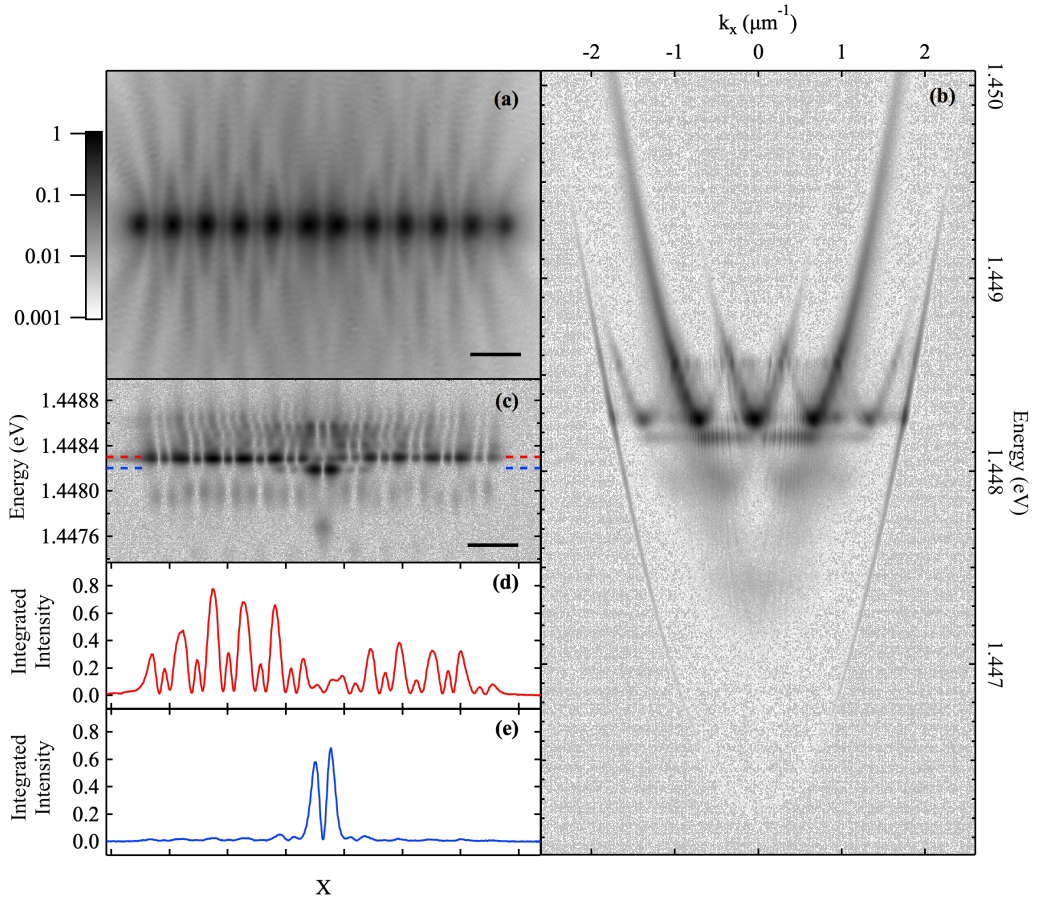

FIGURE 6.4: Photoluminescence from a chain of 12 polariton condensates, with a uniform inter-condensate separation of $\sim 10\mu$m except between the central two condensates where the gap is only $\sim 8.8\mu$m. (a) Shows the real space intensity distribution of the PL, (b) shows the corresponding dispersion with the characteristic flat band of a localised state spectrally in the gap between two spatially delocalised energy bands and (c) shows an energy resolved strip of real space going along the chain. (d) shows the line profile going across (c) centred at the spectral position of the red dashed lines corresponding to the condensed state that is delocalised across the chain. (e) is the line profile across (c) centred on the blue dashed lines in (c) corresponding to the localised defect state. The intensity colourmaps all use the same colourscale defined by the colour bar on the top left. Data presented in [4].

by $\sim 9.1\mu$m[1]. The dispersion contains the energy bands, as have been observed and discussed above, with the addition of a new flat band (spatially localised) energy state in the gap between two bands. Figure 6.4(e) shows the line profile of the energy resolved real space, centred around the energy of the flat band (highlighted by the blue dashed lines in (c)). As anticipated by the flat nature of the band in the dispersion, this state shows very strong localisation on the condensates forming the defect, with negligible occupation across the rest of the chain. Conversely the energy relating to the delocalised state shows suppression in the region surrounding the defect.

[1]i.e. It is a chain of twelve condensates with a uniform inter-condensate separation distance of $\sim 10.2\mu$m, where the central separation distance has been shortened to $\sim 9.1\mu$m to introduce a defect.

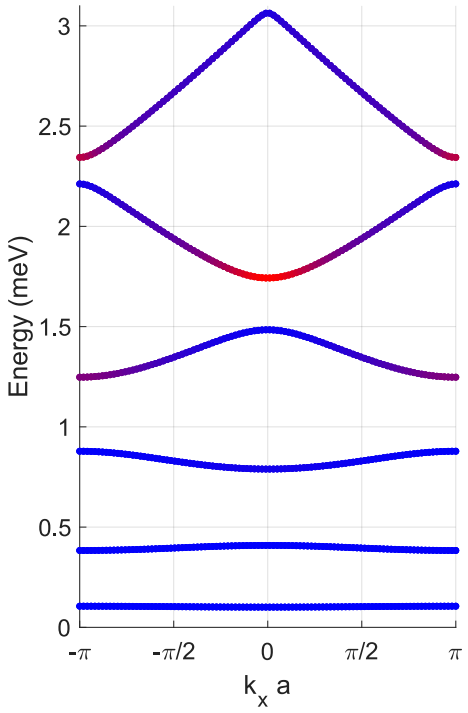

FIGURE 6.5: Energy bands calculated using Bloch's theorem for complex valued Gaussian potentials in a uniform lattice constant $\alpha = 12.4\mu$m. The colouring denotes regions of high (red) and low (blue) optical gain. Data presented in [4].

6.3.4 Simulation

From Bloch theory, solving the single particle eigenenergies in a complex potential results in the bands depicted in Figure 6.5, where colour relates to the single particle gain. The resulting bands show enhanced gain (large positive imaginary values) in the high symmetry regions that also demonstrate high occupation in the experimental dispersions (the Γ and M points of the Brillouin zone). This is a result of the group velocity becoming zero at these points, thus inhibiting dissipation of energy.

More generally the system can be simulated utilising the generalised Gross-Pitaevskii equation with both an active and an inactive reservoir, as described in section 1.3.

6.4 Conclusions and outlook

In the work presented in this chapter, an all-optical technique for band structure engineering is proposed and experimentally demonstrated. The technique harnesses the inherent potentials that exist under non-resonant optical injection of polariton condensates to create periodic potential landscapes which are probed and imaged via the condensates themselves. Furthermore, the potential landscape can be changed as desired using the same section of un-patterned sample by adjusting the geometry of the excitation laser.

The creation of allowed energy bands in the dispersions is first shown for linear chains of uniform inter-condensate separation.Where, by adjusting the separation distance, different energy bands can selectively be condensed into. Band splitting is then demonstrated via alternating the inter-condensate separation distances along the chain. It is shown that the spectral size of the gap opened can be controlled by adjusting the difference between the two separation distances within the chain. Beyond the existence of band structures and the ability to split the bands, defect state creation and lasing is demonstrated by breaking the symmetry locally. This is achieved by adjusting one of the inter-condensate separation distances in a chain of otherwise uniform separations. The resulting defect demonstrates the characteristic flat band dispersion and high degree of spatial localisation.

This work constitutes the creation of an all-optical polariton artifical crystal that demonstrates a high degree of controllability including band splitting and defect state condensation.

6.5 Acknowledgments

The work presented in this chapter is the result of experimental work by the author in conjunction with simulations carried out by H. Sigurðsson. A paper based on the work presented in this chapter with input from J. Ruostekoski and P. G. Lagoudakis is in preparation at the time of writing [4].

6.6 Appendix - Polygons

In addition to the investigation of finite linear chains, there was a line of research conducted where the chains are folded back onto themselves forming polygons. For even numbered polygons with uniform or alternating separation distances and odd polygons with uniform separation distances, there exist discrete rotational symmetries that would result in angular Bloch waves subject to periodic boundary conditions. Defects can then be introduced in several ways, including removal of a pump spot or utilising odd numbered polygons with alternating separation distances, see Figure 6.7(a).

The two-dimensional circular nature of polygon geometries, in conjunction with all-to-all coupling (as a result of the macroscopic distances over which polariton condensates can couple, see chapter 5), results in complicated Fourier space distributions (e.g. see Figure 6.6-6.8). As a result, interpretation is notably more difficult than for 1D chains or 2D lattices and so this is an area that requires further investigation before conclusions can be drawn. Nonetheless, interesting features were observed when experimentally investigating these geometries, some of which are shown below.

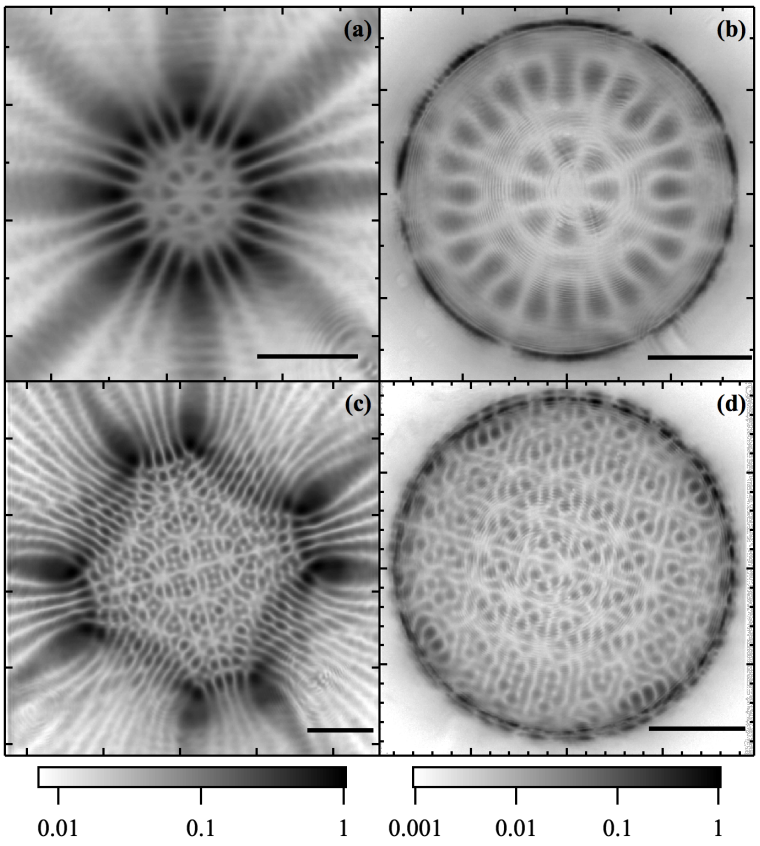

FIGURE 6.6: Photoluminescence distributions in real space (a & c) and Fourier space (b & d) for octagons of polariton condensates. The top row corresponds to an octagon with uniform inter-condensate separations of $\sim 10.4\mu$m and the bottom row to an octagon with separation distances alternating between $\sim 14.5\mu$m and $\sim 29\mu$m. The solid bars in (a & c) represent 15μm and in (b & d) $1\mu\text{m}^{-1}$. Data presented in [4].

Figure 6.6 shows the PL intensity distributions in real space (a & c) and Fourier space (b & d) for an octagon with a uniform inter-condensate separation distance of $\sim 10.4\mu$m (a & b) and an octagon with alternating distances of $A \sim 14.5\mu$m and $B \sim 29\mu$m (c & d). The Fourier space demonstrates a singular bright narrow ring for the uniform octagon, whereas, the staggered octagon demonstrates two concentric rings (distinct energy components).

Figure 6.7 shows the experimental photoluminescence distributions in real space (a), Fourier space (b) and the corresponding dispersion (c) for a nonagon with separation distances alternating between $A \sim 9.7\mu$m and $B \sim 31\mu$m. In comparison to the octagons, one clear distinction in the Fourier space distribution is that the features show significantly less contrast. This could be an indicator of states with some degree of spatial localisation due to the defect in separation distances (top of the nonagon in Figure 6.7(a)) as this reduction in contrast is not observed when there is no defect (i.e. for

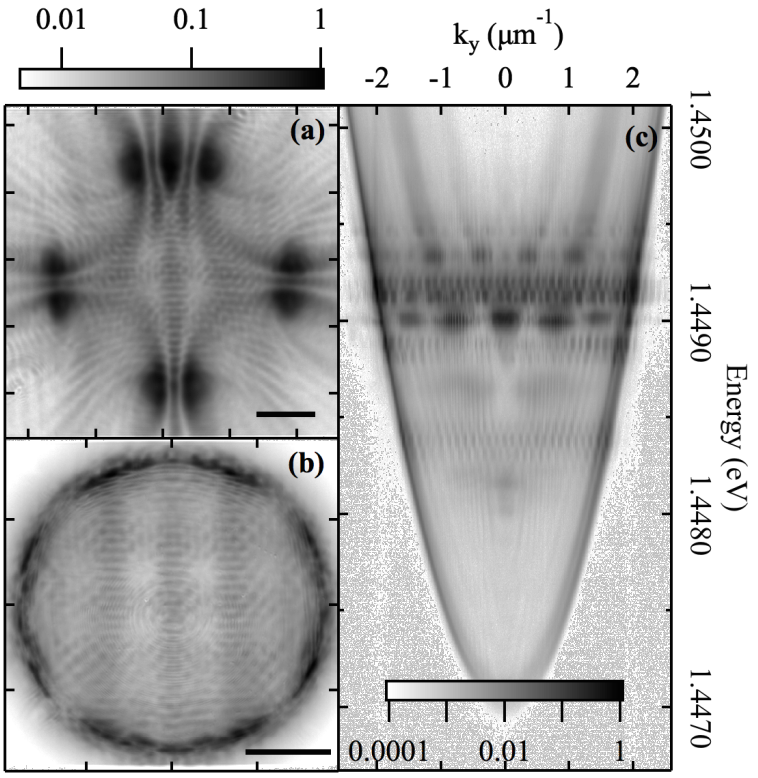

FIGURE 6.7: Photoluminescence from a nonagon with alternating with separation distances of $\sim 9.7\mu$m and $\sim 31\mu$m in (a) real space, (b) Fourier space and (c) the corresponding dispersion.

uniform nonagons) see Figure 6.8. To be able to confirm this, energy resolved tomography of the real space and Fourier space is conducted for an alternating nonagon, the results of which can be seen in Figure 6.9 and Figure 6.10.

Figure 6.9(a) shows the spectra for each condensate centre, for a nonagon with $A : B = 1 : 1.4$ (real space distribution of laser and non-energy resolved PL shown in (c & d) respectively), calculated by integrating the counts over regions surrounding each condensate centre in the tomographically reconstructed real space distribution for each energy. To quantify the level of localisation it is beneficial to consider the relative contribution of each condensate centre, for each energy, as is shown in Figure 6.9(b). The horizontal dashed line in (b) marks a value of $1/N$ where $N = 9$ - denoting the contribution value one would get when all condensate centres are equally occupied. For the spectral position corresponding to the largest occupation on the defect site (shown by the vertical dashed lines), the defect shows an enhancement of $\sim 67\%$ in occupation whilst condensate centres 1,2,5 and 6 show notable suppression. This spectral position additionally corresponds to the brightest spectral mode of the entire system.

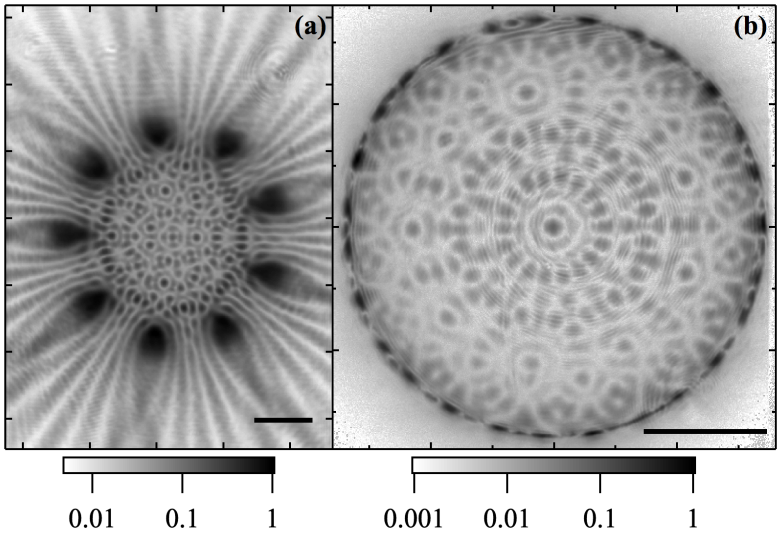

FIGURE 6.8: (a) Real space and (b) Fourier space of the photoluminescence from a nonagon with a uniform separation distance of $\sim 17.4\mu$m.

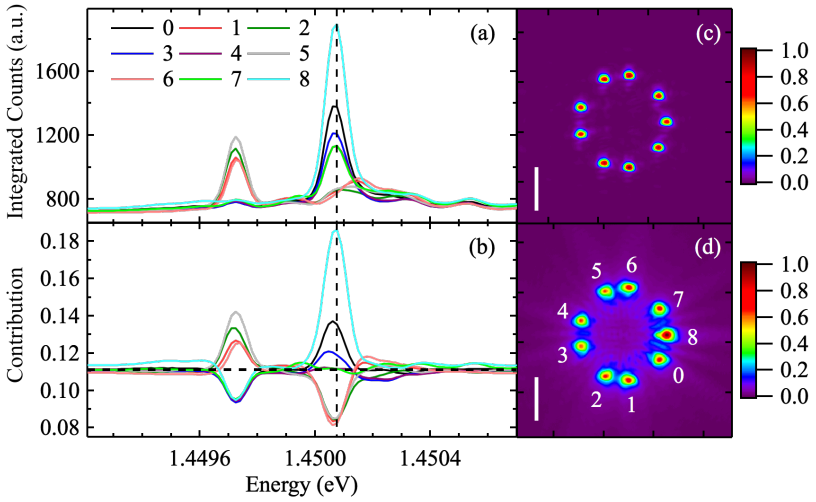

FIGURE 6.9: Alternating nonagon where the ratio of the separations A and B is 1:1.4, (a) shows the integrated counts calculated for regions around each condensate centre (numbered 0-8 corresponding to the numbers in (d)) vs energy. (b) Shows the relative contribution of each condensate centre to each energy. The horizontal dashed line corresponding to the value of 1/9, condensate contributions larger than this correspond to an enhanced occupation and contributions below this line corresponds to a suppression of occupation. (c) Real space distribution of the excitation pump laser and (d) real space distribution of the photoluminescence (not energy resolved). Note the vertical dashed lines in (a) and (b) mark the brightest overall energy, that also has the highest localisation on the defect. The reconstructed real space of the PL at this energy is shown in Figure 6.10. The solid vertical white lines in (c) and (d) correspond to 15μm. Data presented in [4].

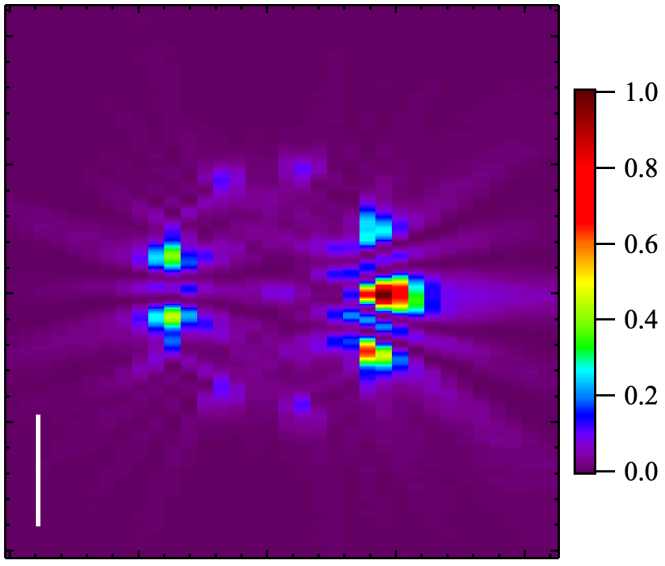

FIGURE 6.10: Tomographically reconstructed real space distribution of the alternating nonagon with a separation ratio $A : B = 1 : 1.4$ at the energy demonstrating the strongest localisation and overall intensity, corresponding to the vertical dashed line in Figure 6.9 (a & b). The solid white line represents 15μm. Data presented in [4].

Chapter 7

Conclusions, future steps and final remarks

The ease of creation, control and optical readout of polariton condensates has made the platform evermore appealing for potential use in a wide variety of applications from optical switches, transistors and lattices for possible future use in neuromorphic computation. Depending on the specifics of the sample, condensation can occur at standard cryogenic temperatures with GaAs, InGaAs & CdTe and up to room temperature with high bandgap inorganic materials such as GaN or organic active materials. Whilst the development of room temperature polariton systems has seen vast bounds in recent years [7,136], they don't yet show significant enough in-plane propagation for use in the areas investigated in this thesis. Therefore consideration is limited here to inorganic systems at standard cryogenic temperatures.

7.1 Experimental results

This thesis has specifically been concerned with the control of polariton condensates via optically imprinted potential landscapes, formed by the strong interactions between polaritons and the incoherent hot-exciton reservoir present under non-resonant excitation.

In chapter 3 the first demonstration of all-optical polariton bistability is shown in the spinor of an optically trapped polariton condensate. The strength of the bistability can be quantified in terms of the area encapsulated by the hysteresis loop. The observed suppression of this area as the overlap of the condensate with the exciton reservoir is increased, supports the determination that polariton-reservoir exciton interactions are what previously precluded the observation of all-optical bistability in non-resonantly pumped polariton condensates. This is further supported by the observation that the

hysteresis area increases as the exciton fraction (and concomitant interparticle interaction strength) is reduced.

Increasing the temperature of the sample is shown to collapse the hysteresis completely as temperatures reach $\sim 35K$. The exact origin of this collapse with temperature increase is difficult to discern as temperature affects multiple parameters, including, detuning (increasing temperature causes the detuning to become less negative) and an increased linewidth of the exciton transition (note however, strong coupling is maintained throughout the temperature range investigated). Finally it is demonstrated that the bistable behaviour persists without collapsing for excitation power sweep times spanning five orders of magnitude, from 10μs to 1s, showing future potential of the system in areas such as spin switches and volatile spin memory.

The spatial separation of the condensate from the exciton reservoir, in optically trapped polariton condensates, was additionally anticipated to greatly enhance the coherence properties of the system. In chapter 4 the coherence properties of condensates spatially separated from and spatially coincident with the exciton reservoir are investigated. The work presented specifically considers the first order coherence properties. First order coherence times, exceeding 1.5ns are demonstrated for the optically trapped polariton condensate, where spatially coincident condensates only achieve coherence times on the order of tens of ps. This opens the door to potential techniques for externally coupling any two polariton condensates in a lattice - i.e. a route towards any-to-any coupling.

When increasing the excitation power, a reduction of coherence time was observed for the optically trapped polariton condensates. However, in the range tested, the coherence time remains greater than 1ns. The reduction observed is attributed to an increased overlap of the condensed state with the exciton reservoir due to the pol-pol interactions in the condensate causing it to spread.

It was also observed that the coherence time of polariton condensates, spatially coincident with the exciton reservoir, increased as the size of the excitation pump and consequently the condensate is increased. This enhancement is due to the increased coherent polariton population, in conjunction with the reduced in-plane wavevector of the condensed state due to the flatter potential landscape. Even with this enhancement though, for the largest condensates tested, the coherence time remained sub 100ps.

Whilst optically trapped polariton condensates demonstrate first order coherence times orders of magnitude greater than the spatially coincident condensates, the spatially coincident condensates afford an easy way to couple multiple condensates across macroscopic distances. The potential landscape produced by a Gaussian excitation spot causes polaritons to ballistically propagate radially outward with a given wavevector, thus these condensates are referred to as freely expanding. In chapter 5 an in-depth experimental and theoretical investigation of the simplest basis of any freely expanding polariton condensate lattice (i.e. a dyad) is conducted.

It is observed that for most separation distances a polariton dyad exhibits two opposite parity energy states with notable occupation. As the separation distance is increased, the relative spectral weight of each parity oscillates in a near-sinusoidal manner, with a π phase difference between the oscillations for each parity. Consequently, there are small ranges of separation distance that alternatingly correspond to either the even or odd parity state having negligible occupation, and the system is effectively single mode. With increasing separation distance between two consecutive single mode operation distances, there is a reduction in the collective frequencies of the system, a phase flip of the dominant state along with a discontinuous jump in energy. This results in a series of redshifting energy branches with alternating parity as a function of separation distance. Such features are characteristic of time delayed coupled oscillators as the time delay is increased. As such, it is critically necessary when modeling, that the coupling of freely expanding condensates accounts for the finite propagation time between condensate centres. In other words the coupling is time delayed, a property that was missing in previous works where instantaneous couplings were assumed. This dramatically increases the complexity of the system, but also indicates that it could have applications in the future for neuromorphic computation.

Additionally, interferometric measurements on separation distances with multiple energy states were carried out as a function of delay time between the arms of the interferometer. The interferograms exhibit strong decay and revival of the interference visibility as a function of delay time. Thus conclusively determining that the two energy states coexist with one another, rather than the system stochastically choosing one of the two in each realisation.

Finally the experimental investigations presented are concluded in chapter 6, where an all-optical bandstructure engineering platform is introduced, harnessing the interactions between polaritons and exciton reservoirs that are present under non-resonant excitation. By spatially sculpting the non-resonant excitation laser it is possible to create an all optical polariton artificial crystal. Band structures are initially demonstrated using the simplest periodic potential, namely a 1D chain polariton condensates formed by a chain of equally sized and separated Gaussian pump spots. The band into which the system condenses is shown to be controllable via adjusting the separation distance between neighbouring pump beams. By alternating the separation distances in the chain of pump spots band splitting is clearly demonstrated. Where the size of the energy gap opened is shown to be dependent on the difference between the two separation distances used. In addition, defect state lasing is also experimentally demonstrated using a chain of condensates with uniform separation of the pump spots, except for the separation distance at the centre of the structure, which is different.

Lastly some results are shown from polygon pump geometries, where, rather than hard boundaries there is a periodic boundary; this time in the discrete rotational symmetries. By breaking these symmetries using nonagons with alternating side length, localisation

on the defect point is demonstrated via energy resolved tomography of the real space distributions.

7.2 Experimental techniques

I was fortunate when starting my PhD candidature to be presented an empty optical bench as it has allowed me to develop the skills necessary to design, build and run complex optical setups. It also afforded me the opportunity to develop techniques to improve the usability of optically imprinted polariton setups. One of which is the development of live active feedback on the kinoform calculation procedure to bring the experimentally realised excitation profile closer to the desired geometry, accounting for optical imperfections in the system.

7.3 Final remarks

I have enjoyed my PhD candidature immensely, the field of polaritonics is fast moving, exciting and holds promise for many future applications. The community of people are extraordinary and I'm very lucky to have met the people in the community I have and I look forward to meeting those (new and old) I have not met yet.

References

[1] L. Pickup, K. Kalinin, A. Askitopoulos, Z. Hatzopoulos, P. G. Savvidis, N. G. Berloff, and P. G. Lagoudakis, "Optical Bistability under Nonresonant Excitation in Spinor Polariton Condensates," *Phys. Rev. Lett.*, vol. 120, 2018.

[2] A. Askitopoulos, L. Pickup, A. Zasedatelev, S. Alyatkin, K. Lagoudakis, W. Langbein, and P. G. Lagoudakis, "Ultra long polariton condensate coherence time," *In preparation.*, 2019.

[3] J. D. Töpfer, H. Sigurdsson, L. Pickup, and P. G. Lagoudakis, "Time-delay polaritonics," *Commun Phys*, vol. 3, pp. 1–8, Jan. 2020.

[4] L. Pickup, H. Sigurðsson, J. Ruostekoski, and P. G. Lagoudakis, "Synthetic band-structure engineering in polariton crystals with non-hermitian topological phases," *In preparation*, 2019.

[5] M. H. Anderson, J. R. Ensher, M. R. Matthews, C. E. Wieman, and E. A. Cornell, "Observation of Bose-Einstein Condensation in a Dilute Atomic Vapor," *Science*, vol. 269, pp. 198–201, July 1995.

[6] K. B. Davis, M. O. Mewes, M. R. Andrews, N. J. van Druten, D. S. Durfee, D. M. Kurn, and W. Ketterle, "Bose-Einstein Condensation in a Gas of Sodium Atoms," *Phys. Rev. Lett.*, vol. 75, pp. 3969–3973, Nov. 1995.

[7] A. V. Zasedatelev, A. V. Baranikov, D. Urbonas, F. Scafirimuto, U. Scherf, T. Stferle, R. F. Mahrt, and P. G. Lagoudakis, "A room-temperature organic polariton transistor," *Nature Photonics*, p. 1, Mar. 2019.

[8] J. Kasprzak, M. Richard, S. Kundermann, A. Baas, P. Jeambrun, J. M. J. Keeling, F. M. Marchetti, M. H. Szymaska, R. Andr, J. L. Staehli, V. Savona, P. B. Littlewood, B. Deveaud, and L. S. Dang, "BoseEinstein condensation of exciton polaritons," *Nature*, vol. 443, Sept. 2006.

[9] P. Cilibrizzi, A. Askitopoulos, M. Silva, F. Bastiman, E. Clarke, J. M. Zajac, W. Langbein, and P. G. Lagoudakis, "Polariton condensation in a strain-compensated planar microcavity with InGaAs quantum wells," *Appl. Phys. Lett.*, vol. 105, Nov. 2014.

[10] A. Imamoglu, R. J. Ram, S. Pau, and Y. Yamamoto, "Nonequilibrium condensates and lasers without inversion: Exciton-polariton lasers," *Phys. Rev. A*, vol. 53, pp. 4250–4253, June 1996.

[11] S. Christopoulos, G. B. H. von Hgersthal, A. J. D. Grundy, P. G. Lagoudakis, A. V. Kavokin, J. J. Baumberg, G. Christmann, R. Butt, E. Feltin, J.-F. Carlin, and N. Grandjean, "Room-Temperature Polariton Lasing in Semiconductor Microcavities," *Phys. Rev. Lett.*, vol. 98, p. 126405, Mar. 2007.

[12] E. Wertz, L. Ferrier, D. D. Solnyshkov, P. Senellart, D. Bajoni, A. Miard, A. Lematre, G. Malpuech, and J. Bloch, "Spontaneous formation of a polariton condensate in a planar GaAs microcavity," *Appl. Phys. Lett.*, vol. 95, p. 051108, Aug. 2009.

[13] G. H. Wannier, "The Structure of Electronic Excitation Levels in Insulating Crystals," *Phys. Rev.*, vol. 52, pp. 191–197, Aug. 1937.

[14] Mott Nevill Francis, "On the absorption of light by crystals," *Proceedings of the Royal Society of London. Series A. Mathematical and Physical Sciences*, vol. 167, pp. 384–391, Sept. 1938.

[15] W. Y. Liang, "Excitons," *Phys. Educ.*, vol. 5, pp. 226–228, July 1970.

[16] M. Fox and R. Ispasoiu, *Quantum Wells, Superlattices, and Band-Gap Engineering*. Springer Handbooks, Boston, MA: Springer US, 2007.

[17] S. V. Gaponenko, *Optical Properties of Semiconductor Nanocrystals*. Cambridge, UK ; New York, NY, USA: Cambridge University Press, Jan. 1999.

[18] G. Bastard, E. E. Mendez, L. L. Chang, and L. Esaki, "Exciton binding energy in quantum wells," *Phys. Rev. B*, vol. 26, pp. 1974–1979, Aug. 1982.

[19] M. Fox and R. Ispasoiu, "Quantum Wells, Superlattices, and Band-Gap Engineering," 2017.

[20] C. F. Klingshirn, *Semiconductor Optics*. Graduate Texts in Physics, Berlin Heidelberg: Springer-Verlag, 2 ed., 2012.

[21] A. V. Kavokin, J. J. Baumberg, M. Guillaume, and F. P. Laussy, *Microcavities*. Series on semiconductor science and technology, Oxford University Press, revised ed., May 2011.

[22] J. Diouri, A. Taqi, A. E. Haddad, M. Katih, and E. Feddi, "Parametrized equations for excitons in two-dimensional semiconductor quantum wells with arbitrary potential profiles," *Semicond. Sci. Technol.*, vol. 18, pp. 377–384, Mar. 2003.

[23] S. Jorda, U. Rssler, and D. Broido, "Fine structure of excitons and polariton dispersion in quantum wells," *Phys. Rev. B*, vol. 48, pp. 1669–1677, July 1993.

[24] M. Fox and R. Ispasoiu, "Quantum Wells, Superlattices, and Band-Gap Engineering," in *Springer Handbook of Electronic and Photonic Materials* (S. Kasap and P. Capper, eds.), Springer Handbooks, pp. 1–1, Cham: Springer International Publishing, 2017.

[25] H. Tong and M. W. Wu, "Theory of excitons in cubic III-V semiconductor GaAs, InAs and GaN quantum dots: Fine structure and spin relaxation," *Phys. Rev. B*, vol. 83, p. 235323, June 2011.

[26] A. R. Hamilton, R. Danneau, O. Klochan, W. R. Clarke, A. P. Micolich, L. H. Ho, M. Y. Simmons, D. A. Ritchie, M. Pepper, K. Muraki, and Y. Hirayama, "The 0.7 anomaly in one-dimensional hole quantum wires," *J. Phys.: Condens. Matter*, vol. 20, p. 164205, Apr. 2008.

[27] S. T. Cundiff, T. Zhang, A. D. Bristow, D. Karaiskaj, and X. Dai, "Optical Two-Dimensional Fourier Transform Spectroscopy of Semiconductor Quantum Wells," *Acc. Chem. Res.*, vol. 42, pp. 1423–1432, Sept. 2009.

[28] M. Gmitra and J. Fabian, "First-principles studies of orbital and spin-orbit properties of GaAs, GaSb, InAs, and InSb zinc-blende and wurtzite semiconductors," *Physical Review B*, vol. 94, Oct. 2016.

[29] R. Winkler, *Spin-orbit Coupling Effects in Two-Dimensional Electron and Hole Systems*. Springer Tracts in Modern Physics, Berlin Heidelberg: Springer-Verlag, 2003.

[30] D. A. B. Miller, "Optical Physics of Quantum Wells," p. 28.

[31] H. W. van Kesteren, E. C. Cosman, W. A. J. A. van der Poel, and C. T. Foxon, "Fine structure of excitons in type-II GaAs/AlAs quantum wells," *Phys. Rev. B*, vol. 41, pp. 5283–5292, Mar. 1990.

[32] F. Meier and B. P. Zakharchenya, eds., *Optical Orientation - 1st Edition*. Elsevier, Nov. 1984.

[33] M. I. Dyakonov, ed., *Spin Physics in Semiconductors*. Springer Series in Solid-State Sciences, Berlin Heidelberg: Springer-Verlag, 2008.

[34] V. Savona, L. C. Andreani, P. Schwendimann, and A. Quattropani, "Quantum well excitons in semiconductor microcavities: Unified treatment of weak and strong coupling regimes," *Solid State Communications*, vol. 93, pp. 733–739, Mar. 1995.

[35] Y.-S. Huang, S.-Y. Hu, C.-C. Huang, Y.-C. Lee, J.-W. Lee, C.-C. Chang, Z.-K. Wun, and K.-K. Tiong, "Incident-angle-dependent reflectance in distributed Bragg reflectors fabricated from ZnO/MgO multilayer films," *OPT REV*, vol. 21, pp. 651–654, Sept. 2014.

[36] X. F. Li and S. F. Yu, "Modeling of Rabi splitting in quantum well microcavities using time-dependent transfer matrix method," *Opt. Express, OE*, vol. 16, pp. 19285–19290, Nov. 2008.

[37] J. R. Tischler, M. Scott Bradley, Q. Zhang, T. Atay, A. Nurmikko, and V. Bulovi, "Solid state cavity QED: Strong coupling in organic thin films," *Organic Electronics*, vol. 8, pp. 94–113, Apr. 2007.

[38] C. Weisbuch, M. Nishioka, A. Ishikawa, and Y. Arakawa, "Observation of the coupled exciton-photon mode splitting in a semiconductor quantum microcavity," *Phys. Rev. Lett.*, vol. 69, pp. 3314–3317, Dec. 1992.

[39] L. R. Brovelli and U. Keller, "Simple analytical expressions for the reflectivity and the penetration depth of a Bragg mirror between arbitrary media," *Optics Communications*, vol. 116, pp. 343–350, May 1995.

[40] H. Deng, H. Haug, and Y. Yamamoto, "Exciton-polariton Bose-Einstein condensation," *Rev. Mod. Phys.*, vol. 82, pp. 1489–1537, May 2010.

[41] S. Ben-Tabou de Leon and B. Laikhtman, "Exciton-exciton interactions in quantum wells: Optical properties and energy and spin relaxation," *Phys. Rev. B*, vol. 63, p. 125306, Mar. 2001.

[42] A. Askitopoulos, K. Kalinin, T. C. H. Liew, P. Cilibrizzi, Z. Hatzopoulos, P. G. Savvidis, N. G. Berloff, and P. G. Lagoudakis, "Nonresonant optical control of a spinor polariton condensate," *Phys. Rev. B*, vol. 93, May 2016.

[43] A. Einstein, "Quantentheorie des einatomigen idealen gases. zweite abhandlung," *Sitzungsberichte der Preussischen Akademie der Wissenschaften, Physikalisch-mathematische Klasse*, pp. 3–14, Jan. 1925.

[44] A. Einstein, "Quantentheorie des einatomigen idealen gases," *Sitzungsberichte der Preussischen Akademie der Wissenschaften, Physikalisch-mathematische Klasse*, pp. 261–267, 1924.

[45] F. London, "The λ-phenomenon of liquid helium and the bose-einstein degeneracy," *Nature*, vol. 141, pp. 643–644, Apr. 1938.

[46] P. Kapitza, "Viscosity of liquid helium below the λ-point," *Nature*, vol. 141, p. 74, Jan. 1938.

[47] Y. Yamamoto, "Qis385 "Bose-Einstein condensation and matter-wave lasers" lecture series."

[48] M. Fox, *Quantum Optics An Introduction*. Oxford ; New York: Oxford University Press, USA, June 2006.

[49] C. J. Pethick and H. Smith, *Bose-Einstein Condensation in Dilute Gases*. Sept. 2008.

[50] O. Penrose and L. Onsager, "Bose-Einstein Condensation and Liquid Helium," *Phys. Rev.*, vol. 104, pp. 576–584, Nov. 1956.

[51] E. A. Cerda-Mndez, D. N. Krizhanovskii, M. Wouters, R. Bradley, K. Biermann, K. Guda, R. Hey, P. V. Santos, D. Sarkar, and M. S. Skolnick, "Polariton Condensation in Dynamic Acoustic Lattices," *Phys. Rev. Lett.*, vol. 105, p. 116402, Sept. 2010.

[52] Y. Sun, P. Wen, Y. Yoon, G. Liu, M. Steger, L. N. Pfeiffer, K. West, D. W. Snoke, and K. A. Nelson, "Bose-Einstein Condensation of Long-Lifetime Polaritons in Thermal Equilibrium," *Phys. Rev. Lett.*, vol. 118, p. 016602, Jan. 2017.

[53] T. Byrnes, N. Y. Kim, and Y. Yamamoto, "Exciton-polariton condensates," *Nature Physics*, vol. 10, pp. 803–813, Nov. 2014.

[54] N. B. Kopnin, "Introduction to Ginzburg-Landau and Gross-Pitaevskii Theories for Superconductors and Superfluids," *Journal of Low Temperature Physics*, vol. 129, pp. 219–262, Dec. 2002.

[55] T. Winiecki, "Numerical Studies of Superfluids and Superconductors."

[56] M. Wouters and I. Carusotto, "Excitations in a Nonequilibrium Bose-Einstein Condensate of Exciton Polaritons," *Phys. Rev. Lett.*, vol. 99, p. 140402, Oct. 2007.

[57] R. Houdr, J. L. Gibernon, P. Pellandini, R. P. Stanley, U. Oesterle, C. Weisbuch, J. OGorman, B. Roycroft, and M. Ilegems, "Saturation of the strong-coupling regime in a semiconductor microcavity: Free-carrier bleaching of cavity polaritons," *Phys. Rev. B*, vol. 52, Sept. 1995.

[58] P. Tsotsis, P. S. Eldridge, T. Gao, S. I. Tsintzos, Z. Hatzopoulos, and P. G. Savvidis, "Lasing threshold doubling at the crossover from strong to weak coupling regime in GaAs microcavity," *New J. Phys.*, vol. 14, 2012.

[59] T. Jacqmin, I. Carusotto, I. Sagnes, M. Abbarchi, D. Solnyshkov, G. Malpuech, E. Galopin, A. Lematre, J. Bloch, and A. Amo, "Direct Observation of Dirac Cones and a Flatband in a Honeycomb Lattice for Polaritons," *Phys. Rev. Lett.*, vol. 112, Mar. 2014.

[60] M. Galbiati, L. Ferrier, D. D. Solnyshkov, D. Tanese, E. Wertz, A. Amo, M. Abbarchi, P. Senellart, I. Sagnes, A. Lematre, E. Galopin, G. Malpuech, and J. Bloch, "Polariton Condensation in Photonic Molecules," *Phys. Rev. Lett.*, vol. 108, Mar. 2012.

[61] S. Klembt, T. H. Harder, O. A. Egorov, K. Winkler, R. Ge, M. A. Bandres, M. Emmerling, L. Worschech, T. C. H. Liew, M. Segev, C. Schneider, and S. Hfling, "Exciton-polariton topological insulator," *Nature*, vol. 562, p. 552, Oct. 2018.

[62] C. Whittaker, E. Cancellieri, P. Walker, D. Gulevich, H. Schomerus, D. Vaitiekus, B. Royall, D. Whittaker, E. Clarke, I. Iorsh, I. Shelykh, M. Skolnick, and D. Krizhanovskii, "Exciton Polaritons in a Two-Dimensional Lieb Lattice with Spin-Orbit Coupling," *Phys. Rev. Lett.*, vol. 120, p. 097401, Mar. 2018.

[63] A. Askitopoulos, H. Ohadi, A. V. Kavokin, Z. Hatzopoulos, P. G. Savvidis, and P. G. Lagoudakis, "Polariton condensation in an optically induced two-dimensional potential," *Phys. Rev. B*, vol. 88, July 2013.

[64] A. Askitopoulos, T. C. H. Liew, H. Ohadi, Z. Hatzopoulos, P. G. Savvidis, and P. G. Lagoudakis, "Robust platform for engineering pure-quantum-state transitions in polariton condensates," *Phys. Rev. B*, vol. 92, July 2015.

[65] A. Askitopoulos, A. V. Nalitov, E. S. Sedov, L. Pickup, E. D. Cherotchenko, Z. Hatzopoulos, P. G. Savvidis, A. V. Kavokin, and P. G. Lagoudakis, "All-optical quantum fluid spin beam splitter," *Phys. Rev. B*, vol. 97, June 2018.

[66] A. Dreismann, P. Cristofolini, R. Balili, G. Christmann, F. Pinsker, N. G. Berloff, Z. Hatzopoulos, P. G. Savvidis, and J. J. Baumberg, "Coupled counterrotating polariton condensates in optically defined annular potentials," *PNAS*, vol. 111, June 2014.

[67] D. N. Krizhanovskii, K. G. Lagoudakis, M. Wouters, B. Pietka, R. A. Bradley, K. Guda, D. M. Whittaker, M. S. Skolnick, B. Deveaud-Pldran, M. Richard, R. Andr, and L. S. Dang, "Coexisting nonequilibrium condensates with long-range spatial coherence in semiconductor microcavities," *Phys. Rev. B*, vol. 80, July 2009.

[68] A. Kavokin, P. G. Lagoudakis, G. Malpuech, and J. J. Baumberg, "Polarization rotation in parametric scattering of polaritons in semiconductor microcavities," *Phys. Rev. B*, vol. 67, May 2003.

[69] N. G. Berloff, M. Silva, K. Kalinin, A. Askitopoulos, J. D. Tpfer, P. Cilibrizzi, W. Langbein, and P. G. Lagoudakis, "Realizing the classical XY Hamiltonian in polaritonsimulators," *Nature Materials*, vol. 16, Sept. 2017.

[70] H. Ohadi, R. L. Gregory, T. Freegarde, Y. G. Rubo, A. V. Kavokin, N. G. Berloff, and P. G. Lagoudakis, "Nontrivial Phase Coupling in Polariton Multiplets," *Phys. Rev. X*, vol. 6, Aug 2016.

[71] D.-K. Yang and S.-T. Wu, *Fundamentals of Liquid Crystal Devices.* John Wiley & Sons Ltd, 2006.

[72] P. Cristofolini, *Optical control of polariton condensation and dipolaritons in coupled quantum wells*. PhD thesis, University of Cambridge, Feb. 2015.

[73] M. Pasienski and B. DeMarco, "A high-accuracy algorithm for designing arbitrary holographic atom traps," *Opt. Express, OE*, vol. 16, Feb. 2008.

[74] R. W. Gerchberg and W. O. Saxton, "A practical algorithm for the determination of phase from image and diffraction plane pictures.," *Optik*, vol. 35, 1972.

[75] M. U. Wehner, M. H. Ulm, and M. Wegener, "Scanning interferometer stabilized by use of Pancharatnam's phase," *Opt. Lett., OL*, vol. 22, pp. 1455–1457, Oct. 1997.

[76] K. Lagoudakis, *On the Physics of Exciton-Polariton Condensates*. PhD thesis, EPFL, Nov. 2010.

[77] E. Abraham and S. D. Smith, "Optical bistability and related devices," *Reports on Progress in Physics*, vol. 45, 1982.

[78] H. Gibbs, *Optical Bistability: Controlling Light With Light*. Elsevier, Dec. 2012.

[79] A. Joshi, A. Brown, H. Wang, and M. Xiao, "Controlling optical bistability in a three-level atomic system," *Physical Review A*, vol. 67, 2003.

[80] P. Jung, G. Gray, R. Roy, and P. Mandel, "Scaling law for dynamical hysteresis," *Physical Review Letters*, vol. 65, 1990.

[81] F. Forsmann, D. Jger, and W. Niessen, "Nonresonant optical bistability in InP:Fe seed devices," *Optics Communications*, vol. 62, 1987.

[82] H. Gibbs, S. McCall, and T. Venkatesan, "Differential gain and bistability using a sodium-filled fabry-perot interferometer," *Physical Review Letters*, vol. 36, 1976.

[83] P. Smith and E. Turner, "A bistable fabry-perot resonator," *Applied Physics Letters*, vol. 30, 1977.

[84] A. Baas, J. P. Karr, H. Eleuch, and E. Giacobino, "Optical bistability in semiconductor microcavities," *Physical Review A*, vol. 69, 2004.

[85] A. Baas, J.-P. Karr, M. Romanelli, A. Bramati, and E. Giacobino, "Optical bistability in semiconductor microcavities in the nondegenerate parametric oscillation regime: Analogy with the optical parametric oscillator," *Physical Review B*, vol. 70, 2004.

[86] T. K. Paraso, M. Wouters, Y. Lger, F. Morier-Genoud, and B. Deveaud-Pldran, "Multistability of a coherent spin ensemble in a semiconductor microcavity," *Nature Materials*, vol. 9, 2010.

[87] R. Cerna, Y. Lger, T. K. Paraso, M. Wouters, F. Morier-Genoud, M. T. Portella-Oberli, and B. Deveaud, "Ultrafast tristable spin memory of a coherent polariton gas.," *Nature Communications*, vol. 4, 2013.

[88] C. Ouellet-Plamondon, G. Sallen, F. Morier-Genoud, D. Y. Oberli, M. T. Portella-Oberli, and B. Deveaud, "Reservoir-induced decoherence of resonantly excited confined polaritons.," *Physical Review B*, vol. 95, 2017.

[89] S. R. K. Rodriguez, W. Casteels, F. Storme, N. Carlon Zambon, I. Sagnes, L. Le Gratiet, E. Galopin, A. Lemaître, A. Amo, C. Ciuti, and J. Bloch, "Probing a dissipative phase transition via dynamical optical hysteresis," *Physical Review Letters*, vol. 118, 2017.

[90] A. Dreismann, H. Ohadi, Y. del Valle-Inclan Redondo, R. Balili, Y. G. Rubo, S. I. Tsintzos, G. Deligeorgis, Z. Hatzopoulos, P. G. Savvidis, and J. J. Baumberg, "A sub-femtojoule electrical spin-switch based on optically trapped polariton condensates," *Nature Materials*, vol. 15, 2016.

[91] D. Bajoni, E. Semenova, A. Lemaître, S. Bouchoule, E. Wertz, P. Senellart, S. Barbay, R. Kuszelewicz, and J. Bloch, "Optical bistability in a gaas-based polariton diode.," *American Physical Society*, vol. 101, 2008.

[92] M. Amthor, T. C. H. Liew, C. Metzger, S. Brodbeck, L. Worschech, M. Kamp, I. A. Shelykh, A. V. Kavokin, C. Schneider, and S. Hfling, "Optical bistability in electrically driven polariton condensates.," *Physical Review B*, vol. 91, 2015.

[93] O. Kyriienko, E. A. Ostrovskaya, O. A. Egorov, I. A. Shelykh, and T. C. H. Liew, "Bistability in microcavities with incoherent optical or electrical excitation," *Physical Review B*, vol. 90, 2014.

[94] S. H. Strogatz, *Nonlinear Dynamics and Chaos: With Applications to Physics, Biology, Chemistry and Engineering.* Perseus Books, 2000.

[95] W. Casteels, F. Storme, A. Le Boité, and C. Ciuti, "Power laws in the dynamic hysteresis of quantum nonlinear photonic resonators," *Physical Review A*, vol. 93, 2016.

[96] H. Abbaspour, G. Sallen, S. Trebaol, F. Morier-Genoud, M. T. Portella-Oberli, and B. Deveaud, "Effect of a noisy driving field on a bistable polariton system," *Physical Review B*, vol. 92, 2015.

[97] C. Ciuti, V. Savona, C. Piermarocchi, A. Quattropani, and P. Schwendimann, "Role of the exchange of carriers in elastic exciton-exciton scattering in quantum wells," *Phys. Rev. B*, vol. 58, pp. 7926–7933, Sept. 1998.

[98] E. Estrecho, T. Gao, N. Bobrovska, D. Comber-Todd, M. D. Fraser, M. Steger, K. West, L. N. Pfeiffer, J. Levinsen, M. M. Parish, T. C. H. Liew, M. Matuszewski,

D. W. Snoke, A. G. Truscott, and E. A. Ostrovskaya, "Direct measurement of polariton-polariton interaction strength in the Thomas-Fermi regime of exciton-polariton condensation," *Phys. Rev. B*, vol. 100, p. 035306, July 2019.

[99] S. R. K. Rodriguez, A. Amo, I. Sagnes, L. Le Gratiet, E. Galopin, A. Lematre, and J. Bloch, "Interaction-induced hopping phase in driven-dissipative coupled photonic microcavities," *Nature Communications*, vol. 7, p. 11887, June 2016.

[100] Y. Sun, Y. Yoon, M. Steger, G. Liu, L. N. Pfeiffer, K. West, D. W. Snoke, and K. A. Nelson, "Direct measurement of polaritonpolariton interaction strength," *Nature Physics*, vol. 13, pp. 870–875, Sept. 2017.

[101] A. Delteil, T. Fink, A. Schade, S. Hfling, C. Schneider, and A. mamolu, "Towards polariton blockade of confined excitonpolaritons," *Nature Materials*, vol. 18, p. 219, Mar. 2019.

[102] D. M. Whittaker and P. R. Eastham, "Coherence properties of the microcavity polariton condensate," *EPL*, vol. 87, p. 27002, July 2009.

[103] S. Alyatkin, J. D. Töpfer, A. Askitopoulos, H. Sigurdsson, and P. G. Lagoudakis, "Optical control of synchronous phases in a programmable polariton cell," *arXiv:1907.08580 [cond-mat]*, July 2019. arXiv: 1907.08580.

[104] T. Heil, I. Fischer, W. Elssser, J. Mulet, and C. R. Mirasso, "Chaos Synchronization and Spontaneous Symmetry-Breaking in Symmetrically Delay-Coupled Semiconductor Lasers," *Phys. Rev. Lett.*, vol. 86, pp. 795–798, Jan. 2001.

[105] L. Bauer, J. Bassett, P. Hvel, Y. N. Kyrychko, and K. B. Blyuss, "Chimera states in multi-strain epidemic models with temporary immunity," *Chaos*, vol. 27, p. 114317, Oct. 2017.

[106] K. Manoj, S. A. Pawar, and R. I. Sujith, "Experimental Evidence of Amplitude Death and Phase-Flip Bifurcation between In-Phase and Anti-Phase Synchronization," *Scientific Reports*, vol. 8, p. 11626, Aug. 2018.

[107] A. Barardi, B. Sancristbal, and J. Garcia-Ojalvo, "Phase-Coherence Transitions and Communication in the Gamma Range between Delay-Coupled Neuronal Populations," *PLOS Computational Biology*, vol. 10, p. e1003723, July 2014.

[108] K. G. Lagoudakis, B. Pietka, M. Wouters, R. Andr, and B. Deveaud-Pldran, "Coherent Oscillations in an Exciton-Polariton Josephson Junction," *Phys. Rev. Lett.*, vol. 105, p. 120403, Sept. 2010.

[109] M. Abbarchi, A. Amo, V. G. Sala, D. D. Solnyshkov, H. Flayac, L. Ferrier, I. Sagnes, E. Galopin, A. Lematre, G. Malpuech, and J. Bloch, "Macroscopic quantum self-trapping and Josephson oscillations of exciton polaritons," *Nature Physics*, vol. 9, pp. 275–279, May 2013.

[110] H. Ohadi, A. Ramsay, H. Sigurdsson, Y. del Valle-Inclan Redondo, S. Tsintzos, Z. Hatzopoulos, T. Liew, I. Shelykh, Y. Rubo, P. Savvidis, and J. Baumberg, "Spin Order and Phase Transitions in Chains of Polariton Condensates," *Phys. Rev. Lett.*, vol. 119, p. 067401, Aug. 2017.

[111] G. Christmann, G. Tosi, N. G. Berloff, P. Tsotsis, P. S. Eldridge, Z. Hatzopoulos, P. G. Savvidis, and J. J. Baumberg, "Oscillatory solitons and time-resolved phase locking of two polariton condensates," *New J. Phys.*, vol. 16, p. 103039, Oct. 2014.

[112] I. L. Aleiner, B. L. Altshuler, and Y. G. Rubo, "Radiative coupling and weak lasing of exciton-polariton condensates," *Phys. Rev. B*, vol. 85, p. 121301, Mar. 2012.

[113] K. P. Kalinin and N. G. Berloff, "Polaritonic network as a paradigm for dynamics of coupled oscillators," *arXiv:1902.09142 [cond-mat, physics:nlin, physics:physics]*, Feb. 2019. arXiv: 1902.09142.

[114] E. Niebur, H. G. Schuster, and D. M. Kammen, "Collective frequencies and metastability in networks of limit-cycle oscillators with time delay," *Phys. Rev. Lett.*, vol. 67, pp. 2753–2756, Nov. 1991.

[115] K. G. Lagoudakis, F. Manni, B. Pietka, M. Wouters, T. C. H. Liew, V. Savona, A. V. Kavokin, R. Andr, and B. Deveaud-Pldran, "Probing the Dynamics of Spontaneous Quantum Vortices in Polariton Superfluids," *Phys. Rev. Lett.*, vol. 106, p. 115301, Mar. 2011.

[116] H. G. Schuster and P. Wagner, "Mutual Entrainment of Two Limit Cycle Oscillators with Time Delayed Coupling," *Prog Theor Phys*, vol. 81, pp. 939–945, May 1989.

[117] S. Yanchuk and P. Perlikowski, "Delay and periodicity," *Phys. Rev. E*, vol. 79, p. 046221, Apr. 2009.

[118] A. Prasad, J. Kurths, S. K. Dana, and R. Ramaswamy, "Phase-flip bifurcation induced by time delay," *Phys. Rev. E*, vol. 74, p. 035204, Sept. 2006.

[119] A. Prasad, S. K. Dana, R. Karnatak, J. Kurths, B. Blasius, and R. Ramaswamy, "Universal occurrence of the phase-flip bifurcation in time-delay coupled systems," *Chaos*, vol. 18, p. 023111, May 2008.

[120] R. M. Corless, G. H. Gonnet, D. E. G. Hare, D. J. Jeffrey, and D. E. Knuth, "On the Lambert W function," *Adv Comput Math*, vol. 5, pp. 329–359, Dec. 1996.

[121] R. Lang and K. Kobayashi, "External optical feedback effects on semiconductor injection laser properties," *IEEE Journal of Quantum Electronics*, vol. 16, pp. 347–355, Mar. 1980.

[122] M. C. Soriano, J. Garca-Ojalvo, C. R. Mirasso, and I. Fischer, "Complex photonics: Dynamics and applications of delay-coupled semiconductors lasers," *Rev. Mod. Phys.*, vol. 85, pp. 421–470, Mar. 2013.

[123] M. Wouters, I. Carusotto, and C. Ciuti, "Spatial and spectral shape of inhomogeneous nonequilibrium exciton-polariton condensates," *Phys. Rev. B*, vol. 77, p. 115340, Mar. 2008.

[124] N. Ashcroft and N. Mermin, *Solid State Physics*. New York: Brooks Cole, new edition edition ed., Jan. 1976.

[125] Kronig R. De L., Penney William George, and Fowler Ralph Howard, "Quantum mechanics of electrons in crystal lattices," *Proceedings of the Royal Society of London. Series A, Containing Papers of a Mathematical and Physical Character*, vol. 130, pp. 499–513, Feb. 1931.

[126] H. Nmec, P. Kuel, L. Duvillaret, A. Pashkin, M. Dressel, and M. T. Sebastian, "Highly tunable photonic crystal filter for the terahertz range," *Opt. Lett., OL*, vol. 30, Mar. 2005.

[127] N. Y. Kim, K. Kusudo, C. Wu, N. Masumoto, A. Lffler, S. Höfling, N. Kumada, L. Worschech, A. Forchel, and Y. Yamamoto, "Dynamical d-wave condensation of excitonpolaritons in a two-dimensional square-lattice potential," *Nature Physics*, vol. 7, p. 681, Sept. 2011.

[128] C. W. Lai, N. Y. Kim, S. Utsunomiya, G. Roumpos, H. Deng, M. D. Fraser, T. Byrnes, P. Recher, N. Kumada, T. Fujisawa, and Y. Yamamoto, "Coherent zero-state and π-state in an excitonpolariton condensate array," *Nature*, vol. 450, p. 529, Nov. 2007.

[129] P. St-Jean, V. Goblot, E. Galopin, A. Lematre, T. Ozawa, L. L. Gratiet, I. Sagnes, J. Bloch, and A. Amo, "Lasing in topological edge states of a one-dimensional lattice," *Nature Photonics*, vol. 11, p. 651, Oct. 2017.

[130] M. Milievi, T. Ozawa, G. Montambaux, I. Carusotto, E. Galopin, A. Lematre, L. Le Gratiet, I. Sagnes, J. Bloch, and A. Amo, "Orbital Edge States in a Photonic Honeycomb Lattice," *Phys. Rev. Lett.*, vol. 118, p. 107403, Mar. 2017.

[131] H. Flayac, D. D. Solnyshkov, and G. Malpuech, "Bloch oscillations of an exciton-polariton Bose-Einstein condensate," *Phys. Rev. B*, vol. 83, p. 045412, Jan. 2011.

[132] A. Nalitov, T. Liew, A. Kavokin, B. Altshuler, and Y. Rubo, "Spontaneous Polariton Currents in Periodic Lateral Chains," *Phys. Rev. Lett.*, vol. 119, p. 067406, Aug. 2017.

[133] G. Tosi, G. Christmann, N. G. Berloff, P. Tsotsis, T. Gao, Z. Hatzopoulos, P. G. Savvidis, and J. J. Baumberg, "Sculpting oscillators with light within a nonlinear quantum fluid," *Nature Physics*, vol. 8, p. 190, Mar. 2012.

[134] H. F. T. E. F.R.S, "LXXVI. Facts relating to optical science. No. IV," *The London, Edinburgh, and Dublin Philosophical Magazine and Journal of Science*, vol. 9, pp. 401–407, Dec. 1836.

[135] T. Gao, E. Estrecho, G. Li, O. Egorov, X. Ma, K. Winkler, M. Kamp, C. Schneider, S. Hfling, A. Truscott, and E. Ostrovskaya, "Talbot Effect for Exciton Polaritons," *Phys. Rev. Lett.*, vol. 117, p. 097403, Aug. 2016.

[136] T. Cookson, K. Georgiou, A. Zasedatelev, R. T. Grant, T. Virgili, M. Cavazzini, F. Galeotti, C. Clark, N. G. Berloff, D. G. Lidzey, and P. G. Lagoudakis, "A Yellow Polariton Condensate in a Dye Filled Microcavity," *Advanced Optical Materials*, vol. 5, no. 18, p. 1700203, 2017.